QUANTUM WALKS OF A RUBIDIUM BOSE-EINSTEIN CONDENSATE AND THEIR APPLICATIONS

By

JERRY H. CLARK

Bachelor of Science in Physics, Chemistry, and Mathematics
Arkansas State University
Jonesboro, Arkansas
2012

Submitted to the Faculty of the
Graduate College of the
Oklahoma State University
in partial fulfillment of
the requirements for
the Degree of
DOCTOR OF PHILOSOPHY
December, 2022

QUANTUM WALKS OF A RUBIDIUM
BOSE-EINSTEIN CONDENSATE
AND THEIR APPLICATIONS

Dissertation Approved:

Dr. Yingmei Liu

Dissertation Advisor

Dr. Albert Rosenberger

Dr. Derek Meyers

Dr. Birne Binegar

ACKNOWLEDGMENTS

I would first like to thank my advisor Dr. Yingmei Liu for her guidance and help throughout the last few years in dealing with the experiment, data analysis, and general professionalism in working in physics. She inspires me to work my best and to push myself to be better and I will undoubtedly continue to be inspired by her in the years to come. I also want to thank Dr. Gil Summy and the previous students in the Rubidium lab including Siamak Dadras, Jiating Ni, Wa Kun Lam, and Amruthaa for their help in getting me acquainted with the lab and the BEC system so that I could complete my research and even helping remotely if possible when I ran into issues. Jared and Zach for their help in the lab when I needed extra equipment and for their help with the computational analysis of data. Cosmo, who joined the lab much later but still provided helpful insights and has also become a good friend. I would also like to thank my committee members and the rest of the faculty and office staff of the physics department at OSU. You all work hard to provide an excellent learning environment and also make physics fun. I want to thank Larry and Wes in the machine shop for building numerous high-quality parts to be used in the lab when it was necessary.

I would like to thank my parents for their encouragement during my Ph.D. work. You were both here with me in spirit even if you weren't able to visit often. Last and certainly not least I would like to thank my wonderful wife Dulanjani for her patience, understanding, and endless encouragement throughout these years. She kept me going in those times when I was most discouraged.

"True education is a kind of never ending story — a matter of continual beginnings, of

Acknowledgments reflect the views of the author and are not endorsed by committee members or Oklahoma State University.

habitual fresh starts, of persistent newness." -J.R.R. Tolkien

Acknowledgments reflect the views of the author and are not endorsed by committee members or Oklahoma State University.

Name: JERRY H. CLARK

Date of Degree: DECEMBER, 2022

Title of Study: QUANTUM WALKS OF A RUBIDIUM BOSE-EINSTEIN CONDENSATE AND THEIR APPLICATIONS

Major Field: PHYSICS

Abstract:

A quantum walk in momentum space with a rubidium spinor Bose-Einstein condensate was recently realized in our research group by applying a periodic kicking potential as a walk operator and a resonant microwave pulse as a coin toss operator. The generated quantum walks appear to be stable for up to ten steps and then quickly transit to classical walks due to spontaneous emissions induced by laser beams of the walk operator. The quantum to classical walk transitions were investigated by introducing well-controlled spontaneous emissions with an external light source during quantum walks. Our findings demonstrate a scheme to control the robustness of the quantum walks and can also be applied to other cold atom experiments involving spontaneous emissions. Our QW possessed behaviors that generally agreed with theoretical predictions; however, it also showed momentum distributions that were not adequately explained by the theory. A theoretical model is presented in which the coherent dynamics of the spinor condensate is sufficient to explain the experimental data without invoking the presence of a thermal cloud of atoms as in the original theory. These numerical findings are supported by an analytical prediction for the momentum distributions in the limit of zero-temperature condensates. This current model provides more complete explanations to the momentum-space QWs that can be applied to study quantum search algorithms and topological phases in Floquet-driven systems. Finally, a concrete theoretical proposal for detecting topological phase transitions in double kicked atom-optics kicked rotors with internal spin-1/2 degree of freedom is presented. Its implementation utilizes a kicked Bose-Einstein condensate evolving in one-dimensional momentum space. To reduce the influence of atom loss and phase decoherence, possible techniques to keep experimental durations short while maintaining a resonant experimental protocol are presented. Experimental limitations induced by phase noise, quasimomentum distributions, symmetries, and the ac-Stark shift are considered. These results thus suggest a feasible and optimized procedure for observing topological phase transitions in quantum kicked rotors.

TABLE OF CONTENTS

LIST OF TABLES

LIST OF FIGURES

CHAPTER I

INTRODUCTION

1.1 Outline

Since the advent of quantum theory by Max Planck in 1900 many interesting and surprising discoveries have been made as well as many applications that have had major effects on everyday life. One of the first such applications was the discovery of the properties of semiconductors that lead to the prevalence of electronics and computers in our everyday lives. These computers often require searching for data within a stored database. To find the desired piece of data one must use a method to search each piece of data until the required data is found. Such a method is known as a search algorithm. Classical random walks have been used in such search algorithms and networks [12, 132]. These discoveries and applications also lead to the development of the field of information theory pioneered in the 1940s by mathematicians such as Turing, Shannon, and Van Neuman. In more recent decades starting primarily with Richard Feynman in the 1970s information theory has begun to be extended into the quantum realm. Such new and exciting phenomena and potential applications of quantum information include quantum walks, quantum search algorithms, quantum computing, and topological phenomena of quantum walks. In order to potentially utilize such phenomena in future applications it is necessary to study them to learn about their strengths and limitations. A very effective method of conducting such research is by using the Bose-Einstein Condensates (BECs) as a basis. This state of matter is useful for quantum information research because BECs consist of tens of thousands to around one hundred thousand atoms of a particular species with each atom assuming the same quantum state upon being prepared. This greatly aids in investigation as now measurements are taken

at the micrometer scale (10^{-6}m) rather than at the nanometer scale (10^{-9}) characteristic of the atomic scale. With BECs, numerous investigations of quantum information have been successfully conducted over the last couple of decades. However, one important limitation of utilizing BECs in this manner is the presence of spontaneous emission that causes decoherence or a loss of information during the experiments. Such spontaneous emission causes a loss of atoms in experiments with BECs that are conducted over longer periods of time. In QWs using BECs for instance, they can be carried out for up to around 10 to 15 steps until the effect of spontaneous emissions induced by the kicked rotor becomes detrimental. While this was adequate to observe the behavior of the QWs in our previous studies this may increase difficulties in future experiments where more applications of the kicked rotor increase the probability of spontaneous emission. In this thesis, we carefully investigate the effects of spontaneous emission on QWs utilizing an external source of light to induce spontaneous emission to test how robust our QWs were under such a light source that is tunable in both intensity and duration. This tunable source of light also provided an opportunity to investigate the quantum-to-classical transition behavior of our QWs and suggest a possible method of quantifying this transition. We also investigated the effects of light shift due to the atom optics kicked rotor (AOKR) used to generate the shift in QWs and possible future methods to "clean up" our QWs so that it could be carried out to greater number of steps. The results of these studies indicate that our QWs could be used to successfully realize further experiments to study topological phenomena, quantum search algorithm, and other aspects of quantum information.

1.2 A brief history

In our studies we used the quantum walk with a BEC as a basis to investigate the effects of spontaneous emission. As a result, it will be useful to briefly outline the history of quantum walk. The concept of a quantum random walk is quite recent as the first paper proposing the concept was from 1993 [2, 63]. This paper proposed a "coin" based on a spin-

$\frac{1}{2}$ particle constrained onto a one-dimensional line. This paper also proposed as possible experimental realizations the use of micromasers [83, 18]. In one of the papers mentioned [18] interestingly a two photon maser was realized using ^{85}Rb. A later paper by Agarwal *et al.* [1] proposed an improved version of the experimental method proposed in Aharonov's paper. It is also important to note that the original model proposed by Aharonov differs from the contemporary model of the quantum walk in two major ways. First, the position states are forming an orthogonal basis with the walker. Secondly, the original proposal would measure the state of the coin after each step while in contemporary models measurements are made after a number of steps are performed [90, 125]. The first experimental realizations of the quantum walk were done in 2009 using an ion trapped in phase space and optically trapped individual atoms [104, 62]. Other possible schemes to realize a QW involve the use of quantum circuits, nuclear magnetic resonance (NMR), and waveguides that can act as a Mach-Zehnder interferometer [125]. The possibility of utilizing a BEC in momentum space to realize a QW was first proposed by Chandrashekhar in 2006 [21] although it was proposed that a Raman kick could be used to realize the unitary shift operator. It wasn't until a decade later that Wimberger *et al.* proposed the QW using a ^{87}Rb BEC with the AOKR to realize the aforementioned kicks [117]. Such a QW was then shortly realized by [27, 26] in 2018 and it was stable up to about fifteen steps. Some of the applications of a quantum walk include quantum search algorithms [107, 51, 52, 11], quantum computing [91], and topological phenomena [135, 131, 68, 133]. They also possess faster hitting times compared to classical random walks [124, 77, 64]. To attempt to realize some of potential applications of these QWs it is important to analyze the robustness and quality of the walk. This was done by subjecting QWs to external interference from laser light of tunable intensity. This light introduced a spontaneous emission that increased the probability of atoms participating in QWs to leave the walks. We also considered the possibility of adding initial momentum states to our QWs as well as changing the operators of the walk to reduce the effects of light shift from the translation operator that creates a persistent artifact that negatively affects

the quality of the QW over larger numbers of steps.

1.3 Dissertation layout

In chapter 2 I describe in detail the theoretical aspects of QWs using BECs. This setup is what provides the basis for my project in studying spontaneous emission and effects of light-shift. Because our QWs use the Atom-optics kicked rotor (AOKR), quantum ratchet, and microwave spectroscopy to be successfully realized in experiment, these important components are also described in detail. The theoretical aspects of spontaneous emission as pertaining to QWs and the AOKR are also described in detail and theoretical predictions are discussed and presented. The theory AC Stark shift is presented and its effects on the AOKR and QWs are lastly discussed. In chapter 3 I present the aspects of the experimental setup and the standard protocols used in obtaining the experimental data that is presented and analyzed in this dissertation. Detailed schematics of the optical tables and relevant equipment are presented and discussed in detail. The standard protocol of creating BECs that are utilized in my experiments is outlined in detail. In chapter 4 the results of my experiments are presented and discussed in detail. The robustness of QWs under external spontaneous emission perturbation is analyzed and the detection of the quantum-to-classical transition in QWs is explored. Simulations of the effects of light shift are also presented here along with a discussion of possible methods to reduce the effects of light-shift on our QWs to realize QWs that more closely resemble ideal behavior.

CHAPTER II

THEORETICAL ASPECTS OF QUANTUM WALKS AND SPONTANEOUS EMISSION

2.1 Introduction

In this chapter we will discuss the theoretical background of the quantum walk in general as well as the theory in realizing such a walk using the BEC in momentum space with an AOKR as the translation operator and the theory of utilizing microwave pulses to realize the quantum coin. As was discussed in the introduction, regardless if we are considering a classical or quantum walk they can both be classified as discrete or continuous in time. In the classical case examples of the discrete case include the so-called drunkard's walk along a line [96] or a random walk along a circle [116] while such phenomena as Brownian motion [71] are described by the continuous case. For our quantum walks we only considered discrete walks although continuous walks have been realized in experiments [122, 126].

2.2 Theory of Quantum Walk

In this section we will first describe the general basic properties of the quantum walk as well as its distribution. We then will detail the derivation of the Bloch equations necessary for the description of a two level system using two hyperfine levels of alkali atoms in the presence of on resonance radiation. A useful model to help visualize the transition of this system is introduced via the Bloch vector and Bloch sphere which will be helpful in the derivation of the results of Rabi oscillations. Hereafter we then describe the theory of the AOKR necessary for the realization of the momentum space translation operator of the quantum walk. Lastly,

we will outline the theory of spontaneous emission and apply this to the quantum walk and discuss the predicted results.

2.2.1 Concept of a Quantum Walk

Let's consider the simple case of a quantum walk on line in which our coin becomes a quantum coin or qubit [90, 125, 63]. Now let the two possible states of our quantum coin be $|1\rangle$ and $|2\rangle$ and consider an application of a quantum coin denoted by the operator $\hat{\boldsymbol{M}}$. This then results in an equal superposition of our states giving us the following matrix representation [90]

$$\hat{\boldsymbol{M}} = \frac{1}{\sqrt{2}} \begin{bmatrix} 1 & i \\ i & 1 \end{bmatrix}. \tag{2.2.1}$$

Now if we let $|1\rangle = \left[\begin{smallmatrix} 0 \\ 1 \end{smallmatrix}\right]$ and $|2\rangle = \left[\begin{smallmatrix} 1 \\ 0 \end{smallmatrix}\right]$ and apply the operator defined in Eq. 2.2.1 then we have [90]

$$\begin{aligned} \hat{\boldsymbol{M}}|1\rangle &= \frac{1}{\sqrt{2}} \begin{bmatrix} i \\ 1 \end{bmatrix} \\ \hat{\boldsymbol{M}}|1\rangle &= \frac{1}{\sqrt{2}} \left(|1\rangle + i|2\rangle\right). \end{aligned} \tag{2.2.2}$$

If we simply measured the state at this point and moved left or right along the line depending upon this result then we arrive at the same results of the classical walk as described in the Introduction. However, if instead we treat our walker as a quantum system and apply our quantum walk where the coin operator is applied and the walker will move to the right if the state is $|1\rangle$ and to the left if $|2\rangle$. This process is a step for the quantum walker and is given by $\hat{\boldsymbol{U}}_{\text{step}} = \hat{\boldsymbol{T}}\hat{\boldsymbol{M}}$ where $\hat{\boldsymbol{M}}$ and $\hat{\boldsymbol{T}}$ are the coin and momentum shift operator respectively [63, 26]. The direction of this shift operation is determined by the result of the quantum coin. If the initial state of our quantum system is given by $|\psi_0\rangle$ and if the quantum

walk is applied t number of steps then the state of the system is then [90]

$$|\psi_t\rangle = \left(\hat{\boldsymbol{U}}_{\text{step}}\right)^t |\psi_0\rangle. \tag{2.2.3}$$

The distribution of the walker produced by this process is dependent on the initial state of our system. If, for instance the initial state is $|1\rangle$ then the second step will have a nonzero mean showing that mean of the distribution can be nonzero. If we select the initial state to be $|\psi_0\rangle = \frac{1}{\sqrt{2}}(|1\rangle + |2\rangle)$ then we have quantum walk with a zero mean for any number of steps t. For the remainder of this discussion we will only consider this initial state. In contrast with the classical walk shown in Table 1 [90], the probability p of the walker being in a position, n after a number of steps t we can see that the terms are not terms from Pascal's triangle as shown [90] in Table 2 [90] with the first four states of $|\psi_t\rangle$.

t/d	-4	-3	-2	-1	0	1	2	3	4
0					1				
1				$\frac{1}{2}$	0	$\frac{1}{2}$			
2			$\frac{1}{4}$	0	$\frac{1}{2}$	0	$\frac{1}{4}$		
3		$\frac{1}{8}$	0	$\frac{3}{8}$	0	$\frac{3}{8}$	0	$\frac{1}{8}$	
4	$\frac{1}{16}$	0	$\frac{4}{16}$	0	$\frac{6}{16}$	0	$\frac{4}{16}$	0	$\frac{1}{16}$

Table 1: Probability of finding a classical walker at a position d after t steps.

During the quantum walk the coin is not measured after each individual step but instead quantum correlations between the different positions are kept and are allowed to interfere in the proceeding steps. It is this interference that gives rise to the distinctly peculiar behavior of the quantum walk. Indeed, if we take the distribution of the quantum walk after numerous steps we can see that the resulting distribution has the appearance of horn-like maxima along the edges of the distribution that widens ballistically as the number of steps increases. A numerical simulation of this after $t = 100$ steps is shown [90] in Fig. 1

Because of this behavior it is clear that the calculation of the standard deviation, σ_q is not trivial. In spite of this, it is shown by numerical calculations [121] that this standard deviation is nearly independent of the initial state of the quantum walker and is approximately linear,

t/d	-4	-3	-2	-1	0	1	2	3	4
0					1				
1				$\frac{1}{2}$	0	$\frac{1}{2}$			
2			$\frac{1}{4}$	0	$\frac{1}{2}$	0	$\frac{1}{4}$		
3		$\frac{1}{8}$	0	$\frac{1}{8}$	0	$\frac{5}{8}$	0	$\frac{1}{8}$	
4	$\frac{1}{16}$	0	$\frac{1}{8}$	0	$\frac{1}{8}$	0	$\frac{5}{8}$	0	$\frac{1}{16}$

Table 2: Probability of finding a quantum walker at a position d after t steps. Note that this walk is asymmetric when compared to the classical walk presented in Table 1.

i.e., $\sigma_q \approx t$.

Next we will discuss the details of realizing the discrete-time quantum walk in momentum space. Understanding the properties of this quantum walk is important if one wishes to apply the walk to various applications. In the experiments that we conduct a coin operator, $\hat{\boldsymbol{M}}$ is used to produce a superposition of two internal states of ^{87}Rb. To translate the atoms in momentum space a unitary shift operator, $\hat{\boldsymbol{T}}$, is applied. These two operators then produce a step of each walk as was discussed at the beginning of this section, $\hat{\boldsymbol{U}}_{\text{step}} = \hat{\boldsymbol{M}}\hat{\boldsymbol{T}}$.

2.2.2 Rabi Pulses and Coin Operator

To realize a quantum coin with a BEC of alkali atoms it is necessary to have precise control over a pair of internal states. This effectively creates a spin-1/2 system that can then be used to create the quantum coin. In ^{87}Rb this is accomplished by using microwave radiation that is resonant on two states in the $\left(5^2S_{1/2}\right)$ ground hyperfine levels. These states under consideration are the $|F = 1, m_F = 0\rangle$ and $|F = 2, m_F = 0\rangle$ hyperfine levels which following the works [27, 26] are denoted as $|g\rangle$ and $|e\rangle$ for ground and excited state respectively. In order to understand how to use these states to realize the superposition of states for the quantum coin it is necessary to understand the physics behind this microwave transition which in turn requires some understanding of Bloch vectors, Bloch sphere, and Rabi oscillations.

The hyperfine levels under consideration are due to an interaction between the spins of the electron and nucleus and this interaction causes the ground state to split into two levels [115] with a difference in frequency of several GHz. If one approaches the system in a

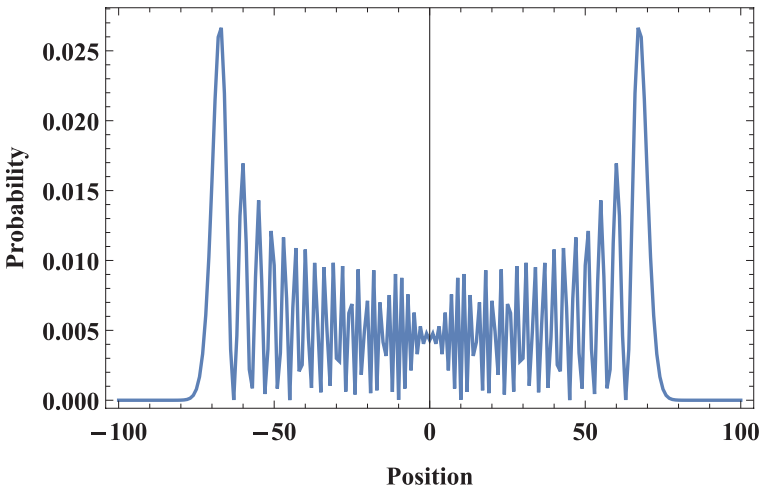

Figure 1: Numerical simulation of a quantum walk after $t = 100$ steps with up to $n = 100$ positions calculated using code adapted from Portugal [90]. Note the distinctive "horns" compared with the Gaussian distribution of the classical walk.

semi-classical manner in which the incident microwave radiation is considered as a classical radiation field and the two states, $|g\rangle$ and $|e\rangle$ are considered as a two-level system then the theoretical analysis becomes more manageable [3]. This is because the quantum physics of a two-level system is well understood [35].

We can begin our discussion by considering the time-dependent interaction described by the Hamiltonian[42]

$$\hat{\mathcal{H}} = \hat{H}_0 + \hat{H}_I(t), \tag{2.2.4}$$

where $\hat{H}_0$ and $\hat{H}_I$ are the stationary atomic and time-dependent terms respectively. If this Hamiltonian interacts on a two level system then the state of the system after a time t can be written as [35, 47]

$$|\psi(t)\rangle = a(t)|e\rangle + b(t)|g\rangle, \tag{2.2.5}$$

where the ket vectors on the right hand side are the aforementioned hyperfine levels. Since we are considering microwaves interacting with atoms we can quantitatively describe the electric and magnetic effects. Because of the symmetry of the hyperfine S states we can neglect the effects of the electric dipole and thus leave only magnetic interactions to be considered. The situation can be further simplified if we consider the fact that if we limit

ourselves to transitions where $\Delta m = 0$ then the treatment resembles that of the electric dipole. With these assumptions in mind we can then rewrite Eq. 2.2.4 as [43]

$$\hat{\mathcal{H}} = \hat{H}_0 - \sum_q \hat{\boldsymbol{\mu}}_q \cdot \hat{\boldsymbol{B}}(r_0), \tag{2.2.6}$$

here the second term on the right member of Eq. 2.2.6 contains the magnetic field operator $\hat{\boldsymbol{B}}$ at a point r_0 and the sum $\sum_q \hat{\boldsymbol{\mu}}_q$ represents the complete magnetic dipole moment operator. This operator takes into account the contributions from the orbital ($\hat{L}$) and spin ($\hat{S}$) momenta of the valence electron and the angular momentum from the nucleus ($\hat{I}$) respectively. These contributions can then be written as [73]

$$\sum_q \hat{\boldsymbol{\mu}}_q = \hat{\boldsymbol{\mu}}_L + \hat{\boldsymbol{\mu}}_S + \hat{\boldsymbol{\mu}}_I. \tag{2.2.7}$$

We can represent these operators in terms of the Pauli spin matrices as shown below

$$\hat{H}_0 = \frac{\hbar\omega_0}{2}\hat{\sigma}_z \tag{2.2.8}$$

$$\hat{\boldsymbol{u}} = \hat{\boldsymbol{\mu}}_r\hat{\sigma}_x - \hat{\boldsymbol{\mu}}_i\hat{\sigma}_y, \tag{2.2.9}$$

here the subscripts r and i represent the radial and angular integrals specific to a particular problem at hand [3]. Because we are only considering $\Delta m = 0$ transitions the second term in the left member of Eq. 2.2.9 will vanish because of the aforementioned symmetry and thus we will only have the radial part to consider [38]. We can also neglect the contributions from orbital spin angular spin momenta because the interaction is between the two S states, thus $L = 0$. As a result of this analysis then we have [44, 3]

$$\hat{\mathcal{H}} = \frac{\hbar\omega_0}{2}\hat{\sigma}_z - \left(\hat{\boldsymbol{\mu}}_r \cdot \hat{\boldsymbol{B}}\right)\hat{\sigma}_x. \tag{2.2.10}$$

If we work in the Heisenberg picture it becomes relatively simple to calculate the evolution

of the Pauli matrices with the following commutation relation [3, 44]

$$i\hbar\dot{\hat{\sigma}}_j = \left[\hat{\sigma}_j, \hat{\mathcal{H}}\right]. \tag{2.2.11}$$

Expanding this commutation relation results in the system of coupled differential equations [3, 44]

$$\begin{aligned}
\dot{\hat{\sigma}}_x(t) &= -\omega_0 \hat{\sigma}_y(t) \\
\dot{\hat{\sigma}}_y(t) &= \omega_0 \hat{\sigma}_x(t) + \frac{2}{\hbar}\left(\boldsymbol{\mu}_r \cdot \hat{\boldsymbol{B}}\right)\hat{\sigma}_z(t) \\
\dot{\hat{\sigma}}_z(t) &= -\frac{2}{\hbar}\left(\boldsymbol{\mu}_r \cdot \hat{\boldsymbol{B}}\right)\hat{\sigma}_y(t).
\end{aligned} \tag{2.2.12}$$

For convenience we can neglect the quantum interactions between the atom and the applied microwave radiation field at a high power as this enables us to treat the incident microwave radiation as a classical wave and it also allows us to consider the expectation values of the Pauli matrices [3, 44]

$$s_j = \left(\langle\psi(t)|\hat{\sigma}_j|\psi(t)\rangle\right). \tag{2.2.13}$$

This also has the additional advantage where the expectation values of surviving operator products can be readily calculated. The results of Eq. 2.2.13 can then be expanded in the following system of differential equation that, although are still coupled, are also slightly more simple than in Eq. 2.2.12 [3, 44]

$$\begin{aligned}
\dot{s}_1(t) &= -\omega_0 s_2(t) \\
\dot{s}_2(t) &= \omega_0 s_1(t) + \frac{2}{\hbar}\left(\boldsymbol{\mu}_r \cdot \boldsymbol{B}\right) s_3(t) \\
\dot{s}_3(t) &= -\frac{2}{\hbar}\left(\boldsymbol{\mu}_r \cdot \hat{\boldsymbol{B}}\right) s_2(t).
\end{aligned} \tag{2.2.14}$$

We can also assume that the microwave radiation is linearly polarized and enables us to write [3]

$$\left\langle \hat{\boldsymbol{B}}(t,0) \right\rangle = \boldsymbol{B}_0 \cos(\omega t) = B_0 \cos(\omega t)\boldsymbol{z}. \tag{2.2.15}$$

With all of these derived results we are now in a position to derive the optical Bloch equations for microwave spectroscopy. The form of these equations vary depending upon the system under consideration. We have already seen a version of these equations in Chapter 2 in the analysis of laser cooling for example. Now, we introduce a further convenience in applying the rotating wave approximation where we consider a reference frame that rotates with a frequency ω that matches the frequency of the microwaves. Also, note that the coupled equations in Eq. 2.2.14 show the s vector will trace out a path on a unit sphere. We will see that such an observation will be very useful in interpreting these equations as they are very difficult to solve directly. Thus it is necessary to make further simplifications using theory of Rabi oscillations as we will discuss next.

Let's consider the interaction term from Eq. 2.2.4 and calculate its terms in terms of the stationary part [127, 44]

$$\hat{H}_I = V_{i,j} = \langle \psi_i | \hat{H}_I | \psi_j \rangle. \tag{2.2.16}$$

Applying the reduced interaction term this then becomes [127, 44]

$$V_{i,j} = \langle e | - \left(\hat{\boldsymbol{\mu}} \cdot \hat{\boldsymbol{B}} \right) | g \rangle = \frac{\hbar}{2} \Omega, \tag{2.2.17}$$

where Ω is again the Rabi frequency. Because we are able to factor the operator products and determine each expectation value we recover the interaction under consideration. Now let's write the radial term $\hat{\boldsymbol{\mu}}_r$ in terms of the Bohr magneton, $\mu_B = \frac{e\hbar}{2m_e}$ and Lande g-factor g_q [127, 44]

$$\hat{\boldsymbol{\mu}}_q = \frac{\mu_B g_q \boldsymbol{q}}{\hbar}. \tag{2.2.18}$$

Because we have already aligned the system along the z-axis as implied in Eq. 2.2.15 we will maintain this orientation and rewrite the interaction term as [127, 44]

$$\hat{H}_I = \frac{B_0}{\hbar} \left(\mu_B g_S S_z + \mu_B g_I I_z \right) \cos(\omega t). \tag{2.2.19}$$

Applying Eq. 2.2.19 to Eq. 2.2.17 results in the rather intimidating expression [127, 44]

$$\begin{aligned} V_{i,j} &= \langle g|\hat{H}_I|e\rangle \\ &= \langle F=1, m_F=0|\frac{B_0}{\hbar}\left(\mu_B g_S S_z + \mu_B g_I I_z\right)\cos(\omega t)|F=2, m_F=0\rangle \\ &= \frac{B_0}{2\hbar}\cos\omega t\langle F=1, m_F=0|\mu_B g_S S_z + muBg_I I_z|F=2, m_F=0\rangle. \end{aligned} \tag{2.2.20}$$

The last line of Eq. 2.2.20 can be successfully evaluated by the use of Clebsch-Gordon coefficients using the basis $\{I_z, S_z\}$ and for the $|F=1, m_F=0\rangle \leftrightarrow |F=2, m_F=0\rangle$ transition [127, 26, 44]. Using these coefficients we can rewrite the angular momentum vectors as

$$|1,1\rangle = \sqrt{3}/2|3/2,-1/2\rangle - 1/2|1/2,1/2\rangle, \tag{2.2.21}$$

and

$$|2,1\rangle = 1/2|3/2,-1/2\rangle - \sqrt{3}/2|1/2,1/2\rangle. \tag{2.2.22}$$

Therefore we have [44, 127, 26]

$$\begin{aligned} \langle 1,1|\hat{H}_I|2,1\rangle &= -\frac{\mu_B\left\langle\hat{\boldsymbol{B}}(t,0)\right\rangle}{\hbar}\langle 1,1|g_s + g_I I_z|2,1\rangle \\ &= \frac{\sqrt{3}\mu_B B_0\cos(\omega t)}{4}\left(g_S - g_I\right). \end{aligned} \tag{2.2.23}$$

Now we use the fact that $\langle 1,1|\hat{H}_I|2,1\rangle = \langle 1,-1|\hat{H}_I|2,-1\rangle$ and perform a similar calculation for the other $\Delta m = 0$ transition [44, 127, 26]

$$|1,0\rangle = \sqrt{2}/2|1/2,-1/2\rangle - \sqrt{2}/2|-1/2,1/2\rangle, \tag{2.2.24}$$

and

$$|2,0\rangle = \sqrt{2}/2|1/2,-1/2\rangle + \sqrt{2}/2|-1/2,1/2\rangle. \tag{2.2.25}$$

We therefore arrive at [127, 44, 26]

$$\begin{aligned}\langle 1,0|\hat{H}_I|2,0\rangle &= -\frac{\mu_B\left\langle \hat{\boldsymbol{B}}(t,0)\right\rangle}{\hbar}\langle 1,0|g_s+g_I I_z|2,0\rangle \\ &= \frac{\mu_B B_0\cos(\omega t)}{2}\left(g_S-g_I\right).\end{aligned} \tag{2.2.26}$$

Now that we have found the matrix elements of the interaction term we can determine the Rabi frequency that represents the interaction potential. If we assume that our system is in the ground state initially and that the microwave radiation possesses a detuning of $\delta=\omega-\omega_0$ and also note that the diagonal terms $V_{ee}=V_{gg}=0$ and that $V_{ge}=V_{eg}^*$ we can write the population of the excited state in terms of the Rabi frequency [26, 127, 44]

$$P_e(t)=\frac{|\Omega|^2}{2\bar{\Omega}^2}\left(1-\cos(\bar{\Omega}t)\right), \tag{2.2.27}$$

where $\bar{\Omega}=\sqrt{|\Omega|^2+\delta^2}$ is the generalized Rabi frequency [42]. It is predicted by Eq. 2.2.27 that the population will show oscillations between the excited and ground states with a rate determined by the generalized Rabi frequency. Using the results of Eqs. 2.2.23,2.2.26, and 2.2.17 we obtain [26, 44, 127]

$$\begin{aligned}\Omega_0 &= \frac{\mu_B B_0}{\hbar}\left(g_S-g_I\right) \\ \Omega_1 &= \frac{\sqrt{3}\mu_B B_0}{2\hbar}\left(g_S-g_I\right).\end{aligned} \tag{2.2.28}$$

The results of the equations in Eq. 2.2.28 allow us to simplify the system in Eq. 2.2.14 into a more manageable form by applying the rotating wave approximation as well as introducing the concept of a Bloch vector.

The modification of Eq. 2.2.14 allows us to represent the rate of change of vector $\boldsymbol{s}$ in terms of a torque $\boldsymbol{\Omega}^F(t)$ [3]

$$\frac{d}{dt}\boldsymbol{s}=\boldsymbol{\Omega}^F(t)\times\boldsymbol{s}(t). \tag{2.2.29}$$

When we consider Eq. 2.2.29 it can be shown[3] that a component of this torque oscillates

very rapidly and is thus nearly ineffective. As a result, we can neglect this term in the rotating wave approximation which then results in the following linear system of equations [3]

$$\begin{bmatrix} u \\ v \\ w \end{bmatrix} = \begin{bmatrix} \cos(\omega t) & \sin(\omega t) & 0 \\ -\sin(\omega t) & \cos(\omega t) & 0 \\ 0 & 0 & 1 \end{bmatrix} \begin{bmatrix} s_1 \\ s_2 \\ s_3 \end{bmatrix}. \tag{2.2.30}$$

The results of Eq. 2.2.30 can then be expanded to give with δ again representing the detuning [3]

$$\begin{aligned} \dot{u} &= -\delta v \\ \dot{v} &= \delta u + \Omega w \cdot \\ \dot{w} &= -\Omega v \end{aligned} \tag{2.2.31}$$

Now that we can see that the variables u, v, and w govern the dynamics of the system we can introduce a new vector $\boldsymbol{\rho} = (u, v, w)$ known as the Bloch vector[3, 73]. Before completing the derivation of the coin operator it is necessary to digress and describe the properties of the Bloch vector as well as the Bloch sphere. The Bloch sphere was first introduced by Felix Bloch in 1946 in relation to nuclear magnetic resonance [13] and very recently a quantum walk has been proposed that occurs entirely on such a sphere [37]. The concept of such a vector can also be used to describe Stokes parameters of polarization states in optics where it is also known as the Poincare[1] sphere[113]. As was observed earlier Eq. 2.2.31 trace a path along a unit sphere known as the Bloch sphere. This result provides a convenient method to determine the state of the system at any particular time by knowing the location of the Bloch vector on this sphere. If we define the Bloch sphere in such a way where our states $|g\rangle$ and $|e\rangle$ are located on the north and south poles on the sphere respectively[26, 134] and

[1]Briefly, if we consider two polarization states $|L\rangle$ and $|R\rangle$ as lying at the south and north poles of a unit sphere respectively and any general state $|E\rangle$ then the position of this state on the Poincare sphere is then $|E\rangle = ae^{-i\phi/2} + be^{i\phi/2}$. Note that if the vector $|E\rangle$ is at a pure state then the components satisfy $P_1^2 + P_2^2 + P_3^2 = 1$ where P_i represent the Stokes parameters. This can be seen to have a very similar form and behavior to Eq. 2.2.32.

the state of our system with the vector $|\psi\rangle$ as shown in Fig. 2 [127, 26]. The state vector

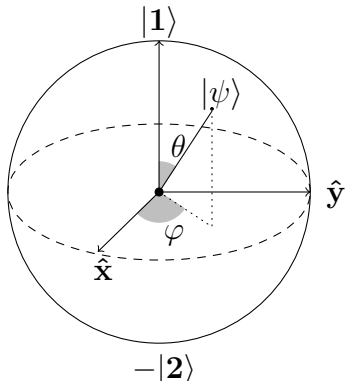

Figure 2: A Bloch sphere where the state vector position is $|\psi\rangle$ and the angles θ and ϕ represent the usual polar and azimuthal angles from spherical coordinates.

$|\psi\rangle$ is defined as[127, 42]

$$|\psi\rangle = \cos(\theta/2)|g\rangle + e^{i\phi}\sin(\theta/2)|e\rangle. \tag{2.2.32}$$

To arrive at Eq. 2.2.32 let's consider a general vector [134]

$$|\psi\rangle = c_0|0\rangle + c_1|1\rangle, \tag{2.2.33}$$

rewriting this in polar form we have

$$c_0 = r_0 e^{i\phi_0}, \tag{2.2.34}$$

and

$$c_1 = r_1 e^{i\phi_1}. \tag{2.2.35}$$

Giving us for the original vector [134],

$$|\psi\rangle = r_0 e^{i\phi_0}|0\rangle + r_1 e^{i\phi_1}|1\rangle. \tag{2.2.36}$$

Although we have four unknowns in Eq.2.2.36 we can consider the fact that a state doesn't change if we multiply by a complex number with a modulus of one. Doing so will eliminate

the phase of $|0\rangle$ giving [134].

$$ce^{-i\phi_0}|\psi\rangle = r_0|0\rangle + r_1 e^{i(\phi_1-\phi_0)} \tag{2.2.37}$$

Now if we consider that $1 = |r_0|^2 \left|e^{i\phi_0}\right|^2 + |r_1|^2 \left|e^{i\phi_1}\right|^2$ thus giving $r_0^2 + r_1^2 = 1$. Letting these be $r_0 = \cos(\theta/2)$ and $r_1 = \sin(\theta/2)$ results in Eq.2.2.32. The time evolution of our system is thus determined by the angles θ and ϕ. As was mentioned before the angles represent the usual spherical coordinates and thus a relation between the coordinates of the Bloch sphere with Cartesian coordinates can be readily written as[127]

$$\boldsymbol{\rho} = (u, v, w) = (\sin(\theta)\cos(\phi), \sin(\theta)\sin(\phi), \cos(\theta)) \,. \tag{2.2.38}$$

Further physical interpretations can be obtained by considering that the population of the states can be gathered by considering how the component w varies from -1 (all atoms in excited state) to 1 (all are in the ground state) where $P_g = {}^{(1+w)}/_2$ and $P_e = {}^{(1-w)}/_2$ indicating that the system is purely in the ground and excited states respectively [26]. While the other components, u and v represent coherence or mixing of the states. For the state vector to represent a pure state on the Bloch sphere the components of the Bloch vector must satisfy the condition: $u^2 + v^2 + w^2 = 1$. If we have a mixed state then the Bloch vector will precess inside of the Bloch sphere.

Having introduced and discussed the Bloch vector and sphere we can now derive the microwave coin operator when we consider a special type of rotation of the Bloch vector known as Rabi rotations. If we consider microwaves that are on resonance with the transition the detuning in Eq. 2.2.31 will then vanish giving rise to case where the solutions become a rotation [3]

$$\boldsymbol{\rho} = \hat{\Theta}(t)\boldsymbol{\rho}_0. \tag{2.2.39}$$

And as a result the systems of equations will then become letting $\theta(t) = \Omega t$ [3]

$$\begin{bmatrix} u \\ v \\ w \end{bmatrix} = \begin{bmatrix} 1 & 0 & 0 \\ 0 & \cos(\theta(t)) & \sin(\theta(t)) \\ 0 & -\sin(\theta(t)) & \cos(\theta(t)) \end{bmatrix} \begin{bmatrix} u_0 \\ v_0 \\ w_0 \end{bmatrix}. \tag{2.2.40}$$

Using our vector state representation in the Bloch vector formalism a pulse of resonant microwave radiation of duration t can then be denoted by an application of the unitary operator $\hat{\boldsymbol{M}}(t)$ and thus we can write[26]

$$|\psi(t)\rangle = \hat{\boldsymbol{M}}(t)|\psi(0)\rangle. \tag{2.2.41}$$

A full derivation of this unitary operator is done in [73]

$$\hat{\boldsymbol{M}}(\theta(t), \chi) = \begin{bmatrix} cos(\theta(t)/2) & e^{-i\chi}\sin(\theta(t)/2) \\ -e^{i\chi}\sin(\theta(t)/2) & \cos(\theta(t)/2) \end{bmatrix}. \tag{2.2.42}$$

Here χ represents the offset phase of the applied microwave pulses and is very rarely adjusted in the experiments. If we set $\theta(t) = \pi/2$ and apply this $\pi/2$ pulse onto a system of atoms in the ground state then our Bloch will rotate to become [73]

$$\boldsymbol{\rho}_{\pi/2} = \begin{bmatrix} 1 & 0 & 0 \\ 0 & 0 & 1 \\ 0 & -1 & 0 \end{bmatrix} \begin{bmatrix} 0 \\ 0 \\ 1 \end{bmatrix} = \begin{bmatrix} 0 \\ 1 \\ 0 \end{bmatrix}. \tag{2.2.43}$$

So if all of the atoms are in the ground state then this $\pi/2$ pulse will transfer the atoms to the equator on the Bloch sphere corresponding to the v-direction. This then represents a population where the atoms are equally split into a superposition of the ground and excited

states. We can see this by applying Eq. 2.2.42 and setting $\theta(t) = \pi/2$ [26]

$$\begin{aligned} |\psi_{\pi/2}\rangle &= \hat{\boldsymbol{M}}(\pi/2, \chi)|g\rangle \\ &= \frac{1}{\sqrt{2}} \begin{bmatrix} 1 & e^{-i\chi} \\ -e^{i\chi} & 1 \end{bmatrix} \begin{bmatrix} 1 \\ 0 \end{bmatrix}. \\ &= \frac{1}{\sqrt{2}} \left(|g\rangle - e^{i\chi}|e\rangle\right) \end{aligned} \tag{2.2.44}$$

A similar derivation can be done when $\theta(t) = \pi$ where all of the atoms can be transferred from one pure state to another. In our work there are two specific microwave coin operators that very important and are denoted as the gate and coin pulses and have the form [26]

$$\hat{\boldsymbol{M}}(\pi/2, \pi) = \frac{1}{\sqrt{2}} \begin{bmatrix} 1 & -1 \\ 1 & 1 \end{bmatrix}, \tag{2.2.45}$$

and the coin as

$$\hat{\boldsymbol{M}}(\pi/2, -\pi/2) = \frac{1}{\sqrt{2}} \begin{bmatrix} 1 & i \\ i & 1 \end{bmatrix}. \tag{2.2.46}$$

The gate pulse prepares an equal superposition of the initial states following the Bragg pulse and gives a symmetric QW and can be checked experimentally by measuring the population after applying the gate only and without an imaging pulse. A proper gate pulse will give half the population of the Bragg pulse as half the population will be in the $|g\rangle$ and $|e\rangle$ states. Next we will consider how to realize the translation operator using the AOKR.

2.2.3 Translation Operator (AOKR)

Here we will describe how to utilize the AOKR to realize the translation operator necessary for the quantum walk. Since it was first proposed in 1979 [22] and realized experimentally in 1995 [95], the AOKR has been well studied over the last few decades [94, 69, 5] and was the basis of the quantum ratchet which has been used in many studies [29, 9, 120, 110, 109,

111, 87, 86, 65, 102]. The shift operator is unitary and denoted by $\hat{\boldsymbol{T}}$ is given by [26]

$$\hat{\boldsymbol{T}} = e^{(i\hat{x}\Delta p)/\hbar}|1\rangle\langle 1| + e^{-(i\hat{x}\Delta p)/\hbar}|2\rangle\langle 2|, \tag{2.2.47}$$

where $\pm\Delta p$ is the shift in momentum of the atom and is dependent upon if the atom is in $|1\rangle$ or $|2\rangle$ internal states. Such an operator is realized in the experiment by using a quantum ratchet with the AOKR on quantum resonance. This quantum ratchet destroys the spatial-temporal symmetry in the process [99, 101, 45]. The derivation of the AOKR and its properties are outlined in the appendix but we present the Hamiltonian with the constant phase term here as [101]

$$H(\hat{X}, \hat{P}, t) = \frac{\hat{P}^2}{2M} + \hbar\phi_d \cos(1 + G\hat{X}) \sum_{q=0}^{t} \delta(t - qT). \tag{2.2.48}$$

The kicking strength in terms of the Rabi frequency, time duration of the light pulse, and detuning of the laser from the atomic transition is $\phi_d = \frac{\Omega^2 \Delta t}{8\delta_L}$. For convenience in the upcoming theoretical discussions we express Eq. 2.2.48 in dimensionless variables by making the following scaling operations and letting $\mathcal{H} = \frac{MH}{\hbar^2 G^2}$, $t' = \frac{2\pi t}{T_{(1/2)}}$, $\hat{p} = \frac{\hat{P}}{\hbar G}$, $\tau = \frac{2\pi T}{T_{(1/2)}}$, and $\hat{x} = G\hat{X}$ where $T_{(1/2)} = \frac{2\pi M}{\hbar G^2}$ is the half Talbot time. The Talbot time is the period of the AOKR and is named after Henry Talbot as it is an analogy in time to the optical effect he discovered in the 1830s [119]. After this rescaling the Hamiltonian in Eq. 2.2.48 then becomes [26]

$$\hat{\mathcal{H}} = \frac{\hat{p}^2}{2} + \phi_d \left(1 + \cos(\hat{x})\right) \sum_{j=0}^{t} \delta(t - j\tau). \tag{2.2.49}$$

The momentum operator $\hat{p}$ in the AOKR in the form given by Eq. 2.2.49 consists of two parts, an integer multiple of the photon recoil with units of $\hbar G$ and a quasi-momentum part denoted by β is a real number where $\beta \in [0, 1)\hbar G$ thus $\hat{p} = \hat{n} + \beta$ [48]. The quasi-momentum is conserved due to the fact that non-integer transitions in momentum are forbidden, this is due to the applied potential being periodic in space with a period of $\lambda_G = {}^{2\pi}/_{G}$. It

also describes the width of the BEC and is approximately a Gaussian distribution that is determined from the parameters of the experiment. The integer part of the momentum are given by the eigenvalues of the angular momentum operator $\hat{n} = -i\frac{\partial}{\partial\theta}$. The periodic nature of this potential provides the boundary conditions of the position operator $\hat{x}$ such that it becomes 2π periodic thus we can relate it with the angle operator $\hat{\theta}$ using the modulo relation $\hat{\theta} = \hat{x} \cdot \mathrm{mod}(2\pi)$ [48]. This results in the solutions being invariant after an application of the periodic potential and thus we can now apply Bloch's theorem [54, 48] to our problem. Also, since the pulse duration is finite it must be kept shorter than the period between the pulses, a limitation known as the Raman-Nath limit [46, 79]. With these conditions the Floquet operator is then [48, 108, 26, 102]

$$\hat{\mathcal{U}}(\tau) = \hat{U}_{free}\hat{U}_{kick} = e^{-\frac{i\tau(\hat{n}+\beta)^2}{2}}e^{-i\phi_d(1+cos\hat{\theta})}. \tag{2.2.50}$$

The constant term of the kick part of Eq. 2.2.50 represents an offset due to the applied kicking light and it represents a phase shift that affects the entire quantum walk. The periodic part of this operator represents an atomic grating effect as we will show. If we start with a BEC in the initial state $|\psi_j\rangle$ before a kick pulse is applied and let $|\psi_{j+1}\rangle$ then this kick operator acts on the state in the following manner after a single pulse [48, 26, 108, 102]

$$|\psi_{j+1}\rangle = \hat{U}_{kick}|\psi_j\rangle = e^{-i\phi_d\cos(\hat{\theta})}|\psi_j\rangle. \tag{2.2.51}$$

Now we must work out the dynamics of Eq. 2.2.51 by making use of an identity to evaluate the complex exponential term, $e^{-i\cos\hat{\theta}}$ known as the Jacobi-Anger relation[2], $e^{ix\cos(\theta)} = \sum_{m=-\infty}^{+\infty} i^m J_m(x)e^{im\theta}$. Applying this relation to Eq. 2.2.51 yields [26, 108, 85]

$$|\psi_{t+1}\rangle = \sum_m (-i)^m J_m(\phi_d)|p_m\rangle, \tag{2.2.52}$$

[2]This relation is derived from a generating function that in turn is from Bessel functions of integral order. This generating function is $e^{(x(t\,-\,1/t))/2} = \sum_{m=-\infty}^{+\infty} t^m J_m(x)(t \neq 0)$. Setting $t = e^{i\theta}$ arrives at a similar expression with the sine function[19].

here $J_m(x)$ is the m^{th} order Bessel function of the first kind and $|p_m\rangle = e^{-im\hat{\theta}}$ is a momentum order in the atomic grating direction of $p_m = m\hbar G$ where G is the grating wave vector due to the standing waves generated from the kicking beams. The Bessel function gives us the coupling amplitudes between the initial momentum state, n and a later state, m. As is well known these[59] functions will decay rapidly when their difference $|m - n|$ increases. Moreover, when $\phi_d \approx 1$ in the AOKR then only the nearest momenta states will be coupled in such a way where $m = n \pm 1$. To realize the standing wave pulses used in applying the kicking potential to the BEC two counter-propagating laser beams that are linearly polarized and possess a Gaussian profile with an intensity I_k are used. The finer experimental details of such a setup are discussed in Chapter 4 but we will present the underlying theory here following Derevianko [34]. Let the intensity nodes of the standing wave, λ_G, be given by

$$\lambda_G = \frac{\lambda}{2\sin(\theta_k)}, \tag{2.2.53}$$

where θ_k being the angle between respective kicking beams with respect to the vertical. The optical potential imposed on an atom is given by [34]

$$U(r,z) = U_0 e^{-2(r/w)^2} \cos^2\left(2\pi z/\lambda_G\right). \tag{2.2.54}$$

where w the beam waist along the z-axis, r the radial axis from the center of the beam. Here U_0 is the depth of the potential and is given by [34, 26]

$$U_0 = -\frac{8\pi}{c}\alpha_g(\omega) I_k, \tag{2.2.55}$$

where $\alpha_g(\omega)$ is the polarizability of the ground state and is given by [26]

$$\alpha_g(\omega) = |\langle g|\boldsymbol{D}\cdot\hat{\epsilon}|e\rangle|^2 \left(\frac{2\omega}{\omega^2 - \omega_0^2}\right). \tag{2.2.56}$$

Here $|g\rangle$ and $|e\rangle$ are the ground and excited respectively states of the atoms separated by frequency ω_0, the laser frequency is ω, $\boldsymbol{D}$ is the electric dipole matrix, and $\hat{\epsilon}$ is the polarization vector. When a very short pulse of this wave is applied the atoms will then undergo diffraction to different momenta states as governed by Eq. 2.2.52. Now we discuss an important case with the AOKR and that is where the time between the pulses are set to what is known as quantum resonance. Applying the Floquet operator described by Eq. 2.2.50 to the wave function of our system gives after j kicks gives the general evolution of the system

$$|\psi(j\tau)\rangle = \hat{\mathcal{U}}^j|\psi_0\rangle. \tag{2.2.57}$$

If we look again at the free evolution part of the Floquet operator we can see that if the kick period is set to $\tau = n4\pi$ where $n \in \mathbb{Z}$ then this free evolution will become unity and then the kicks will add coherently into one kick strength of $i \cdot \phi_d$. This special time period is known as the Talbot time T. Such a condition is known as quantum resonance and the Floquet operator then reduces to a form

$$\hat{\mathcal{F}} = \hat{U}^j_{\phi_d} = e^{-ij\phi_d \cos(\hat{\theta})}. \tag{2.2.58}$$

With this version of the Floquet operator we can now calculate the evolution of the system after an application of j kicks starting with an initial momentum state $|p_m = 0\rangle$ [26, 48]

$$\begin{aligned} p_n &= \left|\langle n|\hat{U}^j|0\rangle\right|^2 \\ &= \left|\langle n|e^{-ij\phi_d \cos(\hat{\theta})}|0\rangle\right|^2 \\ &= J_n^2(j\phi_d). \end{aligned} \tag{2.2.59}$$

Now we can find the mean energy of the system [26, 48]

$$\begin{aligned}\langle E\rangle &= \sum_{n=-\infty}^{+\infty} n^2 p_n \\ &= \sum_{n=-\infty}^{+\infty} n^2 J_n^2(j\phi_d) \\ &= \frac{1}{2} j^2 (\phi_d)^2.\end{aligned} \tag{2.2.60}$$

These results show that after j kicks a state starting at zero momentum the mean energy will increase quadratically which is expected from quantum resonance [101]. Such behavior can be seen in the TOF images of panel (a) and the mean energy plot of panel (c) of Fig. 3. Another special case to consider is if the kicking period is half of the Talbot time, $T_{1/2}$ where $\tau = 2n\pi$. Now let's find the form of the wave function after applying the Floquet operator with this time period [48, 26]

$$\begin{aligned}|\psi(\tau = T_{1/2})\rangle &= e^{-i\frac{\hat{p}^2\tau}{2}} e^{-i\phi_d \cos(\hat{\theta})} |\psi_0\rangle \\ &= \sum_{n=-\infty}^{+\infty} (-i)^n J_n(\phi_d) e^{in\hat{\theta}} e^{-i\pi n^2} |\psi_0\rangle \\ &= \sum_{n=-\infty}^{+\infty} (i)^n J_n(\phi_d) e^{in\hat{\theta}} |\psi_0\rangle \\ &= e^{i\phi_d \cos(\hat{\theta})} |\psi_0\rangle.\end{aligned} \tag{2.2.61}$$

We can see that the resulting phase factor will vanish with the next applied kick leading to the atoms being placed back to the initial momentum state at each odd multiple of $\tau = 2\pi$. This occurs because two kicks possessing a period of $T_{1/2}$ cancel out and lead to an oscillation in mean energy as shown in Fig. 3. Such a condition is known as quantum anti-resonance [101] and is shown in panel (b) of Fig. 3. The Talbot time based on the experimental parameters is $T = 103.04$ μs. The AOKR setup can be used to realize a quantum version of a ratchet. The concept of a ratchet is a device that allows motion in only one direction. The quantum version of this is that changes of a system in momentum space is only allowed in one direction,

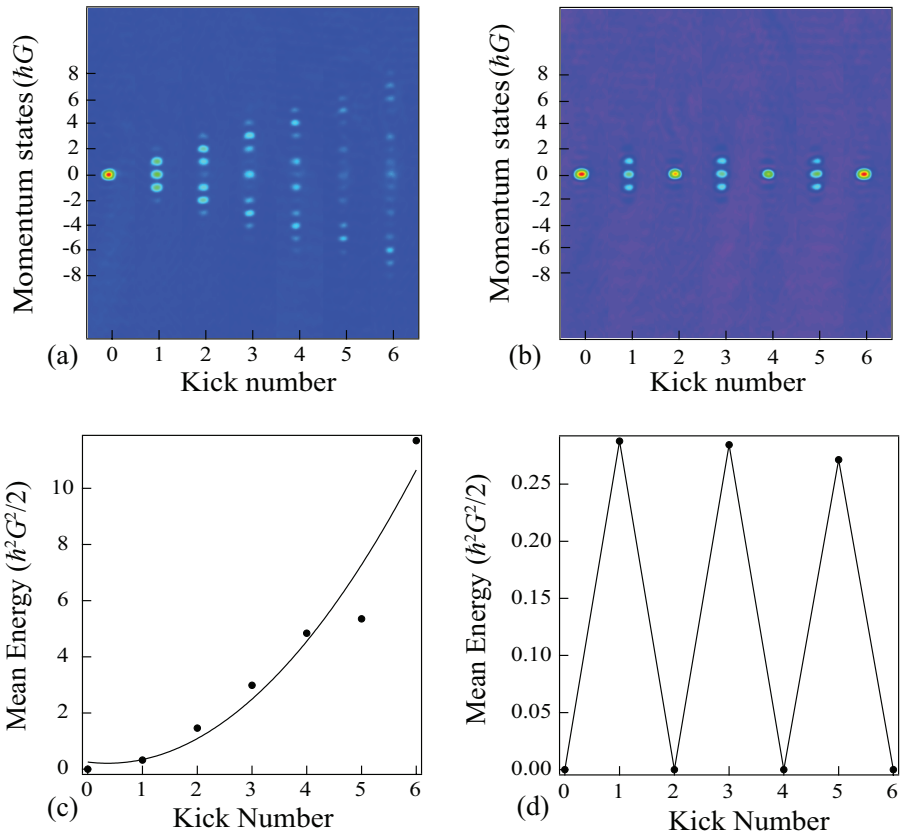

Figure 3: TOF images of AOKR with quantum resonance ($\tau = T$) in panel (a) and quantum anti-resonance ($\tau = T_{1/2}$) in panel (b). Panels (c) and (d) plot the mean energy extracted from (a) and (b) versus kick number. Note the quadratic behavior of (c) which is characteristic of quantum resonance in the AOKR.

i.e positive or negative momentum. If we consider that the gradient of the standing wave behaves as a driving force on the wave function of the atoms then it can be deduced that the wave function with greater potentials will result in a larger net force overall. This then will lead to a higher probability of quantum ratchet behavior[85]. The overall direction of the ratchet in momentum space is determined by the sign of the potential gradient near the maxima of the wave function of the atoms. To realize a quantum ratchet we need to prepare an initial state with multiple plane waves as described by [26, 87]

$$|\psi\rangle = \sum_n e^{-in\phi}|n\rangle. \tag{2.2.62}$$

Here $|n\rangle$ is the momentum state and the offset phase is given by ϕ which determines the strength of the potential gradient. If $\phi = \pi/2$ then this potential is at its maximum. If we make the assumption that the BEC initially possesses a narrow width in momentum space is[85, 26]

$$|\psi\rangle = \delta(p), \tag{2.2.63}$$

where $\delta(p)$ is the width of the BEC and p is the continuous momentum. If a Fourier transform is applied to the wave function transferring it to position space and can then be studied as a standing wave giving rise to the distribution [26] $|\phi(x)| = \sqrt{G/2\pi}$, this shows that a single BEC cannot be used to realize a ratchet as there will be no net force on the atoms. If, however, multiple initial states are prepared then it is possible to realize a ratchet. If we let the wave function of these states be represented by [87]

$$\phi(x) = A\sum_{n}^{m} e^{in\phi}e^{ip_n x/\hbar}, \tag{2.2.64}$$

where A is a normalization factor. A plot of $|\phi(x)|^2$ and the standing wave potential will show that the peaks of the wave function correspond to locations where the derivative of the standing wave is at maximum. Note also that if we have more initial momentum states the wave function will become more spatially localized, *i.e* lowering the FWHM, after a Fourier transformation. Thus this will lead to a more refined quantum ratchet. In realizing the quantum ratchet we have first prepared two or more initial momentum states as mentioned above. In all of the QW experiments we used the following initial states [26, 27]

$$|\psi_{\text{ratchet}}\rangle = \frac{1}{\sqrt{2}}\left(|n=0\rangle + i|n=1\rangle\right). \tag{2.2.65}$$

To do this we apply a Talbot time length, low intensity pulse Bragg pulse with the AOKR beams with the BEC starting at $|n=0\rangle$ momentum state. This Bragg pulse will couple two

momentum states through the following interaction matrix [26, 85, 108]

$$\hat{\boldsymbol{U}}_{\text{Bragg}} = \begin{bmatrix} \cos\left((\Omega_B\tau_T)/2\right) & -ie^{i\gamma_B}\sin\left((\Omega_B\tau_T)/2\right) \\ -ie^{-i\gamma_B}\sin\left((\Omega_B\tau_T)/2\right) & \cos\left((\Omega_B\tau_T)/2\right) \end{bmatrix}, \tag{2.2.66}$$

where Ω_B is the Rabi frequency, τ_T is the pulse length set to Talbot time, and γ_B is the off set phase of the applied standing wave. To obtain an equal superposition of external states we set the phase $\gamma_B = \pi/2$ and adjust the intensity of the beam via trial and error until the Rabi frequency becomes such that the product in Eq. 2.2.66 $\Omega_B\tau_T = \pi/2$. After the Bragg pulse is applied, AOKR pulses are then applied giving a shift in momentum with each kick and is given by [87, 85, 108, 101]

$$\langle\Delta\hat{p}\rangle = -\frac{\phi_d}{2}\sin(\phi)j. \tag{2.2.67}$$

Eq. 2.2.67 shows that the maximum linear shift in momentum space is obtained if we set $\phi_d \approx 2.0$ and phase to $\phi = \pi/2$.

2.2.4 General Properties of the Quantum Walk

In the following discussions the states $|g\rangle$ and $|e\rangle$ will be referred to as $|1\rangle$ and $|2\rangle$ respectively. A QW in our experiments is realized by first preparing the BEC into the initial state $|\psi_0\rangle = \left(|n=0\rangle + e^{-i\pi/2}|n=1\rangle\right)$ using a Bragg pulse, and then a $\pi/2$ MW pulse is applied with a phase of $\chi = \pi$ as defined by Eq. 2.2.42. This process is known as the Hadamard gate and gives an equal superposition of the initial states [26]

$$\hat{\boldsymbol{M}}(\pi/2, \pi)|e\rangle = \frac{1}{\sqrt{2}}(|1\rangle + |2\rangle). \tag{2.2.68}$$

After this the first kick pulse is applied before the first coin pulse is applied $\hat{\boldsymbol{M}}(\pi/2, -\pi/2)$. Afterwards this process of kick followed by a coin is repeated up to t steps. Note also that this choice of coin and gate operators results in a symmetric walk although it isn't the

only possible choice and as will be seen later could be interchanged to reduce an artifact of remnant atoms that don't participate in the QW due to the light shift effects of the kicking beams. Throughout our experiments studying the effects of SE on the QW we have used the standard walk sequence as first realized in [26] and we will follow that discussion here. If we want to create a QW with t steps it is necessary to use the series of kick and MW operators as defined earlier to create a single unitary operator to describe a single step of the QW and this is denoted as $\hat{\boldsymbol{U}}_{\text{step}}$. A series of these operators after t steps is then [26, 48]

$$\left(\hat{\boldsymbol{U}}_{\text{step}}\right)^{t} = \left[\hat{\boldsymbol{T}}\hat{\boldsymbol{M}}(\pi/2, -\pi/2)\right]^{t-1}\left[\hat{\boldsymbol{T}}\hat{\boldsymbol{M}}(\pi/2, \pi)\right], \tag{2.2.69}$$

where $\hat{\boldsymbol{T}}$, $\hat{\boldsymbol{M}}(\pi/2, -\pi/2)$, and $\hat{\boldsymbol{M}}(\pi/2, \pi)$ are the shift operator realized by the AOKR, Coin, and Hadamard Gate MW operators respectively. The shift operator is defined as [26, 48]

$$\hat{\boldsymbol{T}} = \begin{bmatrix} e^{-i\phi_d\left(1+\cos(\hat{\theta})\right)} & 0 \\ 0 & e^{i\phi_d\left(1+\cos(\hat{\theta})\right)} \end{bmatrix}. \tag{2.2.70}$$

In Eq. 2.2.70 either of the diagonals will apply to one of the internal states of the atoms. It should be noted that the signs of these diagonals are opposite of each other. This is due to the fact that the kicking laser is detuned to a frequency between the internal states and is thus opposite in sign to these states. Also note that the constant terms create an additional phase due to the AC stark shift and letting $\phi_d = k$ it applies to either state as $\phi_1 = -k$ and $\phi_2 = k$ and this creates a phase difference [26, 48]

$$\Delta\phi = \phi_2 - \phi_1. \tag{2.2.71}$$

This extra phase creates an additional phase that acts on the QW and increases with each additional application of the shift operator and had to be countered with a compensating phase added to the microwave coin pulses at each step of the walk. This modifies the coin

pulse to be [26, 48]

$$\hat{\boldsymbol{M}}(\pi/2, \frac{\pi}{2} + 2k) = \frac{1}{\sqrt{2}} \begin{bmatrix} 1 & ie^{-2ik} \\ -ie^{2ik} & 1 \end{bmatrix}. \tag{2.2.72}$$

As we can see this additional phase term will cancel out the phase term due to the shift operator. Moreover this shift operator takes on the form after compensation [26, 48]

$$\hat{\boldsymbol{T}} = \begin{bmatrix} e^{-ik\cos(\hat{\theta})} & 0 \\ 0 & e^{ik\cos(\hat{\theta})} \end{bmatrix}. \tag{2.2.73}$$

If this operator is applied with the ratchet configuration which shifts the momentum state by $\pm q$ then becomes [26, 48]

$$\hat{\boldsymbol{T}} = \begin{bmatrix} e^{iq\hat{\theta}} & 0 \\ 0 & e^{-iq\hat{\theta}} \end{bmatrix}. \tag{2.2.74}$$

For the standard walk $q = 1$ and the shift operator can lastly be written as [26, 48]

$$\hat{\boldsymbol{T}} = \begin{bmatrix} |n+1\rangle\langle n| & 0 \\ 0 & |n-1\rangle\langle n| \end{bmatrix}. \tag{2.2.75}$$

This operator has the effect of shifting the system by ± 1 in momentum space when it is applied to a system with internal states $|1\rangle$ and $|2\rangle$. A schematic of the entire standard QW is shown in Fig. 4 [24] (The SE pulses in panel (a) will be discussed in the following section.). Further properties of the QW such as reversal will not be discussed here as this was not of interest in our experiments.

2.3 Spontaneous Emission Theory

In this section we describe the effects of spontaneous emission (SE) by using the imaging light as a readily tuneable source to intentionally induce SE events during the QW. It is important to note that an external source of light such as the imaging beam causes SE events through

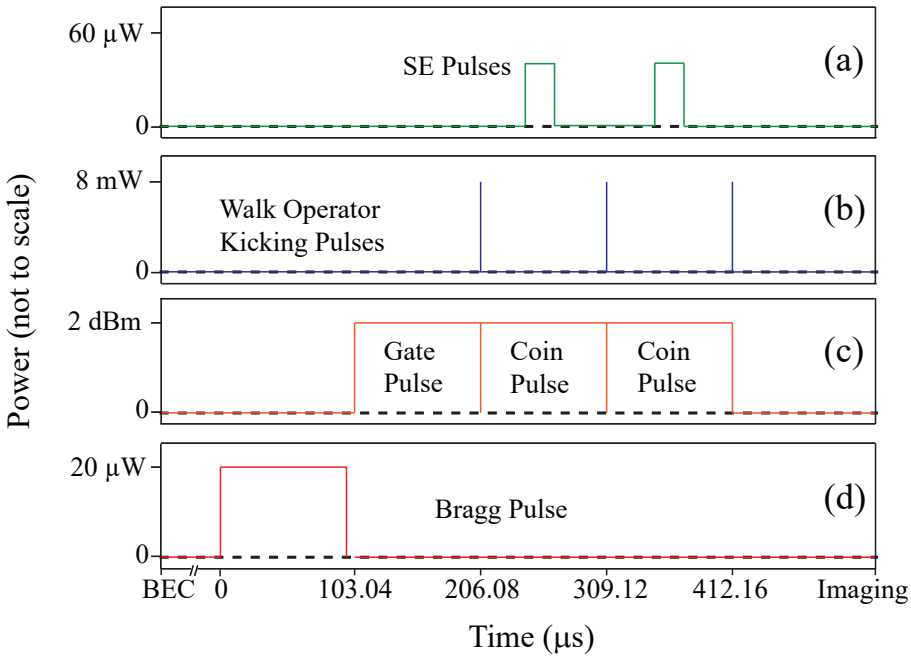

Figure 4: Schematic diagram of the kicking and microwave pulses used in the QW. Also shown are the SE pulses used to induce SE during the QW. Adapted from [24].

a different mechanism compared to the SE from the kicking beams themselves as we will discuss.

2.3.1 Basics of Spontaneous Emission

It is well known that an atom in an excited state has a probability that the excited electron will spontaneously emit a photon and decay back to its ground state. This is known as spontaneous emission and in the QW it has the effect of causing decoherence and thus destroying the quantum walk leading to classical behavior where the momentum distribution approaches a Gaussian as seen in the classical walk. A simple classical model to introduce SE is presented here which also leads to the well known Einstein coefficients and is adapted from [42][4]. If we consider an electric dipole moment $-eD$ with an oscillation of ω this dipole will emit radiation with a power of [42, 4]

$$P = \frac{(eD\omega^2)^2}{12\pi\epsilon_0 c^3}. \tag{2.3.1}$$

Because this electron is in harmonic motion it has a total energy of $E = {}^{(m_e\omega^2 D^2)}/_2$ where D is the amplitude of the motion, ω is the frequency of oscillations and m_e is the rest mass of the electron. This energy decreases with a rate of [42, 4]

$$\frac{dE}{dt} = -\frac{e^2\omega^2}{6\pi\epsilon_0 m_e c^3}E = -\frac{E}{\tau}, \tag{2.3.2}$$

where the fraction term was set to [42, 4]

$$\tau^{-1} = \frac{e^2\omega^2}{6\pi\epsilon_0 m_e c^3}. \tag{2.3.3}$$

Eq. 2.3.3 is known as the classical radiative lifetime and varies over a wide range depending on the atom under consideration.

2.3.2 Spontaneous Emission Applied to Quantum Walk

In our quantum walk SE occurs in each experiment and to realize a high quality QW or other good experiment one will wish to keep their effects to a minimum. In the standard walk a primary source of induced spontaneous emission are due to the applied AOKR pulses used for the shifting operator. SE in the AOKR has been known for some time [5] and its effects have been observed in numerous experiments. In our quantum walks the SE from the AOKR was theoretically analyzed in [50] by considering a closed three level system and describing the SE dynamics by a Lindbladian dissipator that acts on an atomic density operator. These Lindblad operators included the spontaneous emission rate with the projection operator from the ground and excited states [50]

$$L_m = \sqrt{\gamma_m}|g\rangle\langle e|, \tag{2.3.4}$$

with the SE rate defined in terms of our experiment as [50]

$$\gamma_m = \frac{k_m}{\tau_p \tau_{SE} \Delta_m}. \tag{2.3.5}$$

From this the total decay rates from both AOKR beams is then $\gamma = \gamma_1 + \gamma_2$ and this then gives the spontaneous emission for each kick as [50]

$$p = \gamma \tau_p. \tag{2.3.6}$$

When a spontaneous emission event occurs an atom in an excited state $|e\rangle$ will collapse into one of the two ground states. Although this analysis was done with the AOKR beams in mind and an experimental procedure was attempted with this mind, although it was not successful in inducing very noticeable SE effects it did lead the way to introducing the idea of using the imaging light as will be discussed.

2.3.3 Spontaneous Emission using imaging light

As was mentioned before using the AOKR to increase the rate did not have much effect on the distribution of the QW. As a result the imaging light which is on resonance with the $|F = 2\rangle$ to $|F' = 3\rangle$ hyperfine levels of ^{87}Rb and is normally used to take images of the atoms after an experiment is applied as a tunable SE source. Applying this light during the coin pulses of the QW to avoid interfering with the shift operator causes the atom to decay due to the selection rules to the state $|F = 2\rangle$ and this thus corresponds to a projection of the atom onto the $|F = 2\rangle$ state. The laser coupling is defined as [24]

$$\Omega_{\mathrm{C}} = \gamma \sqrt{\frac{I}{2I_s}}, \tag{2.3.7}$$

where I is the intensity of the laser, I_s is the saturation intensity, and γ is the decay rate. This laser coupling is assumed to be small when compared to the excited state hyperfine splitting

between the $|F'=3\rangle$ and $|F'=2\rangle$ levels so it can be assumed that the $|F=2\rangle \rightarrow |F'=2\rangle$ transition is far too detuned to create a significant population in $|F'=2\rangle$. Because the SE pulse is long enough we can assume that the atom will reach the steady-state, *i.e*, the coin pulse should not interfere with this process, meaning that the effective SE rate γ_{eff} is given by the natural line width times the steady-state population of $|F'=3\rangle$ as follows [115]

$$\gamma_{\text{eff}} = \frac{\gamma}{2}\frac{I/I_s}{1+I/I_s}. \tag{2.3.8}$$

Eq. 2.3.8 can then be used to give us a modified SE rate similar to Eq. 2.3.6 with the imaging laser in mind [24]

$$\rho = \gamma_{\text{eff}} t_{\text{SE}}. \tag{2.3.9}$$

Because after the atom decays close to an equal superposition of the two ground states the probability of the first and later decay events have to be scaled by a factor of 2. Thus technically γ_{eff} and ρ will change during a single trajectory. Thus the rate represented by Eq. 2.3.9 is an upper limit and is only good for a couple of microseconds after a SE event. In our experiments we estimate that the SE rate for an applied SE power of 3 μW to be $\rho \approx 0.35$ as described in chapter 4. Because the SE light is applied at 30 μs after the start of a coin pulse, SE events will interrupt the coin at random times and thus the coin will only have a partial action in between two events of time delay t given by [24]

$$e^{i\frac{\pi t}{4T}\hat{\sigma}_x} = \begin{bmatrix} \cos(\frac{\pi t}{4T}) & i\sin(\frac{\pi t}{4T}) \\ i\sin(\frac{\pi t}{4T}) & \cos(\frac{\pi t}{4T}) \end{bmatrix}, \tag{2.3.10}$$

where T is the total length of the coin pulse. As a result, the state $|\psi\rangle$ of the internal degree of freedom after a coin sequence is dependent only upon the time of the last SE event, $t' \in [0.29, 0.58] \times T$ and thus given by [24]

$$|\psi_{\text{int}}\rangle = \cos\left(\frac{\pi(T-t')}{4T}\right)|2\rangle + i\sin\left(\frac{\pi(T-t')}{4T}\right)|1\rangle. \tag{2.3.11}$$

Here $|1\rangle$ and $|2\rangle$ represent the two internal states, $|F = 1, m_F = 0\rangle$ and $|F = 2, m_F = 0\rangle$, respectively. From Eq. (2.3.11) we can clearly see that an SE pulse will create an imbalance in the internal state of the atoms towards $|2\rangle$. This imbalance then gets transferred to the atom population and results in an overall biased momentum distribution as shown in theoretical calculations in Fig. 5 [24]. The initial external states in momentum space are

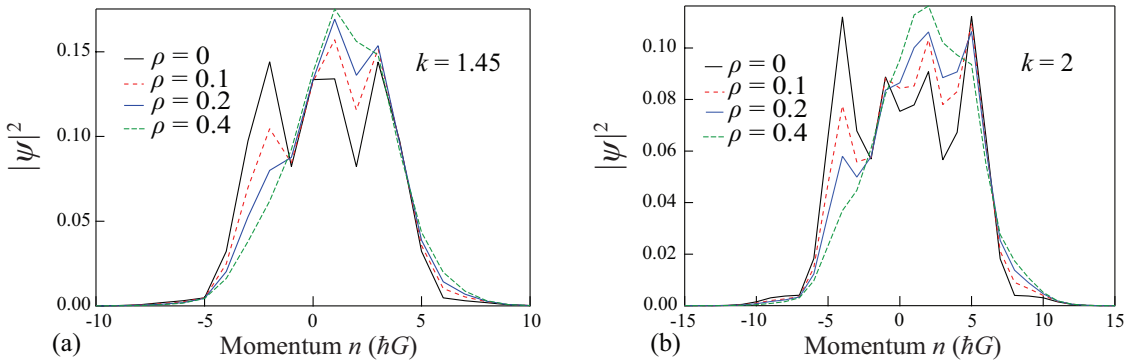

Figure 5: Simulated momentum distributions of five-step quantum walks at two kicking strengths, $k = 1.45$ (a) and $k = 2.0$ (b), averaged over 10^3 trajectories with $\Delta_\beta = 0.025\ \hbar G_0$ at various SE probability ρ. Here Δ_β is the width of the quasimomentum β. Note the increasing asymmetry as the probability ρ increases. Adapted from [24].

given by [24]

$$|\psi_{\text{ext}}\rangle = 1/\sqrt{2}(|n = 0\rangle + e^{i\phi}|n = 1\rangle). \tag{2.3.12}$$

The external degree of freedom is also affected by the SE event and thus causes a shift in quasimomentum by random amounts. Because the SE beam is perpendicular to the axis of the walk the induced SE effect differs from the SE caused by the kicking beams [50] (briefly discussed in Subsec. 3.3.2.), the atom does not incur any recoil from the absorption of a photon from the SE beam. It should be noted that the effects of SE not only cause phase scrambling due to its affects on both the internal and external states or projection onto the hyperfine levels, it also shifts the quasimomentum. Possible heating during the experiment is taken into account during these simulations by considering an initial distribution of the quasimomentum, Δ_β. In the simulations possible recoil from emission itself were taken into account. In this model the possible effects of stimulated emission were also considered along

with absorption. When a kick is applied the atom gets excited from the kicking laser by absorption of the light. When the atom is in the excited state it can interact further with photons either from the AOKR beams or the applied imaging beam with energy $\pm\hbar k$ to return to the ground state resulting in stimulated emission.

2.4 Effects of AC Stark shift on QW due to AOKR light

In this section we will discuss the effects of the AC Stark shift on the QW due to the kicking lasers used to realize the shift operator. As was noted in the discussion of the standard walk the AOKR pulses induce a phase shift that is applied to the atoms as the states of the walker evolve with each step and this was compensated by adding a countering phase to the coin operator. However, even when this compensating phase was found at a particular step $\hat{\boldsymbol{U}}_{\text{step}}$ it could not be used universally throughout the rest of the walk for the desired steps. As a result one has to apply fine tuning of the phase to maintain the proper distribution. However, if we introduce the AC Stark shift into our theory of the QW with the AOKR we are able to arrive at a more complete description. We will first briefly outline the AC Stark shift before describing how it affects the QW.

2.4.1 AC Stark shift or Light Shift

The Stark shift was first discovered in the Balmer series of hydrogen in 1913 by J. Stark [114] and is termed a DC shift due to the electric field being constant. The AC Stark shift wasn't discovered until 1969 [32, 16] after the development of lasers to realize the varying electric fields. Before describing the AC Stark shift we present a quick review of the DC Stark shift first. If we consider an atom in a static electric field $\boldsymbol{\mathcal{E}}$ the electric field will induce a dipole $\boldsymbol{p} = \alpha\boldsymbol{\mathcal{E}}$ where α is the polarizability and cause a shift in energy [43]

$$E = -\boldsymbol{p} \cdot \boldsymbol{\mathcal{E}}. \tag{2.4.1}$$

If the electric field is turned on starting from zero then the change in energy is quadratic and shifted towards smaller frequencies although with a small magnitude. Applying perturbation theory then the change in energy of an i^{th} state is [43]

$$\Delta E_i = \sum_{i \neq i} \frac{|\langle \psi_i | H_I | \psi_j \rangle|^2}{E_i - E_j}. \tag{2.4.2}$$

The effects of this shift on an energy diagram of a two level system [42] are shown in Fig.6. Now let's consider the effects of a varying electric field that gives rise to an A.C. Stark shift.

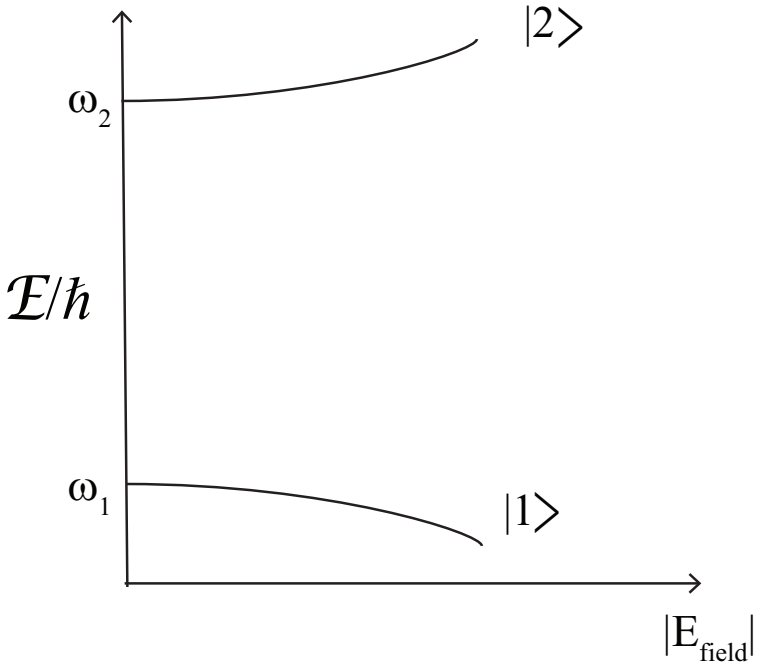

Figure 6: Frequency shift of the energy states of a two-level system due to the Stark-shift as the magnitude of the applied electric field increases from zero.

If we return to the optical Bloch equations and write them in the form [42]

$$i\frac{d}{dt}\begin{bmatrix} c_1 \\ c_2 \end{bmatrix} = \begin{bmatrix} \delta/2 & \Omega/2 \\ \Omega/2 & -\delta/2 \end{bmatrix} \begin{bmatrix} c_1 \\ c_2 \end{bmatrix}, \tag{2.4.3}$$

where Ω is the again the Rabi frequency, c_1 and c_2 are the energy levels of the two level system, $\bar{c}_1 = e^{-i(\delta t/2)}$, $\bar{c}_2 = e^{i(\delta t/2)}$ and $\delta = \omega - \omega_0$ is the detuning of the frequency between

the energy levels of the two level system. Solving Eq. 2.4.3 yields [42]

$$\begin{bmatrix} c_1 \\ c_2 \end{bmatrix} = \begin{bmatrix} a \\ b \end{bmatrix} e^{-i\lambda t}, \tag{2.4.4}$$

where λ are the eigenvalues [42],

$$\lambda = \pm \frac{\sqrt{\delta^2 + \Omega^2}}{2}. \tag{2.4.5}$$

In most cases, including that of the AOKR, a light shift is more important where the frequency detuning is large and off resonance. As a result, Eq. 2.4.5 approximates to [42]

$$\lambda \approx \pm \left(\frac{\delta}{2} + \frac{\Omega^2}{4\delta} \right). \tag{2.4.6}$$

This tells us that the states are shifted from the unperturbed positions, *i.e.* $\lambda = \pm\delta/2$, when the electric field is zero corresponding to $\Omega = 0$. From this the light shift of the state associated with $\bar{c}_1$ is [42]

$$\Delta\omega_{\text{shift}} = \frac{\Omega^2}{4\delta}. \tag{2.4.7}$$

The effects of such a shift on the energy levels of a two level system is shown in Fig. 7 [42]. Next we will discuss how this affects the QW and how it is possible to reduce these effects.

2.4.2 Effects of light shift on the QW

When we analyze the TOF images of the QW with or without SE we notice the presence of a central region of atoms in the images that don't appear to respond to any of the microwave pulses as they are used in the sequence defined in Eq. 2.2.69. The original explanation [27] was that these atoms were a part of a residual thermal cloud of atoms that possesses a higher amount of energy and were distributed uniformly over the quasimomentum β. Because of this, it was thought that these atoms simply did not participate in the walk and thus moved very little from step to step of the walk. The origin of light-shift is from the AOKR beams

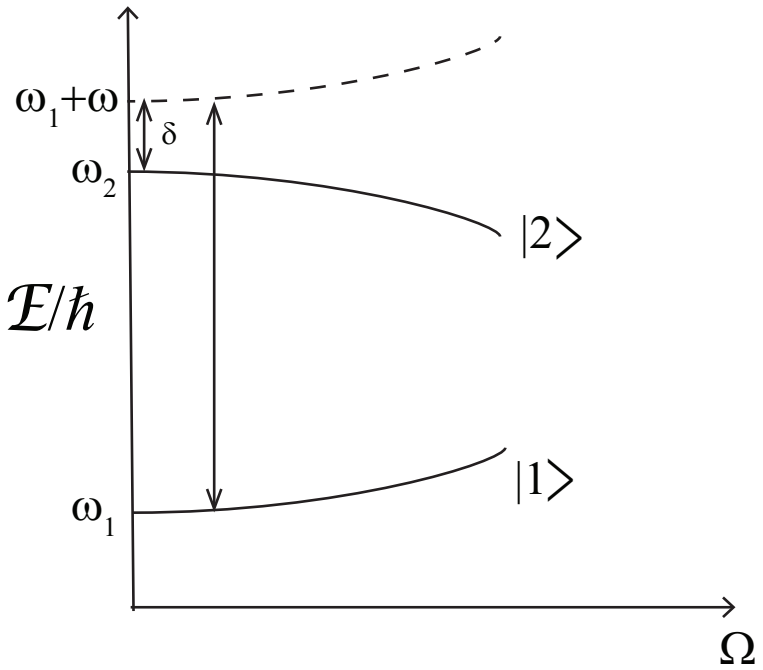

Figure 7: Diagram of eigenenergies of a two level system with AC Stark-shift versus Rabi frequency.

during a kick in the experiment. The interaction between the ground and excited states is [14]

$$\hat{H}_{int} = \frac{\Omega}{2}|g\rangle\langle e|\cos\left(\frac{\theta}{2}\right)e^{i\delta t} + h.c. \tag{2.4.8}$$

The effective dynamics after adiabatically eliminating the excited state are then described by the AC Stark shift of the ground state from the applied kicking laser [14]

$$\hat{H}_{int} = \frac{\Omega}{8\delta}|g\rangle\langle g|\cos\left(\hat{\theta}+1\right). \tag{2.4.9}$$

This adiabatic approximation is valid because the excited state has a very short lifetime and thus it can be assumed that this state is unpopulated on average and thus two ground states remain each with an AC Stark shift. After applying the rotating wave approximation we then have [14]

$$\hat{H}_{int} = \frac{\Omega}{8\delta}\hat{\sigma}_z\cos\left(\hat{\theta}+1\right). \tag{2.4.10}$$

From Eq. 2.4.10 we can see that we now have an additional energy difference that cannot be neglected. It is this energy difference that gives rise to the AC Stark shift. When the effects of light-shift are considered as outlined above we can integrate into the kick operator as [14]

$$\hat{U}_{\text{kick,shift}} = e^{-i\sigma_z \phi_d (1+cos(\hat{\theta}))}. \tag{2.4.11}$$

This gives us the previously mentioned phase shift of $2\phi_d$ that arises with each applied kick operator. Previous mitigation was done by using a counter phase and applying to the coin. However, we could exchange the coin and gate pulses in Eq. 2.2.69 giving rise to a new sequence

$$\left(\hat{\boldsymbol{U}}_{\text{step}}\right)^t = \left[\hat{\boldsymbol{T}}\hat{\boldsymbol{M}}(\pi/2, \pi)\right]^{t-1} \left[\hat{\boldsymbol{T}}\hat{\boldsymbol{M}}(\pi/2, -\pi/2)\right]. \tag{2.4.12}$$

If we incorporate the effects of the light shift into the operator by applying the light shift part of the kicking operator we have

$$\hat{\boldsymbol{M}}(\pi/2, \chi)e^{\phi_d \sigma_z} = \frac{e^{-i\phi_d}}{\sqrt{2}} \begin{bmatrix} 1 & e^{-i(\chi-2\phi_d)} \\ -e^{i\chi} & e^{i2\phi_d} \end{bmatrix}. \tag{2.4.13}$$

From this we can see that the phase compensation using χ as was done in previous experiments could not completely eliminate the light-shift effect. However, exchanging the coin and gate operators as mentioned above are more able to achieve this due to the phase being set to $\chi = \pi = 2\phi_d$. The effects of light shift can be further reduced by increasing the number of initial states. This is because increasing the number of states causes, as mentioned above in discussions around the translation operator especially Eq. 2.2.64, a more refined ratchet which in turn leads to a cleaner walk in combination with exchanging microwave operators.

CHAPTER III

EXPERIMENTAL SETUP

In this chapter we outline the experimental setup and procedures that was used during the research projects. Historically, ^{87}Rb was the first atom to be used to realize a BEC due to its relative ease of use in creating a BEC compared with other isotopes of Rubidium and with other atoms. It was also chosen because the physical properties of ^{87}Rb make it ideal to realize the Atom-Optics kicked rotor (AOKR) in our experiments. Our setup consists of two main optical tables, the "MOT table" and the "Chamber table".

3.1 MOT table

To create a BEC we have to dramatically slow the Rubidium atoms down to achieve the necessary phase space density and critical temperature. One of the steps to this goal is the use of a Magnetic-Optical Trap (MOT). In order to create a MOT one needs to use two main frequency locked lasers at 780 nm for ^{87}Rb. One laser was used to perform the cooling, optical molasses, and imaging procedures of the experiment while the second was used for repump to maintain the MOT. For both lasers a standard laser spectroscopy technique utilizing ^{87}Rb vapor test cells was used to monitor the spectroscopy signal. A detailed schematic for the MOT table is shown in Fig. 9 (Adapted from [26, 108]). The full spectrum signal of the hyperfine levels is shown in Fig. 8(Adapted from [26, 108]). Both of these lasers were TOPTICA DL 100 temperature and grating stabilized diode lasers with a power output of $\approx 30mW$. One of the lasers was frequency locked to between the $5^2S_{\frac{1}{2}}, F = 2$ ground state and the $5^2P_{\frac{3}{2}}, F' = 2$ to $F' = 3$ crossover line in the hyper fine structure of ^{87}Rb. This

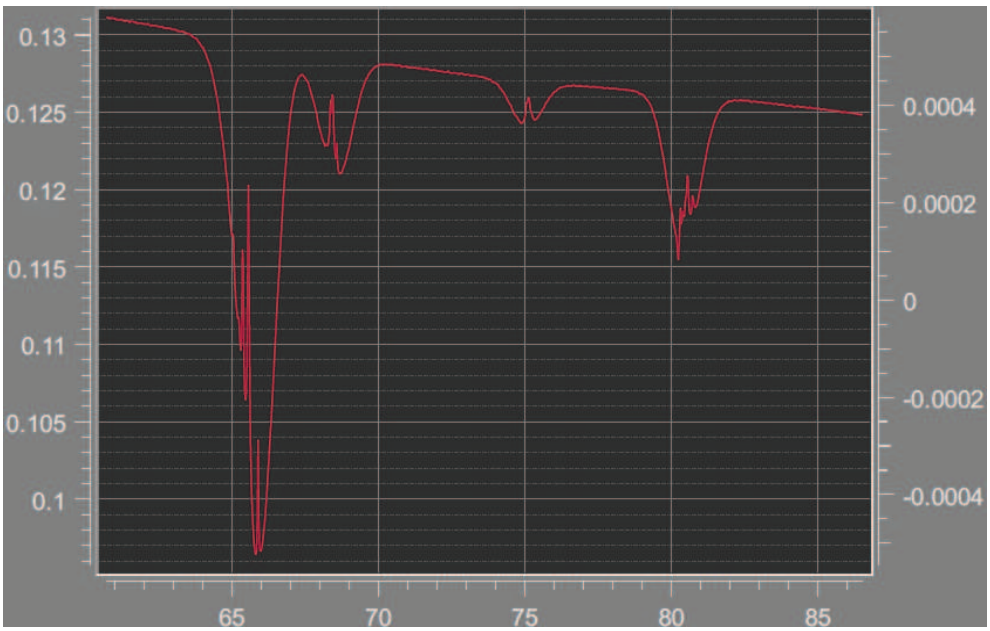

Figure 8: Overall laser spectroscopy signal from a DL 100 frequency locked laser. Both the repump and MOT signals can be seen here.

transition is shown in the line diagram in Fig. 10. The location of this frequency locking is shown in Fig. 11(Adapted from [26, 108]). As mentioned above the laser used for the MOT generation was a TOPTICA DL 100 operating in continuous-wave mode. This laser used a diode laser that has an elliptical beam shape that had to be made circular using a pair of anamorphic prisms immediately placed after the aperture of the laser. These prisms were then followed by a $\lambda/2$ wave-plate to ensure that all of the laser light passes through a polarizing beam splitter with a rotation axis 45° to vertical. To make sure that no light was back reflected into the laser which makes frequency locking impossible a Faraday rotator or optical isolator was placed after the wave-plate. This isolator rotates the polarization from 45° which makes it horizontally polarized and isolating the MOT laser from interference. To perform the absorption spectroscopy necessary for frequency locking a small amount of light from the MOT laser was sent to a spectroscopy setup with a ^{87}Rb vapor cell.

Because the overall output power of the MOT laser was very low it was insufficient to directly create the MOT, with most of the power loss due to the required double pass AOM. As a result, it was necessary to amplify the output power by the use of extra 780nm laser

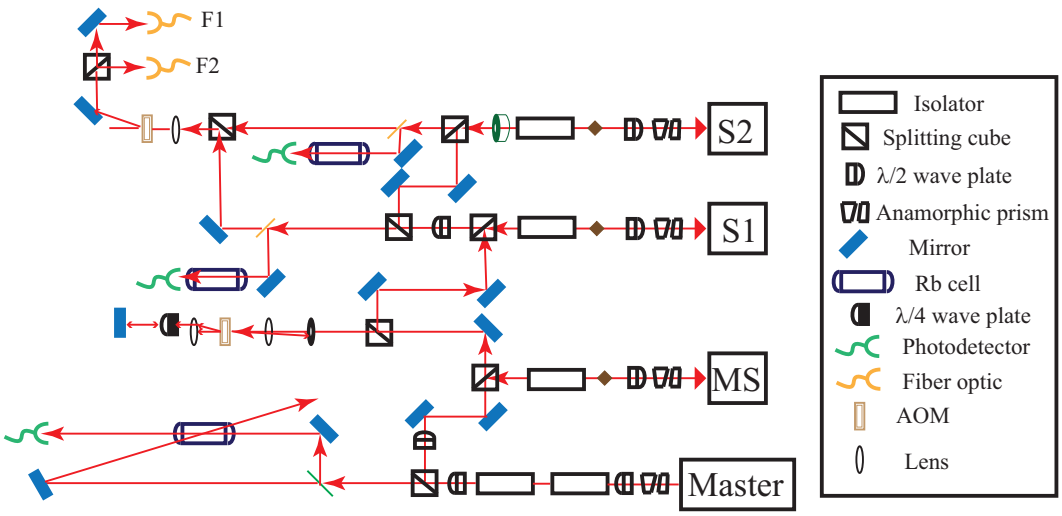

Figure 9: Schematic of the laser table optical setup. Both fibers 1 and 2 send laser light to the chamber table. Although not shown in this figure the repump laser is on the same optical table as this setup.

diodes as amplifiers. These "slave" lasers used the principle of injection locking [112] to ramp up the overall power from an input of $\approx 10mW$ to an output of $\approx 100mW$. Three such lasers were used with this method and for each a small amount of light ($\approx 100\mu W$) was passed through a ^{87}Rb cell to monitor their signals via photodiodes (Thorlabs; DET-210, PDA-400, PDA-36A2, or homemade FDS010, and FDS100) to ensure that these lasers were properly following the main laser spectroscopy signal. If proper injection locking was achieved one can observe the "slave" lasers "following" the absorption profile of the MOT laser on an oscilloscope.

To create a good BEC with high signal-to-noise ratio it was crucial to have a precise control of the laser frequency. Four different frequencies were required to realize MOT creation, optical molasses or Doppler cooling, imaging, and repumping. Each of these frequencies were [26, 108]:

1. -15 MHz detuning from $5^2S_{1/2}, F = 2 \rightarrow 5^2P_{3/2}, F' = 3$ transition for MOT creation.

2. -80 MHz detuning from $5^2S_{1/2}, F = 2 \rightarrow 5^2P_{3/2}, F' = 3$ transition for the Doppler cooling.

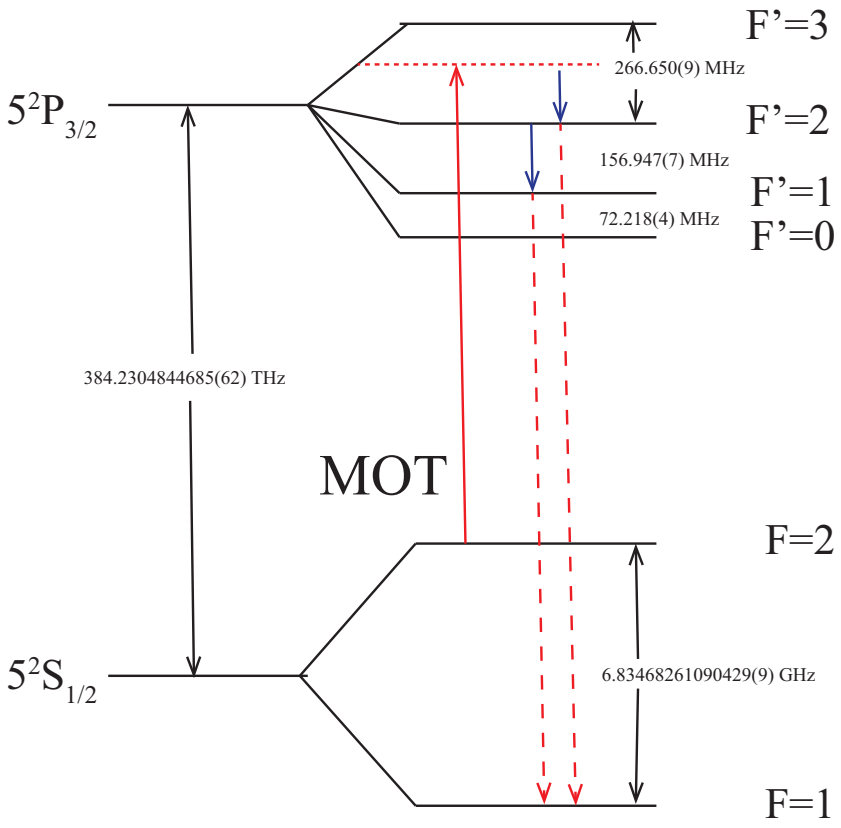

Figure 10: ^{87}Rb line diagram showing the MOT transition frequency along with the possible decay transitions (blue arrows) due to power broadening which had to be addressed by the repump laser. Frequency values for the transitions are also labeled (black arrow) [115]

3. On resonance with the $5^2S_{1/2}, F = 2 \rightarrow 5^2P_{3/2}, F' = 3$ transition for imaging.

4. On resonance with the $5^2S_{1/2}, F = 1 \rightarrow 5^2P_{3/2}, F' = 2$ transition for repumping (This was a separate DL 100 laser).

The first three conditions were achieved by using many acousto-optic modulators (AOM) that were controlled by a LabView computer program. The MOT laser itself was frequency locked at 133.3 MHz below the MOT transition. Light from this laser was then injection locked with a "master slave" laser which was then sent to double pass AOM setup to give better control over detuning to realize the first three frequencies listed above [26, 85]. Taking the first order of light after a pass of the AOM in this setup gave a frequency of $f = f_0 + 2f_{AOM}$ where f_0 is the incoming "master slave" laser frequency. After the double pass setup this light was then sent to two other laser labeled "slave-1" and "slave-2" respectively using the

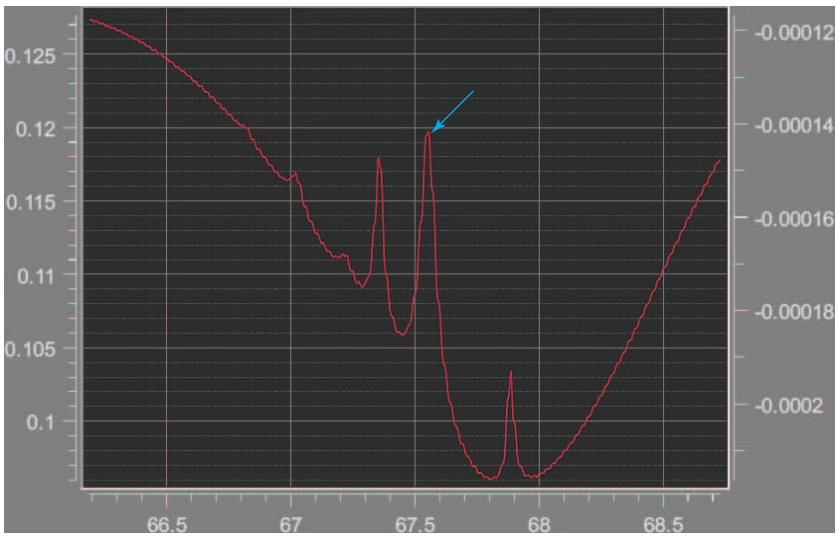

Figure 11: Laser spectroscopy signal of ^{87}Rb showing the hyperfine structure where the DL 100 laser was frequency locked as indicated by the blue arrow for MOT creation.

same injection locking technique described above. The chief advantage of using a double pass AOM setup is that this greatly reduces the deflection of the beam that occurs in a single pass of the AOM at different frequencies [36]. To further reduce deflection a telescopic configuration of two lenses was used to make sure that the retro-reflected first order light after the first pass was co-propagting with the incoming light.

The laser light from both "slave-1" and "slave-2" were sent through another AOM(ISOMET 1205C-1) driven at a frequency of 80 MHz. After the AOM the negative first order beam ($f' = f - 80$ MHz) was split into two beams which were then sent to the chamber table by two polarization-preserving single-mode fibers that are referred hereafter as fiber-1 and fiber-2. The coupling efficiency of such fibers is very dependent upon the shape and size of the incoming beam. As a result, to maximize this efficiency two lenses in a telescope configuration was setup prior to the fibers. To calculate the final detuning values for the transition we use Eq. 3.1.1 [108]

$$\delta = -133.3 \text{ MHz} + 2f_{\text{AOM}} - 80 \text{ MHz}. \tag{3.1.1}$$

From this equation we found that to achieve the required 99.5, 66.5, and 106.65 MHz to

realize the MOT, Doppler cooling, and imaging the AOM frequencies had to be set to -15, -78, and 0 MHz respectively. It is very important to note that these values often have to be slightly changed based on the day-to-day conditions inherit in the experiment and thus these values should be taken as approximations in practice.

A separate TOPTICA DL 100 laser was required to create a repump beam. This repump mechanism is required because of the power broadening in the MOT beam in which there is a probability that atoms excited to the $5^2P_{3/2}, F' = 3$ state will decay down to the $5^2P_{3/2}, F' = 2$ and $F' = 1$ levels. The electron will then decay down to the $5^2S_{1/2}, F = 1$ energy level and thus the MOT would quickly disappear without further intervention. To counter this the repump laser was frequency locked on the transition from the $5^2S_{1/2}, F = 1$ ground state to the $5^2P_{3/2}, F' = 2$ excited state. The location of this frequency on the ^{87}Rb line diagram is shown in Fig. 12 (Adapted from [26, 108]). This enables us to efficiently maintain a stable MOT to create a BEC. The absorption spectrum profile of this transition along with the peak that was frequency locked is shown in Fig. 13 The repump laser had a similar alignment to the MOT laser and a schematic of this optical setup is shown in Fig. 14 (Adapted from [26, 108]). This laser was also sent through a double pass AOM setup using an ISOMET 1205C-2 AOM after which the positive first order was coupled with fiber-2 to be sent to the chamber table along with the MOT beam.

3.2 Chamber table

The chamber table contains the vacuum chamber whereupon the BEC is created and experiments are conducted, the CO_2 laser system to realize the dipole trap, the kicking laser setup, the microwave setup, and the imaging system. It is also important to note that the imaging setup also served as the external light source to realize spontaneous emission. All of the laser beams from the aforementioned MOT table are sent into the vacuum chamber after exiting fiber-1 and fiber-2. The vacuum chamber also had a system of anti-Helmholtz and nulling magnetic coils. In this section we describe each system in detail.

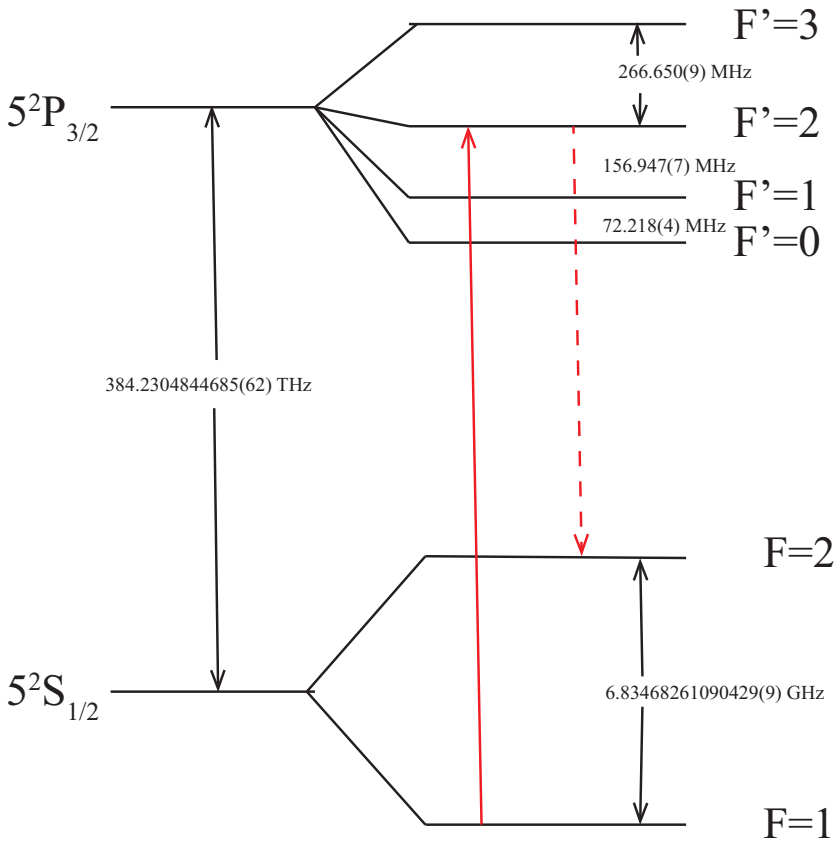

Figure 12: ^{87}Rb line diagram showing the repump transition frequency used to maintain cycling for the MOT (red arrows).

3.2.1 MOT setup

After exiting fiber-1 and fiber-2 the MOT and repump light was delivered to the vacuum chamber via the optics setup as shown in Fig. 15 (Adapted from [26, 108]).

The majority of the light from fiber-1 was used in creating the MOT while a very small portion of it was picked off to be used for the imaging and spontaneous emission. The light from fiber-2, which contained both MOT and repump beams, was first sent to a polarizing splitter to form two separate MOT beams hereafter labeled Beam 2 and Beam 3. All MOT beams and repump beam were expanded to ≈ 1 in. in diameter by using a combination of expanding lenses. This light was then sent through quarter-wave ($\lambda/4$) plates so that the light will be circularly polarized. All three of the expanded MOT beams are then sent into the vacuum chamber and were then retroreflected back into another quarter-wave plate and

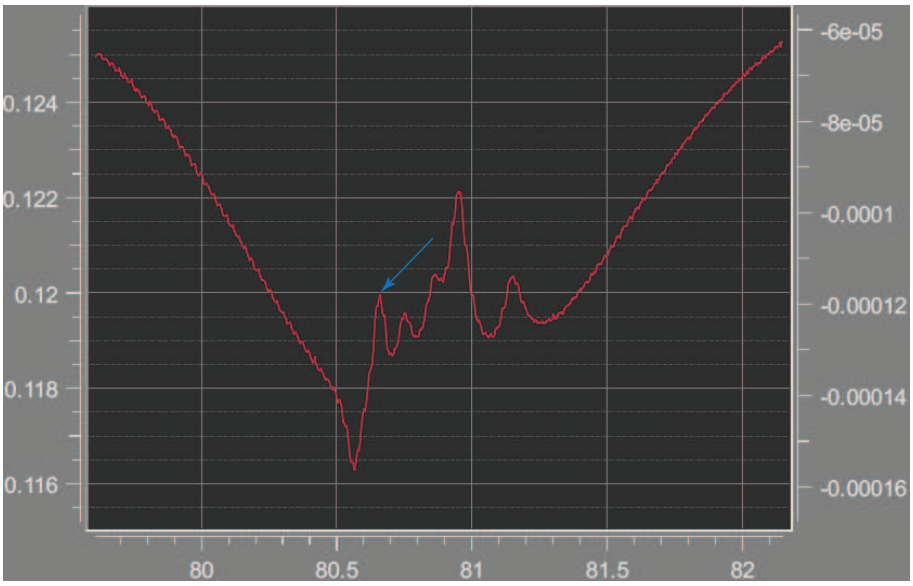

Figure 13: Laser absorption spectroscopy signal ^{87}Rb showing the hyperfine structure where the repump laser was frequency locked as indication by the blue arrow to maintain the MOT.

the chamber after exiting. This extra wave-plate was necessary to ensure that the MOT beams would have the correct $\sigma^+ - \sigma^-$ combinations. Such a setup enables our BEC system to be more compact than a system using six individual counter-propagating MOT beams. All three of the MOT beams were aligned so that each would intersect at the center of the chamber whereupon the MOT itself would appear. During an experimental run, the imaging, MOT, and repump beams were blocked at different times. This process was accomplished by passing each of these beams through fast mechanical shutters (UNIBLITZ, LS2T2) that were controlled by the LabView computer program. It should be noted that to maintain a good and stable MOT it was crucial that the power of the beam after exiting fiber-2 exit the splitting cube with a power ratio near one. This was done in two ways, one was to make sure that the light entering fiber-2 was properly coupled to the fiber with the correct polarization. The other method was by adjusting the half-wave plate after fiber-2 to achieve the proper ratio until a stable MOT was realized.

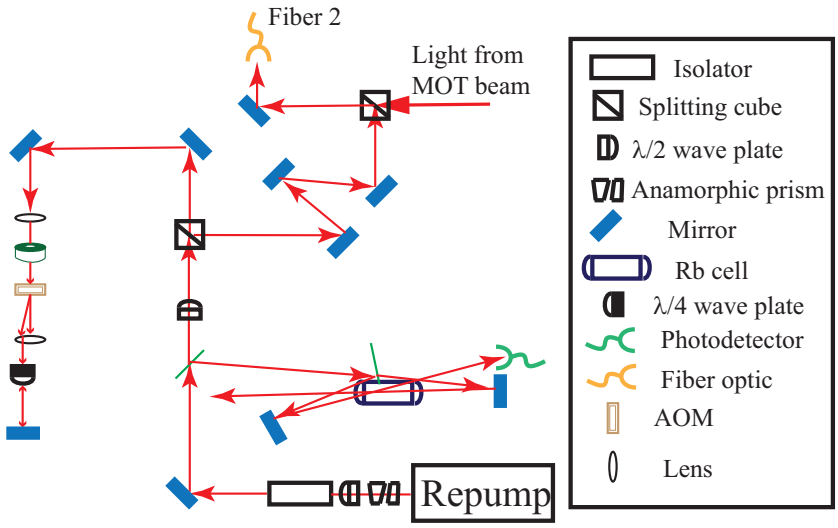

Figure 14: Optical arrangement for the repump laser.

3.2.2 CO_2 Laser System

To realize the dipole trap a high power ($\approx$ 50 W) continuous-wave laser beam with a wavelength of $\approx 10.6\mu$m was used. This laser was far off the resonance of any energy levels of ^{87}Rb and was thus known as the Far-Off-Resonance Trap (FORT). The FORT beam was realized by the use of a COHERENT, GEM Select-50 CO_2 laser powered by an Agilent, 6573A DC power supply. Because the 10.6μm light from this laser has a high absorption coefficient regarding glass and quartz the usual optics that were used for the near infrared MOT lasers could not be used. As a result, the optics for the FORT beam were made from Zinc-Selenide (ZnSe) which had the required lower absorption coefficient. This same material was also use in the viewports of the chamber that accepted the FORT beam.

The schematic of the optical setup for the FORT beam is shown in Fig. 16 (Adapted from [26, 108]).

During the BEC creation procedure it is necessary to have precise control of the power of the FORT beam. This was achieved by the use of a water cooled AOM (IntraAction Corp., AGM 406-B1) that was driven by an IntraAction Modulator Driver Model GE-4030H which was controlled by an analogue voltage signal from the LabView computer program. The first deflected order of the FORT beam ($\approx$ 25 W) was sent to the chamber via a combination of

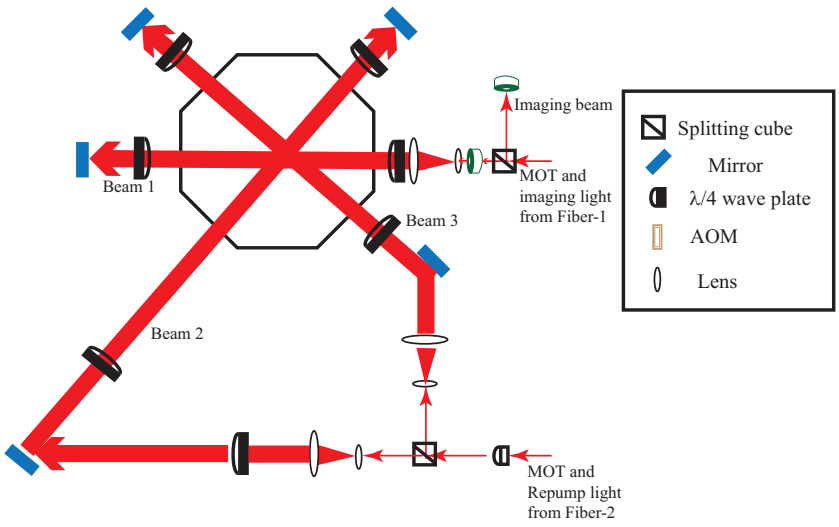

Figure 15: Schematic of MOT beam setup. Adapted from [26]

lenses while the zeroth order was directly sent to a beam dump. The first two lenses in this combination was set up in a telescopic configuration to expand the beam. The third lens was a focusing lens of focal length 1.5in and was installed in the vacuum chamber. The FORT beam was delivered into the chamber through a 1in diameter viewport made from the same ZnSe material used in the FORT optics. The overall spot size of the beam in the center of the chamber is given by $w_0 = \lambda f/(\pi R)$ where R is the beam radius at the third lens and f is the focal length. To achieve the loading and evaporative cooling processes necessary to realize a BEC the waist of the beam (w_0) was either set at a large or small size respectively. To realize this the second lens of the expander was mounted onto a motorized translation stage (Aerotech, 101SMB2-HM) that was controlled by a Soloist driver interface that was in turn controlled by the LabView computer program.

3.2.3 Vacuum Chamber setup

Every experiment using the creation and manipulation of the BEC was conducted inside the vacuum chamber. The vacuum chamber (MDC Vacuum Products) consisted of a stainless steel six-way cross with an octagonal multiport chamber attached. The chamber had four antireflection coated quartz viewports of 2.0 in. in diameter and these were used for the

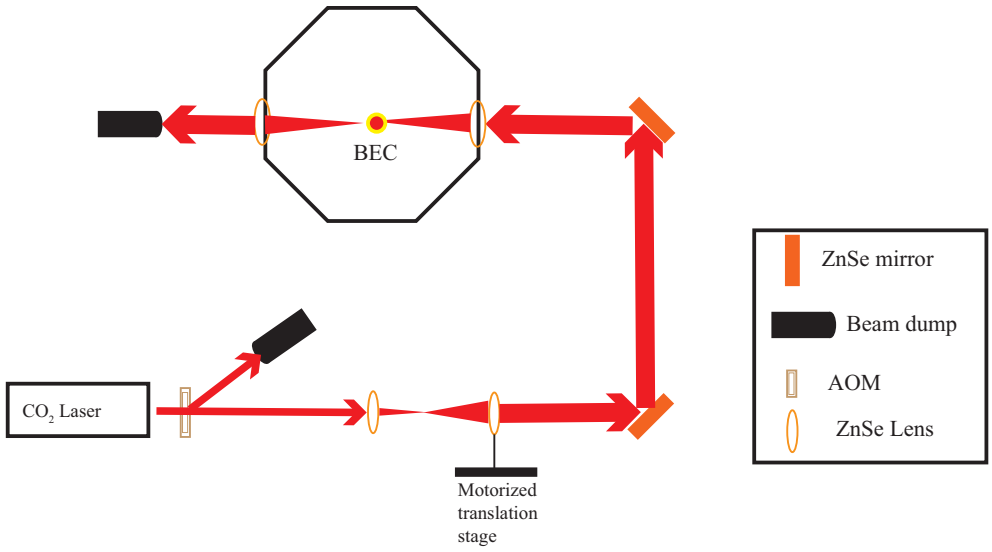

Figure 16: Schematic of the CO_2 laser setup used to realize the FORT to achieve evaporative cooling leading to a BEC.

MOT and kicking beams. There were four 1.0 in. diameter viewports for the FORT beam, and two large 5.0 in. quartz viewports attached to the open side of the six-way cross and the other attached to the octagonal chamber. These large viewports were used for MOT, and imaging/spontaneous emission beams as well as the microwave radiation from a nearby microwave horn antenna. The vacuum system was assembled previously and the chamber was pumped in several phases to achieve a vacuum of $\approx 10^{-10}$ Torr. To maintain this vacuum at all times an automatic Varian style 8 liters ion pump was attached to the chamber and this was powered by a Terrenova-751 controller. The vacuum chamber was itself shielded from the magnetic field generated from the ion pump by using μ-metal sheets attached to the system.

The magnetic field needed for trapping of the atoms in the MOT was generated by a pair of coils setup in an anti-Helmoltz configuration (two coils identical in diameter and windings separated by a distance equal to their radius with currents in opposite directions) and were referred to as the main coils. A schematic of this arrangement is shown in Fig. 17 (Adapted from [26, 108]).

These coils were made from copper tube with a square cross-section of dimensions 0.125

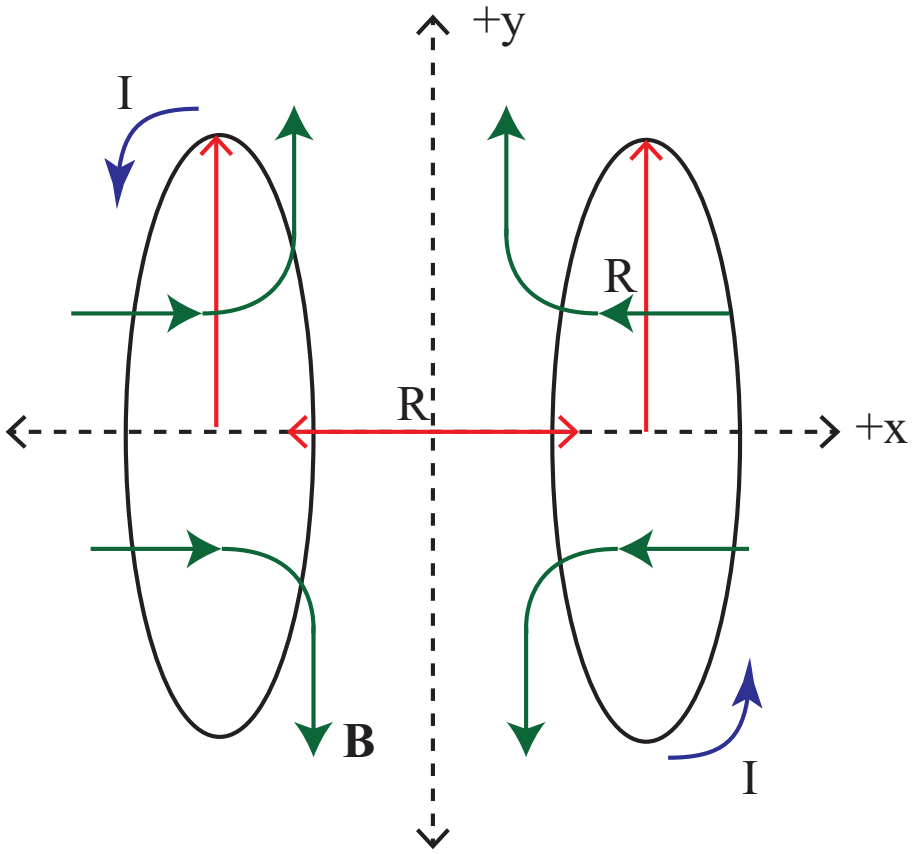

Figure 17: Main coil arrangement used to generate the anti-Helmholtz magnetic field used to realize the MOT. The magnitude of the magnetic field in the center of such an arrangement vanishes. The direction of the currents and the resultant magnetic fields are indicated by the blue and green arrows.

in. externally and 0.0016 in. internally and were wrapped in a 5X5 layer of 24 turns with a radius of 3.0 in. The main coils were mounted around the larger viewports of the chamber with the common axis lying along the symmetry axis of the chamber. To create the MOT a $\approx$ 16A current was delivered to create an inhomogeneous magnetic field between these coils $\approx$ 16G/cm that vanished at the center. This current was supplied by a 400-A DC current supply and controlled remotely by the LabView computer program.

Also necessary to maintain the MOT was an additional series of coils to nullify the Earth's magnetic field. This was done by positioning three pairs of coils on all six sides of the vacuum chamber. These coils also had the additional affect of nullifying any magnetic fields from the ion pump. Each of these coils had currents that flowed in the same direction supplied by a

separate homemade voltage-to-current converter circuit that was controlled by the LabView computer program.

3.2.4 BEC creation

The steps to creating a BEC begin with creating a MOT of around 30 million atoms and subjecting to the high powered FORT beam. This beam overlapped with the MOT for about 30 seconds thus loading the atoms into the FORT.

The repump beam was then reduced in power about 100 times from ≈ 2.4 mW used to create the MOT down to $\approx 12\mu$W to create what is known from the literature as a "dark spontaneous-force optical trap" or dark SPOT [67]. This step was very important as the atoms were prepared into a state that was "dark" to the cooling light. This thus decreased the recoil heating and as a result increased the phase space density. The cooling light was then detuned to -78 MHz so that atoms would experience the MOT beams negatively detuned. This effect was realized even after considerations of the AC-stark shift on the atoms were taken into account. After 60 ms the MOT beams and repump beam were all turned off by the fast mechanical shutters and the magnetic field from the main coils was turned off by setting their currents to zero. This then loaded around 3 million atoms into the dipole trap. To further optimize the loading the waist of the FORT beam was reduced from 100μm down to 25μm and this then increased the elastic collision rate and thus increased the efficiency of the evaporative cooling.

The succeeding two-stage process was known as Evaporative Cooling or "EVC1" and "EVC2". For EVC1 the CO_2 laser was ramped-down exponentially from 25 W to around 1 W with a time constant of 2 seconds by reducing the RF power driving the CO_2 AOM. During EVC2 the laser power was further reduced in a series of short steps with increasing time intervals in each step (The first step was around 50 ms while the final steps were around 200 ms in duration.) after which this was followed by a wait time of around 400 ms to allow for re-thermalization. Also during this process the power of the CO_2 was reduced in distinct

stages to around 50 mW over ≈ 5 s. This process effectively removes the upper end of the Maxwell-Boltzman distribution of the remaining atoms and thus these atoms rethermalized to a lower temperature and a higher phase space density [74]. After EVC2 the remaining atoms arrive at the required phase space density and critical temperature to realize a BEC of around 50 000 atoms in the $5^2S_{1/2}, F = 1$ state ready for application of perturbations relevant to the experiment to be conducted.

3.2.5 Imaging and Spontaneous Emission Setup

In order to image the BEC and experimental results a destructive imaging technique was used. After the BEC is created the FORT is switched off and the experimental sequence is thereafter applied after which the repump light was switched back on. This repump light causes the atoms to be pumped to the $5^2S_{1/2}, F = 2$ excited state from the $5^2S_{1/2}, F = 1$ state. After a time-of-flight (TOF) of about 10 ms, the atoms were then subjected to a pulse of imaging light on resonance with the $5^2S_{1/2}, F = 2 \rightarrow 5^2P_{3/2}, F' = 3$ transition for about 60μs thus completing the imaging process. This imaging transtion is shown in Fig. 18 (Adapted from [26, 108]).

The optical arrangement to realize the imaging process is shown in Fig. 19 (Adapted from [26, 108]).

A small amount of the light on resonance with the aforementioned transition was picked off from the light from fiber-1 to be then expanded by an expander to have a diameter of about 1 cm. This was then passed through a quarter-wave plate to make the light circularly polarized to be then delivered to the chamber. The imaging process itself was done by an absorption imaging technique where the on-resonant light interacts with the atoms. Once the BEC or diffracted atoms were exposed to the light the photons are scattered and a shadow is cast upon a high-resolution CCD camera (ANDOR DV437-BV). This camera's temperature and exposure time were controlled by a separate ANDOR program on a separate computer along with the usual LabView computer program. During the experiment it was crucial to

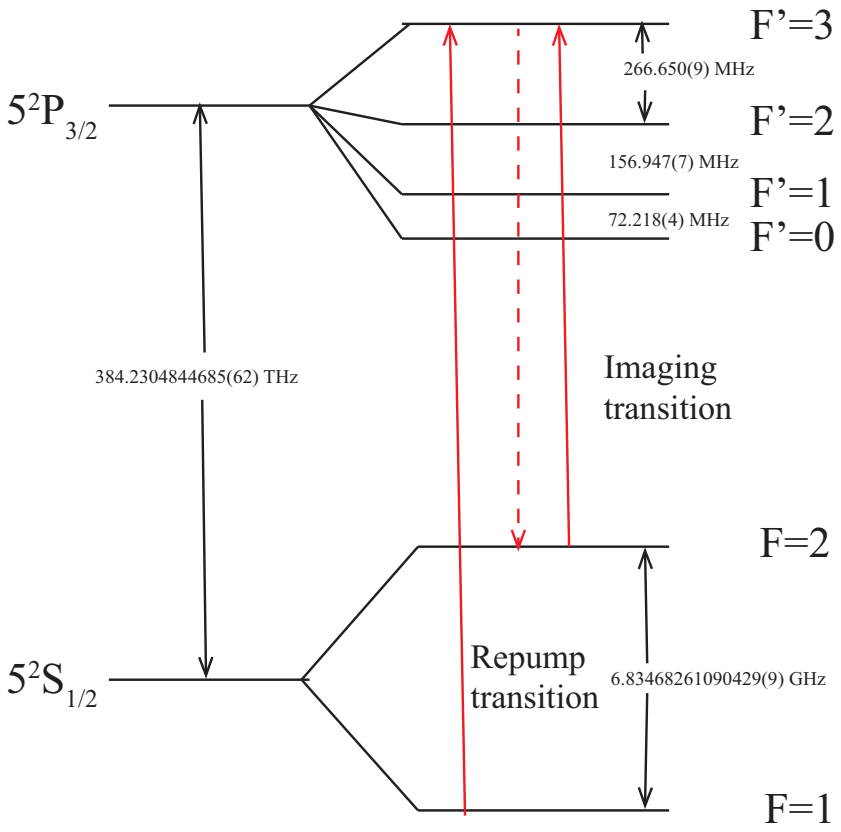

Figure 18: Frequency transition that was required for imaging of the atoms after an experimental run. The repump was reapplied after a TOF of ≈ 10 ms to prepare the atoms into the $5^2S_{1/2}, F = 2$ state before the imaging light resonant with the $5^2S_{1/2}, F = 2 \rightarrow 5^2P_{3/2}, F' = 3$ transition was applied.

be able to monitor the MOT in real time with two security CCD cameras, one viewing the large side port and another viewing a port at the top of the octagonal chamber. This gave a convenient ability to view the MOT shape from two different angles.

After the imaging was done it was necessary to calculate the number atoms in order to further calculate the mean momentum and mean energy to analyze our results. This was done by considering the intensity, I, loss of a laser beam in the z-direction passing through a sample of atoms. This is given by Eq. 3.2.1 [108, 26]

$$\frac{dI}{dz} = -\sigma n I, \tag{3.2.1}$$

where n is the density of the atoms, $\sigma = \hbar\omega\gamma/2I_S$ is the absorption cross section in which

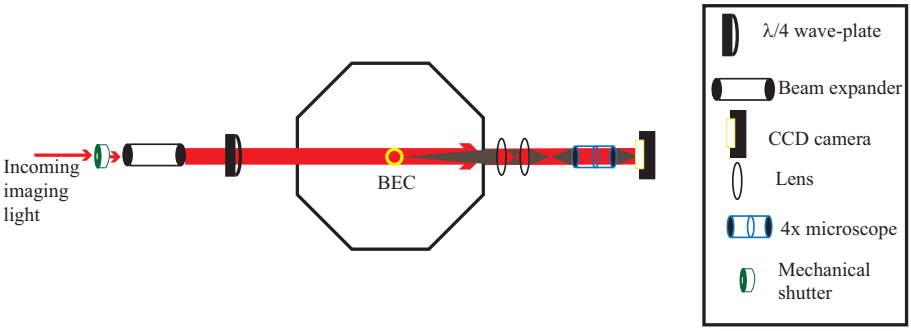

Figure 19: Schematic of imaging setup.

ω is the laser frequency, γ is the natural linewidth, and I_S is the saturation intensity. The solution to the differential equation given by Eq. 3.2.1 is

$$I\left(x,y\right) = I_0 e^{-\sigma\tilde{n}}. \tag{3.2.2}$$

Here $\tilde{n}$ is the column density which is defined as the number atoms per unit area. This intensity was found by taking two separate images in which one was taken with the atoms (known as "signal" in experiment), I_{Sig} and another without (known as the "reference") labeled as I_{Ref}. The intensity profile was then defined as the ratio

$$I(x,y) = \frac{I_{\text{Ref}}}{I_{\text{Sig}}}. \tag{3.2.3}$$

Using these results the number of atoms present can then be calculating by integrating over the column density

$$N = -\frac{S}{\sigma}\sum_{\text{pixels}} \ln(I). \tag{3.2.4}$$

Here, $S = (13\mu\text{m})^2$ is the area of a pixel within the CCD camera and this sum was carried over all of the pixels.

The imaging system also served as the method of realizing the spontaneous emission (SE) whereupon the imaging light was switched on for very short intervals $\approx 30\mu$s and was engineered by the LabView computer program to apply during the microwave coin pulses only

and avoid interfering with the kicking pulses. It is very important to note that this method has limitations because as the power and number of such pulses increases the likelihood of oversaturating the CCD camera also increases. However, this did not prevent us from obtaining the necessary data for our experiments.

3.2.6 AOKR setup

To realize the AOKR system necessary for the Bragg and momentum shift operations during the quantum walk a separate grating stabilized TOPTICA DL 100 was used to create the necessary laser pulses. The frequency of this laser was not locked to any transition frequency although it was set to a position halfway between the $5^2S_{1/2}, F = 1$ and $F = 2$ hyperfine levels of the ground state to the $5^2P_{3/2}, F' = 3$ excited state. This frequency is labeled on the energy level diagram given by Fig. 20 (Adapted from [26, 108]). This particular laser frequency (The detuning here was ± 3.4 GHz from either level of the ground state) was used to ensure that atoms in both energy levels would experience the same kicking strengths.

Similar to the MOT laser as discussed in section 3.1, the kicking laser was injection locked to a separate "kicking slave" homemade laser to ramp up the overall power of kicking light to be sent to the chamber. As before, a small amount of the light from the "master kicking" and "slave kicking" lasers was picked off to be sent to a ^{87}Rb cell to obtain the saturated absorption spectrum signal to ensure good injection locking. The amplified light from the "slave kicking" laser was then sent to a splitting cube to obtain a 50-50 split of the light. Both beams had a power of ≈ 13 mW and were sent to be passed through two separate ISOMET, 40N AOMs. After each AOM the first positive order of the diffracted light was then delivered to the vacuum chamber via two viewports sharing a pair of MOT beams. This caused the kicking beams to enter counter-propagating to one another in the chamber. To create the horizontal standing wave both kicking beams were set to make an angle of 53° giving a final wavelength of $\lambda_G = \lambda / (2 \sin(53°))$ where $\lambda = 780$ nm. Both AOMs used in the kicking setup were driven by an RF signal supplied by a pair of programmable arbitrary waveform

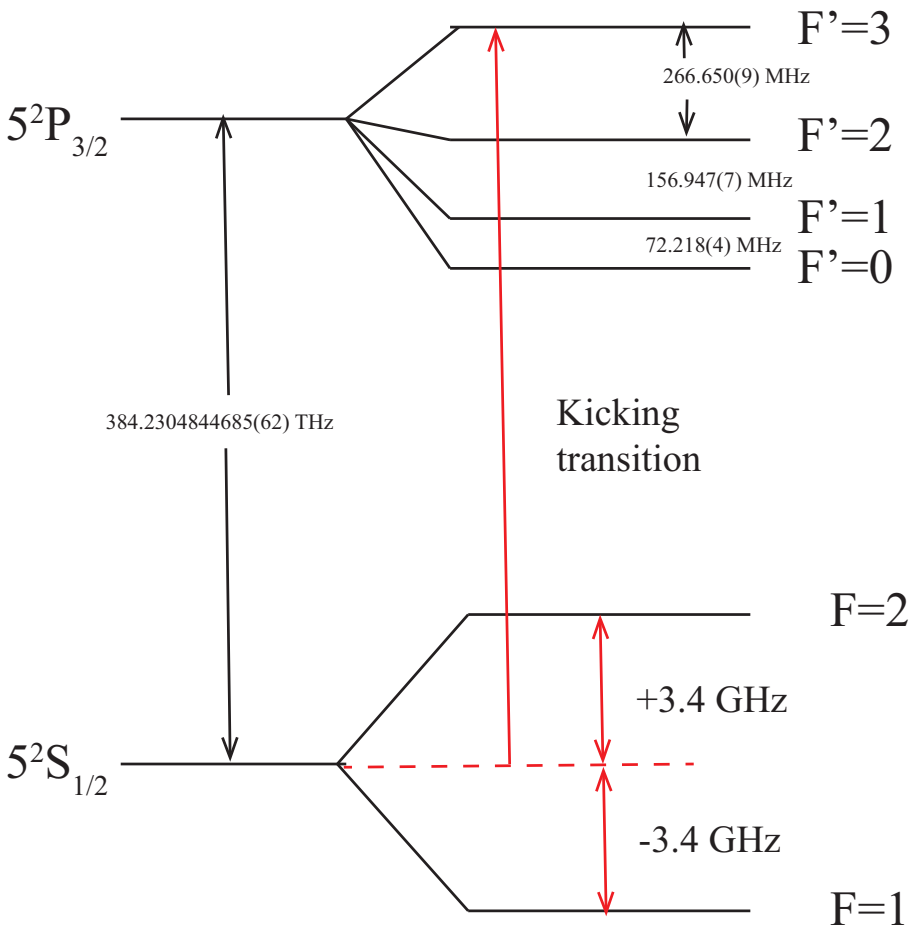

Figure 20: Frequency transition that the kicking laser was set to realize an AOKR. It must be noted that this laser was not frequency locked to this transition and had to be maintained to ensure that equivalent kicking strengths was delivered to both states.

synthesizers (HP8770A) before being passed through a pair of 1-W amplifiers. One AOM was driven at a frequency of 30 MHz by one of the HP8770As ("master") while the other HP8770A was driven at a variable frequency ("slave") and was phase locked to the "master". Both HP8770As were programmed and controlled by a GPIB interface card (National Instruments) that allowed for control of all RF waveform properties via the LabView computer program.

The properties of the standing wave pulses were engineered by using the HP8770As to adjust the phase, intensity, pulse length, and frequency between the two kicking beams. The signal was then sent to the AOMs to realize the desired standing wave for the experiment. The standing wave nodes were displaced by a velocity given by $v = 2\pi\Delta f/G$ where Δf gives

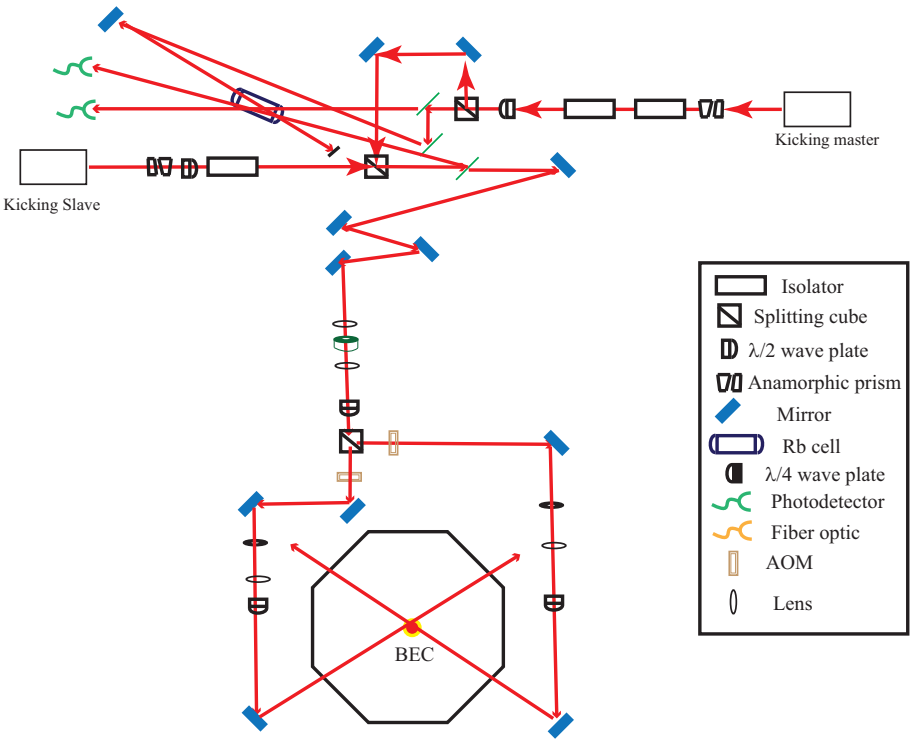

Figure 21: Schematic of the kicking setup.

the frequency difference between the beams. Because the quasimomentum, β, of the BEC is proportional to v one can use Δf to control β during the experiment. To ensure that the applied kicking pulses remained in the Raman-Nath regime the duration of the kicking pulses was adjusted to be 384 ns for all experiments. In other words, this ensures that the distance that the atoms travel during a pulse is much smaller than the spatial period of the potential.

3.2.7 Microwave System

To realize the gate and coin pulses necessary for the QW a microwave system was setup according to the schematic shown in Fig. 22 (Adapted from [26, 108]). Two signals were used to generate the MW pulses by mixing the separate signals. One of these signals was a continuous MW signal with a constant frequency of (6.80 GHz) and the other signal was a pulsed RF signal with an adjustable frequency of $\approx$ 34.682610 MHz. A reference 10 MHz frequency was generated by a Rubidium atomic clock and was used to supply both the locking

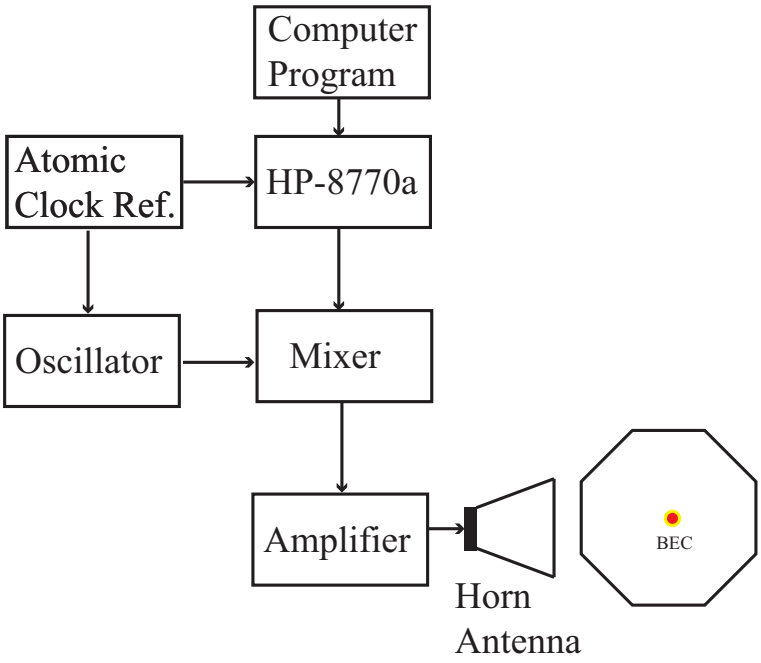

Figure 22: Schematic of the microwave setup.

signal for a 6.80 GHz crystal oscillator (Microwave Dynamics, PLO-4000) and an external clock signal for a third HP8770A waveform synthesizer. The HP8770A allowed for control of the length, phase, and frequency of the RF pulses. This HP8770A was also synchronized with the aforementioned HP8770As used for generating the AOKR pulses to ensure the phase and timing of the MW and AOKR pulses were set as desired for the experiments [26].

The MW signal to be sent to the chamber was realized by combining the crystal and HP8770A signals in a frequency mixer (Marki Microwave) resulting in pulses of ≈ 6.834682610 GHz. This is a frequency corresponding to the $5^2S_{1/2}, F = 1, m_F = 0 \leftrightarrow 5^2S_{1/2}, F = 2, m_F = 0$ transition in ^{87}Rb. The location of this transition is shown in Fig. 23 (Adapted from [26]).

This signal was verified using a spectrum analyzer (Agilent, E4407B). The generated microwave signal was too weak to generate the desired pulses and thus it was sent to a Terrasat Communications, ED-0278-4 amplifier to give an output power of $\approx$ 30dBm. This amplified signal was then sent to C-band horn antenna mounted near the large viewport of the vacuum chamber. The intensity of the MW pulses was tuned by adjusting the voltage

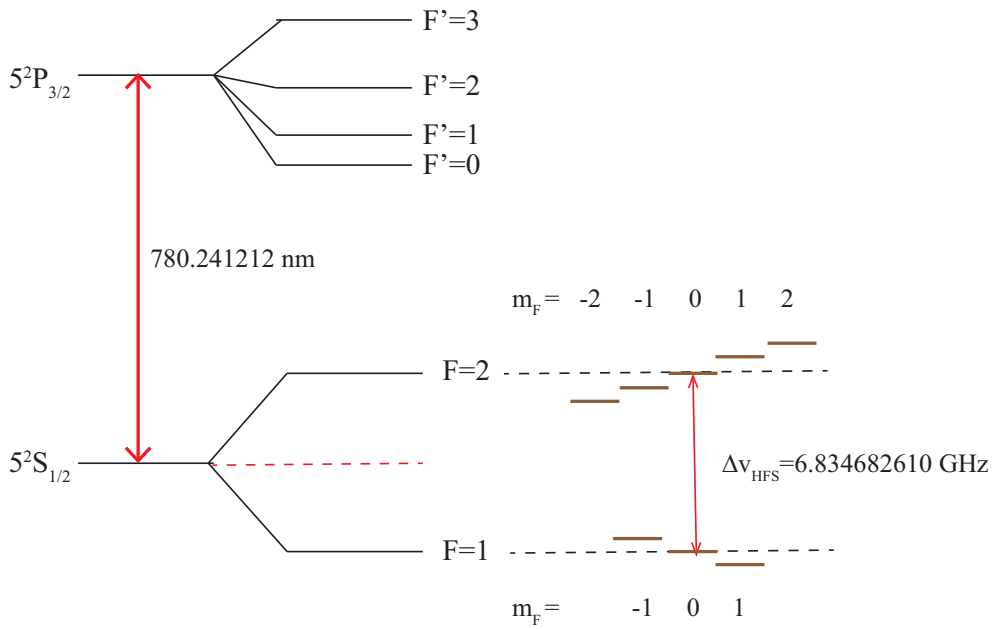

Figure 23: Hyperfine level transitions for ^{87}Rb with the frequency used to generate the microwave pulses indicated by the red arrow. This frequency was the transition between the $|F = 1, m_F = 0\rangle$ and $|F = 2, m_F = 0\rangle$ states.

sent to the amplifier which in turn adjusted the amplification of the received MW signal. This voltage adjustment was done on the LabView computer program and had an adjustable range of $0 - 5$V.

CHAPTER IV

RESULTS AND DISCUSSION

In this chapter we will discuss and analyze the experimental results obtained from the spontaneous emission experiments as well as the predictions made from the new light shift model to explain the central peak of residual atoms present in all of our QW experiment up to this point. The discussion will first start with the initial method that was attempted to cause an increase of spontaneous emission and that was by increasing the intensity of one of the two kicking beams while reducing the intensity of the other to maintain the desired kicking strength. We will then analyze these results and also show why it wasn't able to provide the necessary background light source to cause an increase in probability of spontaneous emission events. Afterwards we will discuss in detail the results of the application of an extra light source using the imaging beam. All of these results enable us to more carefully determine the robustness of the QW so that it can be used in further applications.

4.1 Unbalanced AOKR method

In this section we will present results in which the first attempt to realize extra spontaneous emission during the QW utilized the kicking beams themselves to increase the amplitude of the constant term in the kicking operator U_{kick}. To theoretically accomplish this one can increase the intensity of one side of the AOKR beams. This would, in effect increase the intensity of the background radiation field that the atoms are present in during the walk and

thus increase the spontaneous emission rate as described by[50]

$$\gamma_m = \frac{\phi_d}{\tau_p \tau_{SE} \Delta_m}, \tag{4.1.1}$$

where τ_p, and τ_{SE} are the pulse duration and inverse of the spontaneous emission rate respectively. Note that from Eq. 4.1.1 we might be tempted to just simply increase the duration of the kicks but this would cause our system to exit the Raman-Nath regime and completely change the dynamics of the system. As a result the only realistic option is to set the amplitude of one kicking beam higher than the other and also making fine adjustments in the amplitude of both beams to maintain proper kicking strength. We saw little change in momentum distribution changes from one amplitude setting to another and also not many atoms were lost beyond a normal experiment. Next attempts were done with ever increasing amplitude difference up until the amplitude setting were reaching the limits of the experiment and one of these results is shown in Fig. 24. The TOF images in panel (a) of Fig. 24 show that even with a power difference of nearly 5 mW between the kicking beams the momentum distribution still was largely unchanged aside from the effects of global phase induced by the larger constant term in the kicking potential. In Fig. 24(b) the mean energy was extracted from the images in Fig. 24(a) and plotted against the power difference, ΔP between the two AOKR beams and we can see that the mean energy only differs by about $0.5\ \frac{\hbar^2 G^2}{2}$. The number of condensed atoms plotted against ΔP in Fig. 24(c) also doesn't show significant loss of condensed atoms as would be expected for SE. All of these results show that attempting to utilize the kicking lasers themselves to increase the SE rate is an inadequate procedure due to the limitations of the experiment. If one was to have a pair of AOKR beams capable of higher intensity it may be possible to induce SE with this method while maintaining the Raman-Nath regime. A more systematic and convenient approach was then found in using the imaging light as an external source of spontaneous emission and applying it during the QW as we will discuss next.

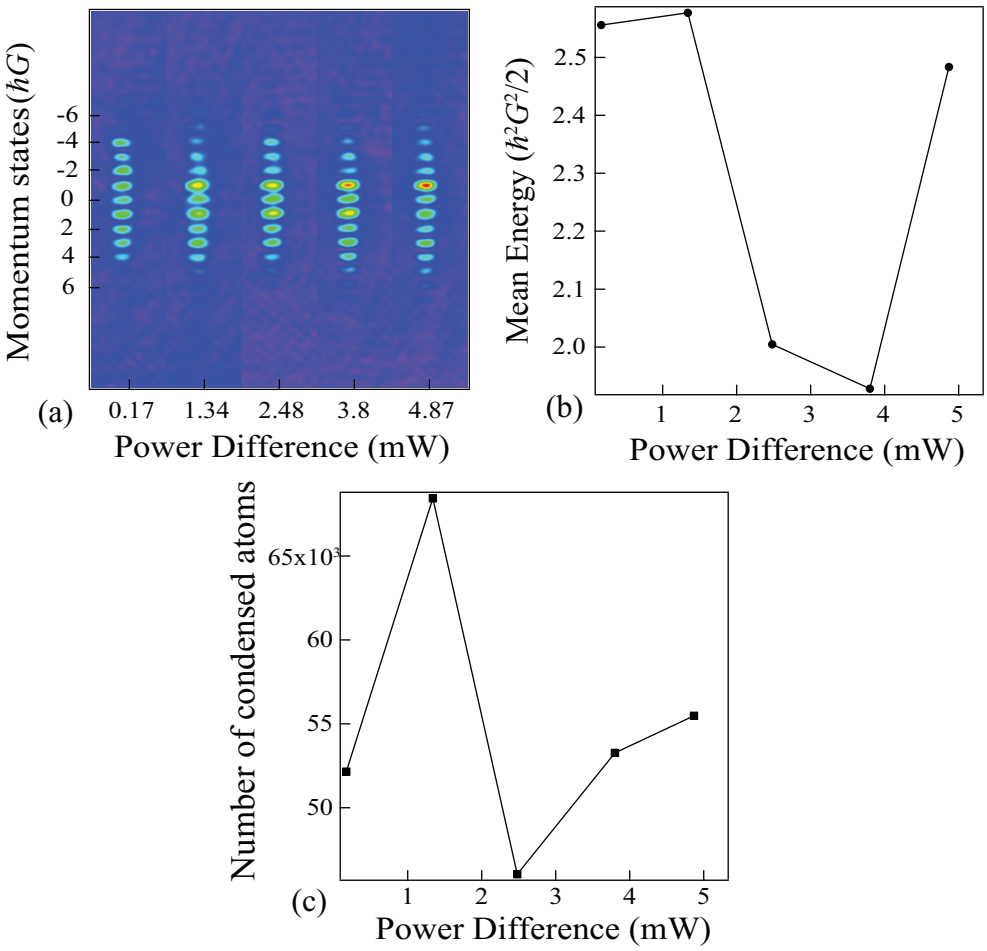

Figure 24: (a)TOF images of a five step QW as a function of power difference in the applied AOKR beams. The mean energy (b) and the number of condensed atoms (c) extracted from panel (a) These results were from the unsuccessful attempts of the early experiments.

4.2 Spontaneous Emission

After the negative results of utilizing the AOKR lasers it was then decided to apply the imaging light during the QW. This approach had the main advantages of being both readily tunable in intensity and duration. It could also be properly timed to align at any point during the QW. After some early attempts it was found that the most desirable timing to apply an SE pulse with this beam was during the coin microwave pulses only. This was done to avoid interference with the kicking pulses as this would also completely change the dynamics of the system [100]. Because of the fact that the program controlling the imaging light was not using one of the HP-8770a synthesizers the timing of the imaging pulses could

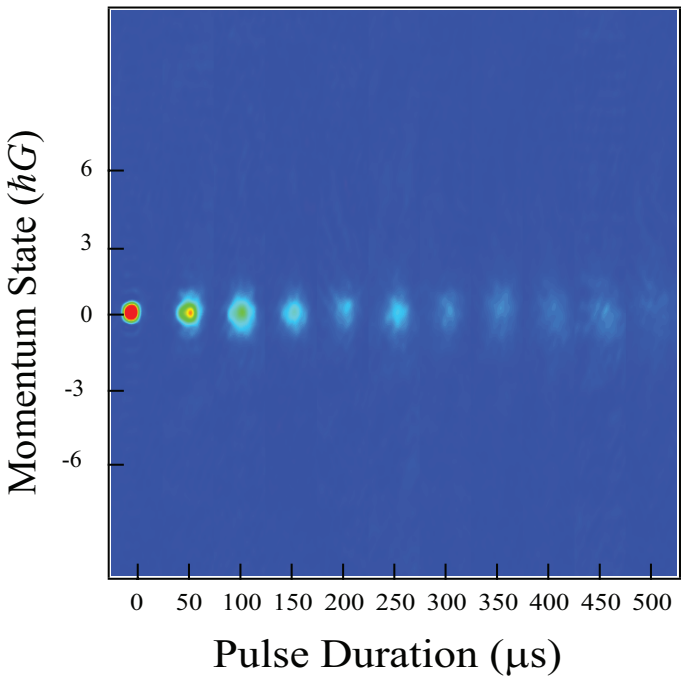

Figure 25: TOF images of a BEC first prepared in the $|F = 2, m_F = 0\rangle$ state before being subjected to an imaging pulse of increasing duration.

vary by a few microseconds. To reduce the effects of this the duration of the pulses was set to be 30 μs for each SE pulse. This also had an additional advantage of reducing the probability of saturating the CCD camera.

It is important to note that using imaging light required additional experimental runs on the BEC alone to obtain data that could be used to numerically calculate the effects of the spontaneous emission. This is due to the fact that this light was of a different frequency compared with the kicking light. This allowed us to calculate the SE probability rate ρ by using the measured exponential decreases in atom population in 50 μs intervals and SE power of 3 μW after the BEC was initially prepared in the $F = 2$ states using a π MW pulse [24]. The results of this are shown in Fig. 26 and the condensate fraction in Fig. 27 [24] This exponential fit enabled us to accurately estimate an effective SE rate $\rho \approx 0.35$. With this estimate in mind we ran a five step QW with a kick strength of $\phi_d = 1.45$ and increasing the SE rate up to $\rho = 5.38$ and the TOF images and momentum distributions of this are shown in Fig. 28 and Fig. 29 [24]. This shift in momentum states confirms the numerical

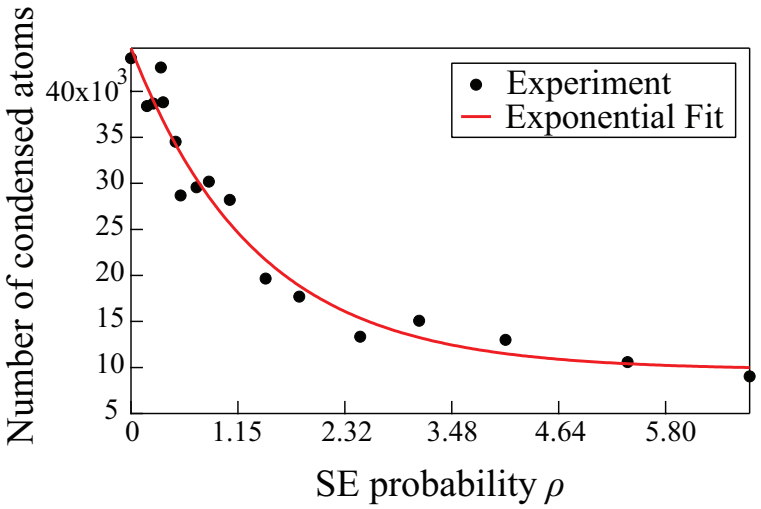

Figure 26: Measured number of atoms after a BEC subjected to SE pulses of increasing duration in 50 μs intervals. This was also fitted with an exponential function to calculate the effective SE rate.

simulations because the SE light induces an imbalance of the internal state of the atoms towards the $|F = 2\rangle$ state and thus creating a bias in the momentum distribution because the projection of $|F = 2\rangle$ moves into the direction of positive momenta. This momentum shift can also be observed in the calculated mean momentum extracted from the TOF images and the momentum distributions. The results of this analysis are shown in Fig. 30. After this result it was decided run a similar experiment but with a more properly compensated QW. We also noted that from the uncompensated results that the effects of SE are well noticeable at an SE rate of around $\rho = 2.48$ and thus in the compensated experiment we ended the SE scan with this setting. This QW was also done with a higher kick strength of $\phi_d = 2.0$ to widen the momentum distribution so that the behavior could be more clearly observed. The TOF images and momentum distributions are shown in Fig. 31 and Fig. 32 [24]. We can see that similar to the results of the non-compensated walks the momentum distributions will shift to the positive momentum states. This thus further verifies the theoretical predictions and it also shows that the positive shift will occur regardless if the QW is compensated for phase or not. These results showed us the imaging light clearly can be used as a convenient tunable external source of spontaneous emission and opened the opportunity to study another

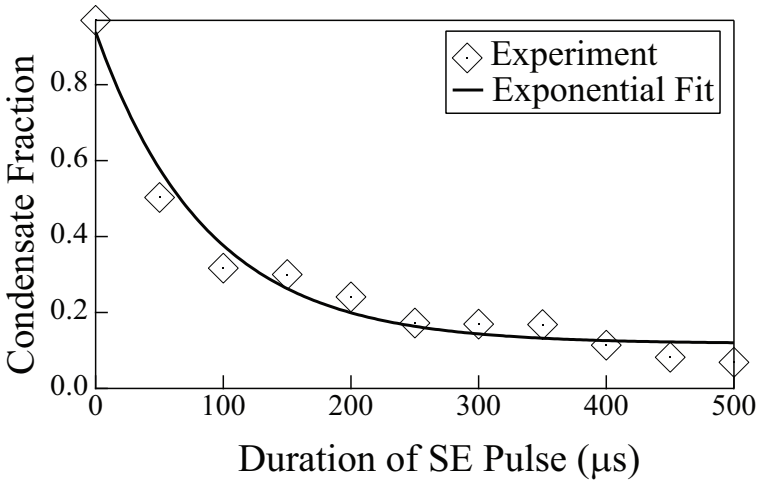

Figure 27: Condensate fraction calculated from TOF images in Fig. 25. Adapted from [24].

important phenomenon of the QW and that was the quantum-to-classical transition. One of the most important questions that appears when studying a QW is: What is the threshold between quantum and classical behavior? This is especially important if one wishes to use a QW in applications. As a result, more SE experiments on the QW were conducted with this in mind. In this experiment SE was applied over the QW at each step and the SE rate was measured for each iteration. The mean energy of this data was then extracted from each step and then plotted against the number of QW steps. The results of this along with theoretical simulations are shown in Fig. 33. This data was then fitted using a linear fit in order to estimate the rate of change in mean enegy R and the results are tabulated along with theoretical data in Table 3. This quantity shows that as the SE rate increases the R for the mean energy will decrease starting with a maximum value when no SE light is present. These observations are in good agreement with the predicted quantum-to-classical walk transition. This also shows that as the SE rate is tuned the QW will make a gradual transition to classical behavior possessing less mean energy which is more characteristic of a classical walk with a Gaussian distribution. This is because the SE rate eventually becomes strong enough to annihilate the entanglement of the internal spin states. These experimental observations were also verified with the theoretical predictions which showed similar behavior. The results of this experiment indicate that the rate of the mean energy

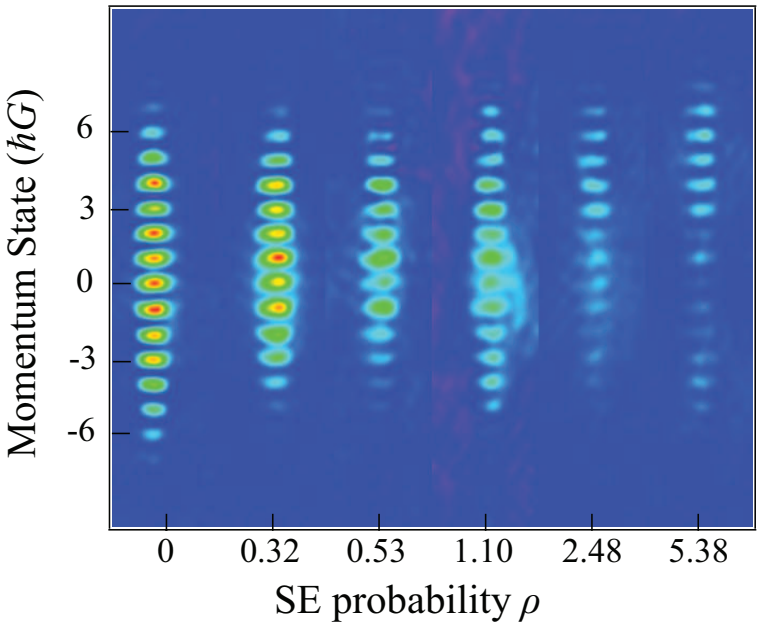

Figure 28: TOF images of five step QW with $\phi_d = 1.45$ without phase compensation. Note the dramatic shift of atom population to positive momentum states. Adapted from [24].

SE Probability	Experimental Rate R	Theoretical Rate R
$\rho = 0$	0.58	0.84
$\rho = 0.24$	0.53	0.68
$\rho = 0.35$	0.52	0.64
$\rho = 0.54$	0.51	0.58

Table 3: Rate R calculated from the experimental and theoretical data of Fig. 33. Adapted from [24].

could be used to more precisely locate the SE rate that can give rise to classical behavior especially with QWs at smaller numbers of steps. We can also see that our QW is quite robust at smaller numbers of steps before being destroyed by the SE rate.

4.3 Predicted effects of Light shift on the QW and possible corrective techniques

In this section we present some numerical data illustrating the effects that the AC stark shift from the AOKR as described in Chapter 2 has on the QW. We will also describe some possible techniques that could be used to help mitigate these defects in our QW experiments

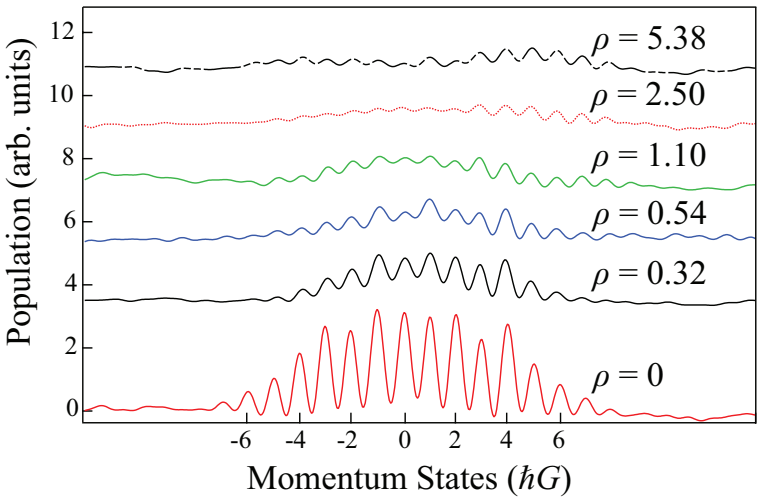

Figure 29: Momentum distributions of the TOF images in Fig. 28. Note the shift towards positive momentum as the SE rate increases. Each distribution curve was offset for added clarity. Adapted from [24].

which will in turn help with further applications [14]. As was noted before the AOKR induces a phase shift which is due to the AC stark shift from the kicking lasers. In past experiments including the SE experiments this phase shift was countered by a trial-and-error method of scanning the χ phase of the $\hat{\boldsymbol{M}}(\theta, \chi)$ coin microwave operator at a particular number of steps until the proper momentum distribution was observed. The chief problems of this approach was that it was time consuming and that it didn't completely counter the phase issue and thus requiring a further fine adjustment if the QW was to be conducted beyond the step in which the phase compensation was found. This is simply due to the fact that each additional QW step added to the contributions of this shift. These issues unfortunately cause some limitations for using the QW to realize further and more complicated applications such as realizing topological phenomena or quantum search algorithms. As a result of the recent theoretical model outlined in Chapter 2 in which the Stark shift plays more of role in the QW two major possible mitigation techniques have been proposed that could be attempted in an experiment without too much difficulty. If we were to swap the coin and Hadamard gate operators that have been applied in each experiment up to this point, then according to the numerical results of Fig. 34 [14] the predicted distribution better approaches

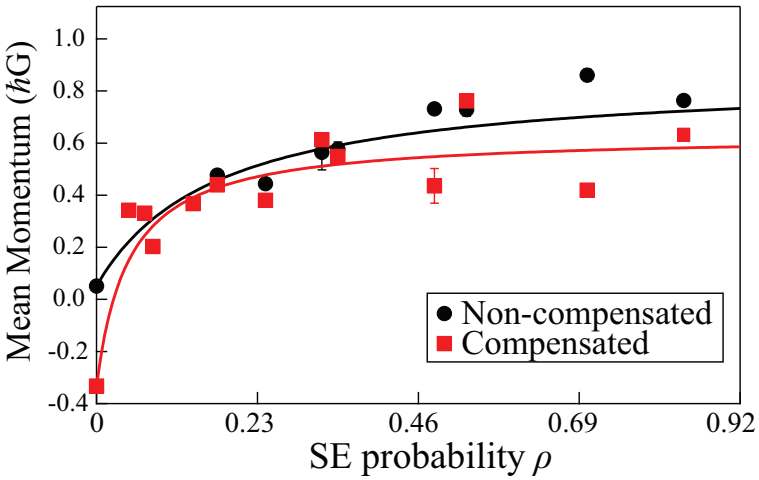

Figure 30: Mean momentum values extracted from both uncompensated and compensated QW TOF images. The fitting curves are to more clearly illustrate the behavior of the data. Adapted from [24].

an ideal symmetric QW. The left panel of Fig. 34 [14] shows that even a straightforward of exchanging the coin and gate operators results in a QW that reduces the central region of atoms fairly well while also increasing the characteristic "horns" of the QW. The initial state experimentally implemented was expressed by Eq. 2.2.68 with two involved momenta. As described in [27, 24], the state is constructed to be concentrated in position space at the rising (falling) flanks of the potential where the force impulse towards the left (right) is maximal. It is exactly this effect that leads to directed ratchetlike motion. The more momentum states that are included in the initial state, the more densely peaked is the wave function in position (angle) space. For a highly dense wave function in position space, the directed motion works with minimal dispersion. This dispersion is a specific problem in our AOKR walk with respect to an ideal quantum walk. Hence, it is indeed not too surprising that the AOKR QWs become more similar to ideal QWs when using "better" ratchet initial states. This is seen in Fig. 34 [14] for the walk with the new Hadamard coin $\hat{GH}$ during the evolution steps. The artificial clumping at the center of the momentum distributions disappears when more momentum classes are included in the initial states (see Fig. 34). It is known that an ideal quantum walk does not display a central peak from the start, independently of the initial state (see Ref. [63]). The consequence is that an ideal walk does

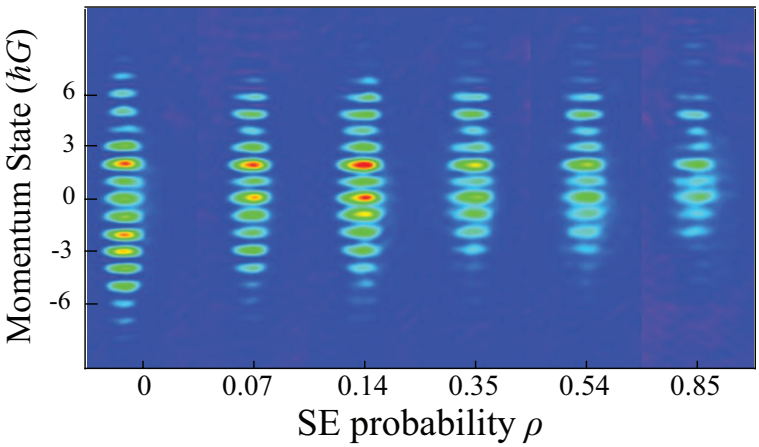

Figure 31: TOF images of a compensated five-step QW with a $\phi_d = 2.0$ and maximum SE rate of $\rho = 0.85$. The atom populations again shift toward positive momentum states. Adapted from [24].

not display any difference between the various implementations using the different balanced coins described above. In the end, the dominant central peak, displayed when using the $\hat{G}_H$ coin, can be seen as an artifact from AOKR realization when using the simplest initial state. This central peak disappears when adding more momentum classes to the initial state as seen in Fig. 34 [14]. This provides a clear prediction that could easily be checked in future experiments. In other words, the experimentally observed residual central peak is actually a relic of the AOKR dynamics. This behavior is expected when in the walk protocol due to light shift effects the effectively implemented coin during the walk is $\hat{G}_H$ and not $\hat{Y}$, as initially intended. Even when this is the case, the central peak is only visible for an initial ratchet state sufficiently narrow in momentum space. An additional possible technique that can be applied, in addition to swapping operators, is to increase the number of initial states to be used in the QW. The results of this are shown on the right panel of Fig. 34 for initial states up to five. The results of this show that the momentum distribution of the QW would be improved dramatically to where the central region of atoms nearly vanishes with three additional states. Such an improvement is due to the fact that increasing the number of initial states causes the wavefunction to be more densely peaked in position space. This in effect creates a better quantum ratchet that leads to a QW

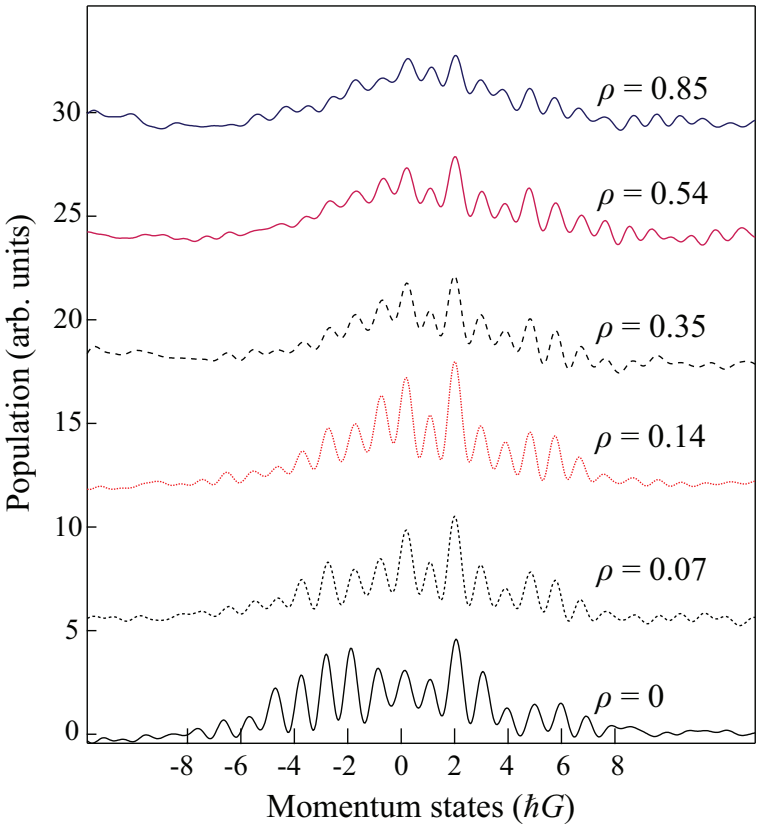

Figure 32: Momentum distributions from the TOF images of Fig. 31 with similar offset applied to each curve for clarity. Note that the positive shift in momentum is well observed. Adapted from [24].

resembling more ideal behavior. The properties of multiple Bragg pulses and their affects on the quantum ratchet have been studied in previous experiments and thus this technique could be attempted. However, it should be noted that increasing the number of initial states is not trivial as the multiple Bragg pulses each have to be tuned to result in states with equal populations to avoid bias in the QW. To ensure that such a new explanation still agrees with the QW experiments conducted in the past it was necessary to perform some further simulations that compared the original phase-compensated QWs with that of the swapping of the coin operators. Each of these were done at different quasi-momentum values and the results are shown in Fig. 35 [14]. We have put forward an alternative way of understanding the central peaks around zero momentum in the experimental implementations of the AOKR quantum walks. To simulate experimental systems, we must include the finite width in the

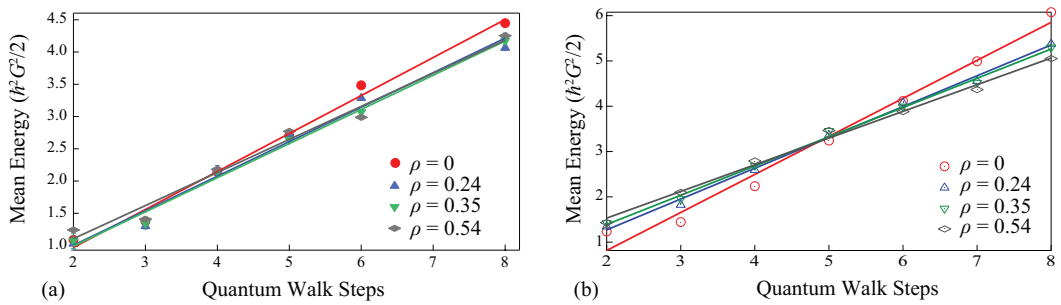

Figure 33: (a) Mean energy extracted from TOF images plotted as a function of the QW steps at various SE probability ρ and $k = 1.4$. Note that difference in the mean energy among various SE probability ρ remains relatively constant at a lower number of steps but begins to decrease at six steps, indicating a transition from a QW to a classical walk. (b) Theoretical predictions based on the experimental conditions for the data shown in Panel (a). The solid lines in both panels represent the linear fitting functions. Adapted from [24].

initial quasimomentum distribution of the spinor BECs mentioned in chapter 2. This is best done numerically by averaging over a reasonable ensemble of quasimomenta β [48]. Nonresonant β induces a phase scrambling [101, 128], making the walks less ballistic with the effect of reducing the population in the ballistically moving side peaks. The value of β, drawn from a Gaussian distribution of a certain width β_{FWHM}, was estimated in the experiments as $\beta_{FWHM} \approx 0.025$ (see Refs. [26, 24]). The numerical walks are obtained as an average over 1000 realizations, with each realization involving a value of β being randomly drawn from the corresponding Gaussian. In the left panels of Fig. 35 [14], the walks are implemented by the $\hat{G}_H$ coin, while the right panels feature the implementation of Eq. 2.4.13. In other words, while the left panels show the walk that we argue to be responsible for the experimentally observed momentum distributions, the right panels show theoretical predictions using experimental parameters based on the originally proposed $\hat{W}$ coin and an incorrectly chosen compensation phase (see Eq. 2.4.13) with $\chi = \pi$ and $k = 1.45$. As anticipated, the latter two protocols given by Eqs. 2.4.12 and 2.4.13 essentially lead to the same momentum distributions for all choices of $\beta_{FWHM} = 0$ in Figs. 35(a) and 35(b), $\beta_{FWHM} = 0.01$ in Figs. 35(c) and 35(d), and $\beta_{FWHM} = 0.025$ in Figs. 35(e) and 35(f). With increasing β_{FWHM}, the side peaks and the central regions become less and less distinct and the ballistic side peaks tend to fade out. Similar behavior is seen in our experimental

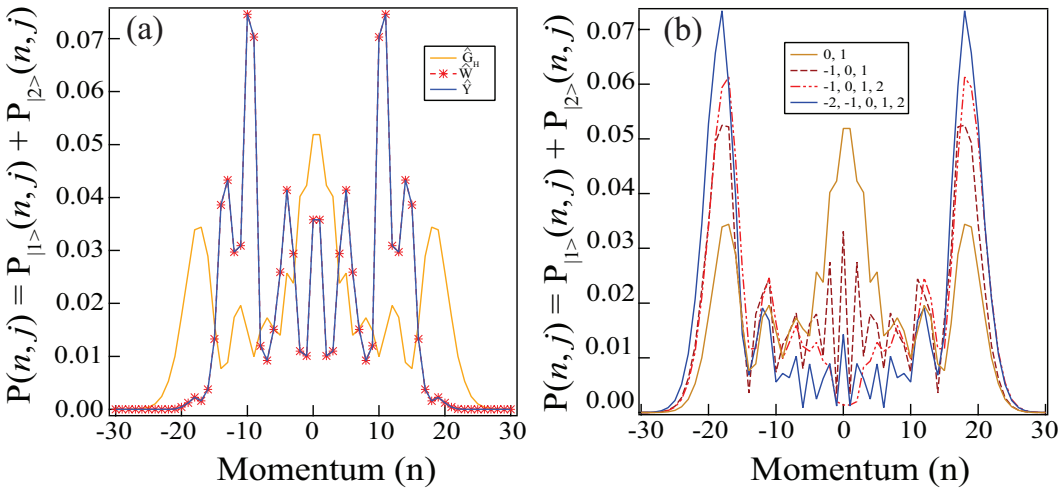

Figure 34: Predicted QW distributions after 20 steps. In panel (a) the Hadamard gate and coin operators were exchanged. Panel (b) also has the operators swapped but each curve represents an increasing number of initial states. Adapted from [14].

data [27, 24]. Fig. 36 (a) [14] shows a typical experimental result adapted from Ref. [26]. We find good theory-experiment agreements by comparing Fig. 36(a) with Fig. 36(b) that shows the predictions of our current model (see Eq. 2.4.12). First, we observe in both panels (a) and (b) in Fig. 36 a central part that does not evolve far away from the origin and the two side peaks that evolve ballistically away from their initial position in momentum space. Second, the observed and predicted rates of the spread of these side peaks in momentum space with increasing number of steps appear comparable. Our current interpretation shown in Fig. 36(b) would also be in reasonable agreement with the originally guessed temperature of the BEC with $\beta_{FWHM} \approx 0.025$, when the fading of the side peaks is considered. Figure 36(c) shows momentum distributions of the QW given by the previous theoretical model (see Chapter 2) after a residual thermal cloud of atoms is added into the BECs. The thermal cloud was originally assumed as a possible solution for the appearance of the prominent central region. Thermal atoms essentially will not follow the kicking evolution [101, 128] and hence remain close to the center. The experimentally intended $\hat{Y}$ protocol does not display this behavior, as can be seen from Fig. 35. However, the QWs shown in Fig. 36(c) appear to be different from our experimental observations, i.e., the predicted QWs lack the significantly contributing central region and the structures of the side peaks are of a

quite different shape. The mean energies of the present and original theoretical models were calculated and compared with experimental data in Fig. 37 [14]. It can be seen that the energy using $\hat{G}_H$ coin increases faster than that of the previous model. The increase in mean energy for the $\hat{Y}$ coin has a linear form, while the $\hat{G}_H$ coin increases more quadratically. Note that quantum resonant AOKR walks possess a quadratic increase in mean energy, corresponding to a ballistic motion in momentum space. In the presence of a strong off-resonant β distribution like the residual thermal cloud from the original theory, the energy increases only linearly [101]. The data shown for a small number of up to 15 steps maximum show that the asymptotic regimes are rarely met. The experimentally obtained energy increases with more quadratic than linear behavior, which is more consistent with current theory and contradicts the presence of a thermal cloud as originally hypothesized. The comparison is yet more complicated since the experimental suffered from a series of well-known issues [27]. The effect most relevant in our context is the fading out of the ballistic peaks in the experimental momentum distributions due to atom number fluctuations and small atom losses. Each time slice is obtained from a new experimental run, and hence also the relative normalization of the atomic density might be an issue. All this may have consequences on the second moment of the distribution that is proportional to the energy plotted in Fig. 37 [14]. Counting less in the tails of the distribution typically leads to an underestimation of the mean energy [128]. The simulations in Fig. 35 [14] show that aside from the gradual loss in atoms at $\beta = 0.025$ the QWs are essentially equivalent. This then tells us that including the light shift into to QW is a good and more complete model to use in future experiments. We also wished to compare this model with the original explanation of the residual remaining atoms that were explained due to the thermal cloud from hotter atoms surrounding the BEC. This comparison is shown in Fig. 36 [14]. As we can see the predicted QWs differ dramatically and this thus shows that the light shift model is indeed more descriptive of the QW phenomena. This model also suggests methods as outlined above that can be used to obtain good experimental results and show that our QW utilizing the

AOKR is actually a good platform that can be used in further studying quantum information.

4.4 Topological phase transitions in a double-kicked quantum rotor

One future project that could utilize our setup is the possible detection of topological phase transitions in a double-kicked quantum rotor (DKQR) and detailed calculations and simulations have been carried out to study the possible outcomes of such experiments. The studies of such topological phases are of great interest as they have found many applications such as topological insulators [92, 58, 55, 72, 82]. The system under consideration as a candidate to experimentally realize topological phase transitions is a DKQR with internal spin-1/2 degree of freedom [135, 49]. The DKQR is a gapped Hamiltonian system characterized by an energy gap between the ground and first excited states. In this system a quantity known as the winding number[1] ν is topologically invariant under a wide range transformations[135]. The preservation of topological winding numbers requires preservation of chiral symmetry and the band gap [135, 49]. Permanently containing this chiral symmetry results in the topological invariant being able to change when the system is changed to a configuration in which the band gap closes. Such closure not only makes the phase undetermined but also allows for direct experimental control by scanning a system parameter. For the DKQR, the quasienergy spectrum is itself periodic and the gaps can be controlled by the driving parameters. The DKQR is based on the same AOKR described in section 2.2.3 in chapter 2 and is described by the Hamiltonian [15]

$$\hat{\mathcal{H}} = \frac{\hat{p} \otimes \mathbf{1}}{2} + k_1 \cos(\hat{\theta}) \otimes \hat{\sigma}_x \cdot \sum_{n=0}^{\infty} \delta(t - 2n\tau) + k_2 \sin(\hat{\theta}) \otimes \hat{\sigma}_y \cdot \sum_{n=0}^{\infty} \delta(t - (2n+1)\tau), \quad (4.4.1)$$

where $\hat{p}$ and $\hat{\theta}$ are the momentum and angular position operators, respectively, τ is the duration between two kicks of different kicking strengths k_1 and k_2, and the Pauli matrices $\hat{\sigma}_x$ and $\hat{\sigma}_y$ act on the internal spin-1/2 degree of freedom. The on-resonance condition where $\tau =$

[1] See the texts by Apostol and Courant for more about winding numbers from a mathematical standpoint [7, 25].

4π corresponds to a full revival at Talbot time. The resulting quasiperiodicity of the system can lead to a Hofstadter butterfly-like quasienergy spectrum and resolving a band structure rich in diplaying topological properties. The topological winding number is an abstract quantity and thus cannot often be measured directly. Instead, a separate quantity, the mean chiral displacement (MCD), is introduced as a measurable quantity in the experiment. In the DKQR the MCD describes the difference between momentum distributions of the two internal states that evolve under the operator $\hat{\mathcal{U}}$, is defined as [15]

$$\begin{aligned} C(t) &= \langle\psi_t|\hat{n}\otimes -\hat{\sigma}_z|\psi_t\rangle \\ &= \langle\psi_0|\hat{\mathcal{U}}^{-1}(\hat{n}\otimes -\hat{\sigma}_z)|\psi_0\rangle. \end{aligned} \tag{4.4.2}$$

The average of this MCD over several discrete steps t converges to half of the topological winding number ν [15]

$$\bar{C}(t) = \frac{1}{t}\sum_{t_i}^{t} \to \frac{\nu}{2}. \tag{4.4.3}$$

To measure the topological phase transitions, it is necessary to repeat the application of the sequence for a series of different configurations of k_1 and k_2 where the results of the experiment can be compared with the ideal data in the phase diagram as reported in Zhou *et. al.* [135]. The proposed sequence as optimized for the experiment reduces the number of operations necessary by making the $|2\rangle$ symmetric in momentum space to give the complete evolution $\hat{U}^t$ [15]

$$\begin{aligned} \hat{\mathcal{U}}^t = \hat{M}\left(\frac{-\pi}{2},\frac{\pi}{2}\right)\hat{K}_2^{1/2}\hat{M}\left(\frac{\pi}{2},\frac{\pi}{2}\right) \\ \cdot\left[\hat{M}\left(\frac{-\pi}{2},0\right)\hat{K}_1\hat{M}\left(\frac{-\pi}{2},\frac{\pi}{2}\right)\hat{M}\left(\frac{-\pi}{2},\frac{\pi}{2}\right)\hat{K}_2\hat{M}\left(\frac{\pi}{2},\frac{\pi}{2}\right)\right]^{t-1} \\ \times\hat{M}\left(\frac{-\pi}{2},0\right)\hat{K}_1\hat{M}\left(\frac{-\pi}{2},0\right)\hat{M}\left(\frac{-\pi}{2},\frac{\pi}{2}\right)\hat{K}_2^{1/2}\hat{M}\left(\frac{\pi}{2},\frac{\pi}{2}\right). \end{aligned} \tag{4.4.4}$$

The predicted momentum distributions after five applications of Eq. 4.4.4 is shown in Fig. 38 [15]. The stability of this proposed sequence was also considered in the simula-

tions. The unavoidable experimental limitations that were considered were the uncontrolled phases of the MW pulses, unwanted deviations from quantum resonance in the DKQR and the relative energy shift between the two internal states. This leads to a relative dynamical phase in the experiment that must be corrected. The phase noise was modeled as a random walk within an additional dynamical phase of the MW pulses. The results of this modeling are shown in Fig. 39 [15] Similar to QWs the light shift will also have to be taken into consideration in the experiments and properly compensated to detect the phase transitions. If this light-shift is not properly compensated then the topological phase will change and imply instabilities, making it impossible to distinguish between topological phase transitions and such instabilities. A proper compensation of this light shift using the same proposed techniques regarding QWs should increase the likelihood of successfully detecting phase transitions in the DKQR as shown in Fig. 40 [15].

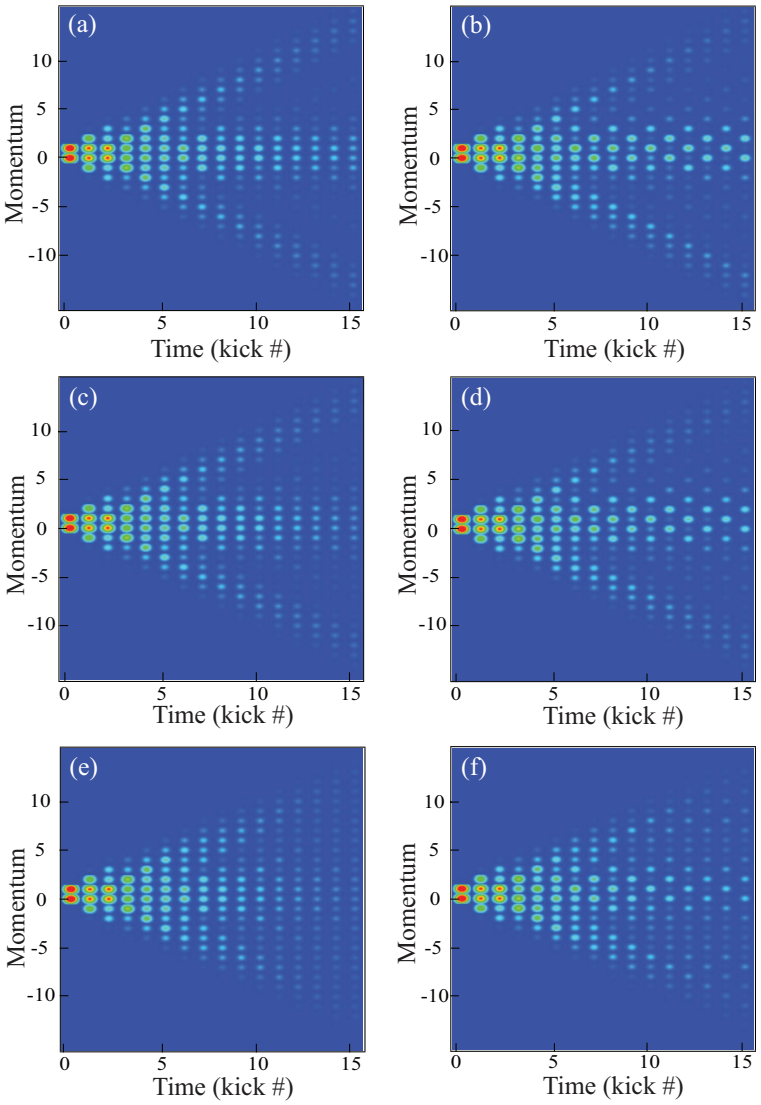

Figure 35: Numerical predictions of the QW up to 15 steps. Panels (a) and (b) were with $\beta = 0$. Panels (c) and (d) with $\beta = 0.01$. Panels (e) and (f) with $\beta = 0.025$. Note that the left hand panels were with a $\hat{W}$ coin and the right with a balancing phase. Adapted from [14]

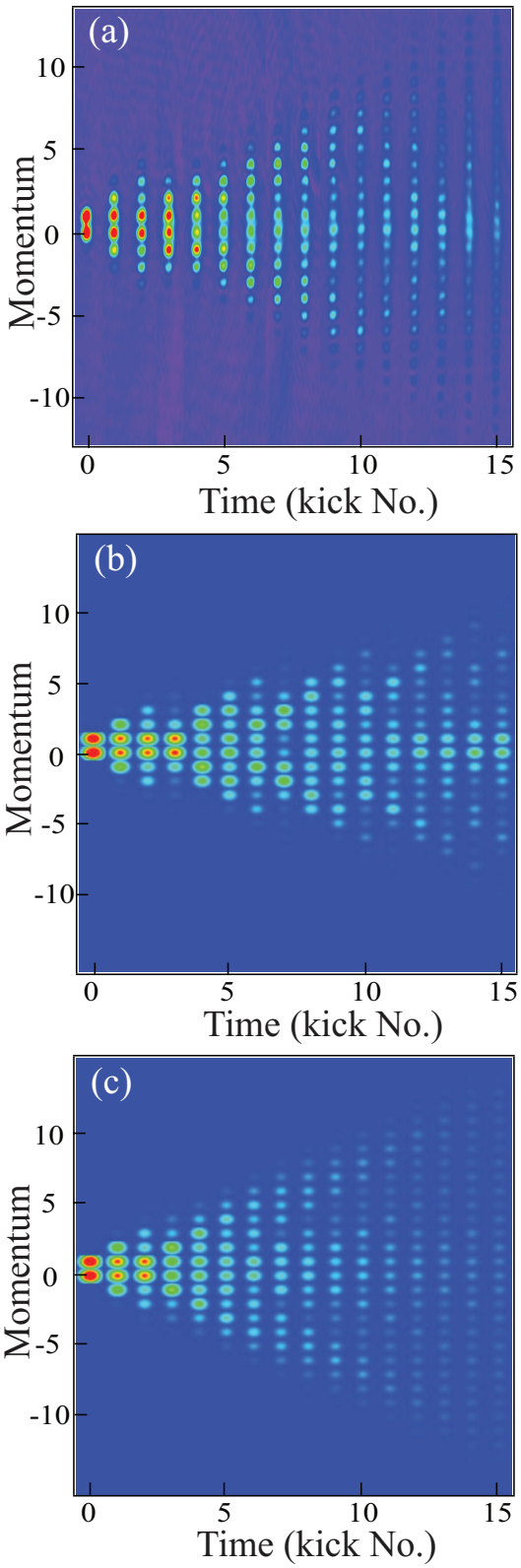

Figure 36: Numerical simulations of the QW with panel (a) with a gate coin and panel (b) showing the QW with original thermal cloud model.

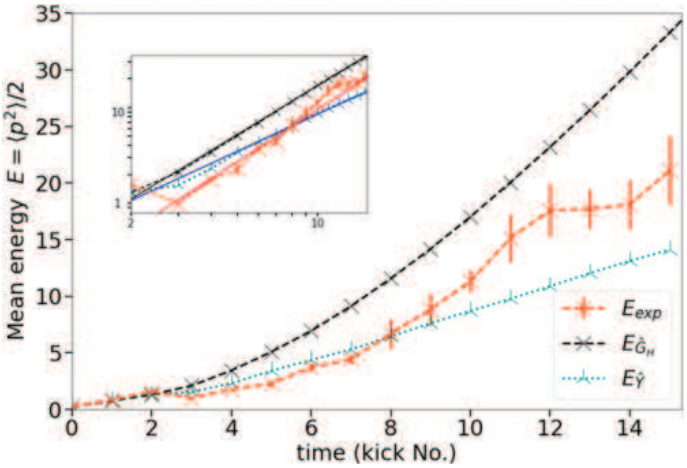

Figure 37: Comparison of mean energies calculated from the walks in Fig. 36 with $\beta_{FWHM} = 0.025$. The inset plots the energies on a double logarithmic scale where the power-law exponents extracted from the fits (solid lines). Giving $1.8 \pm 0.2 (E_{exp})$, 1.7 ± 0.1 $(E_{\hat{G}_H})$, and 1.3 ± 0.1 $(E_{\hat{Y}})$ for the experimental and theoretical data respectively. Notice that the apparent better agreement between E_{exp} and $E_{\hat{G}_H}$ confirms the better scaling of the model. Also, note that the asymptotic exponent of 2 expected for a ballistic walk is hardly approached for QWs with only 15 steps. Adapted from [14].

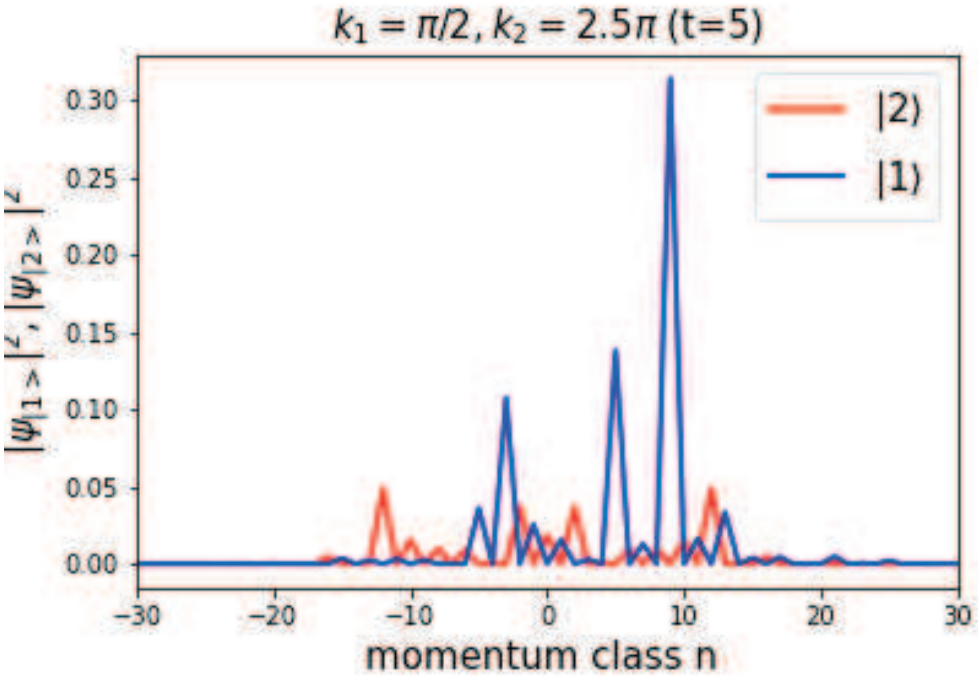

Figure 38: Predicted momentum distributions after 5 applications of the proposed sequence Eq. 4.4.4. Note that the $|2\rangle$ state is symmetric in momentum space. Adapted from [15].

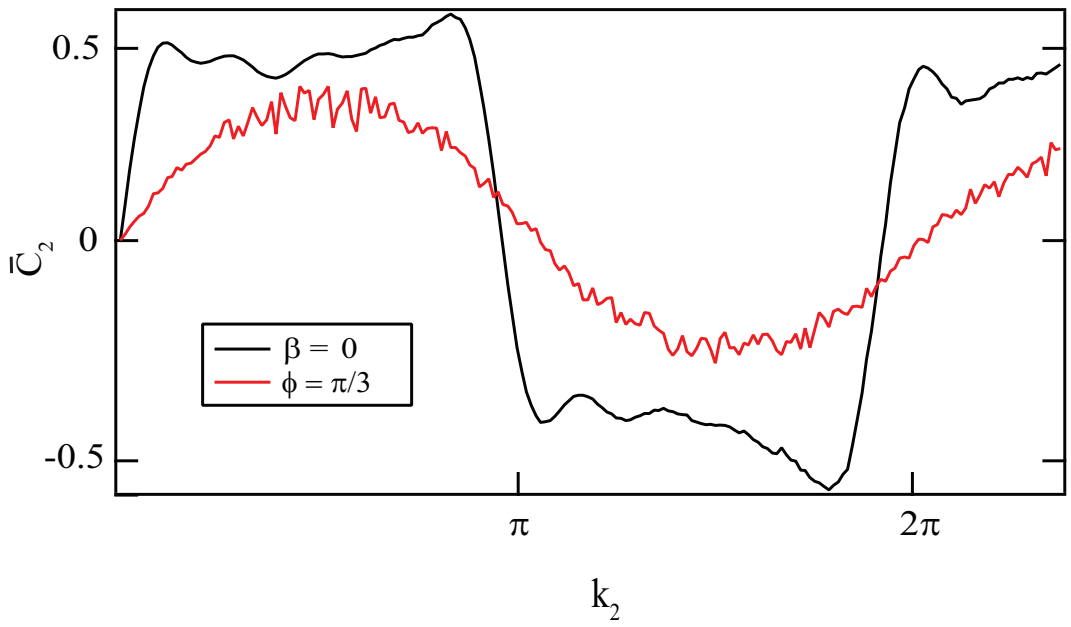

Figure 39: Predicted topological phase diagram with dynamical phase transitions. The black curve represents the predicted ideal MCD topological phase diagram. The red curve represents a phase noise of $\phi = \pi/3$. For both curves $\beta = 0$ (Adapted from [15])

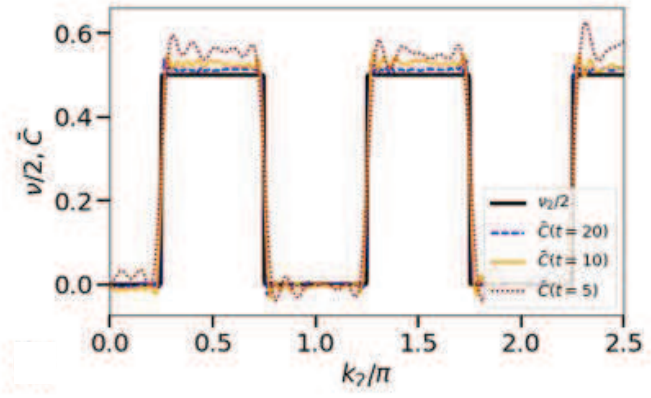

Figure 40: Averaged MCD plotted as a function of step number t scanning the kicking strength k_2. Note that the averaged MCD converges to the predicted phase transitions (black curve) as the number of steps t increases. Adapted from [15].

CHAPTER V

CONCLUSION

We have studied the possibility of utilizing the discrete quantum walk of a ^{87}Rb BEC in momentum space based on the use of an AOKR for various possible applications such as quantum search algorithms, and quantum computing. The main focus was to find out how robust the walk would be when subjected to external sources of spontaneous emission that could have negative effects on the system.

This was first attempted by using the two counter-propagating beams that generate the AOKR pulses by creating an intensity imbalance that in turn creates an increase of the background laser radiation that should increase the probability of an SE event. Multiple experimental runs were attempted with this in mind by changing the applied amplitude while also maintaining the proper kick strength. The results of this failed to show significant atomic losses as well as any transition towards classical behavior within the capabilities of our experimental apparatus. As a result, a solution was found in the possibility of using the imaging beam on resonance with the $|F = 2\rangle$ to $|F' = 3\rangle$ transition as it had the advantages of being easily tunable and well controlled in intensity and duration. Using this, several experiments were conducted testing different pulse parameters until a suitable method was found to induce controllable SE probabilities. It was found that quantum walks at less than five steps were very robust under even high SE pulse intensities in that they maintained their quantum behavior. It was also shown that the imaging light causes a notable shift in the momentum distribution towards positive momenta states of the quantum walks regardless of compensation confirming a theoretical prediction that SE causes an imbalance of internal

states of the atoms towards the $|2\rangle$ state because projection of this state moves towards positive momentum.

The quantum-to-classical transition behavior was also observed with increasing SE probability rate. This was done by measuring the mean energy over eight steps with increasing SE probability and the results fitted to obtain a quantity R. This rate was shown to be higher with lower SE probabilities which was also shown to be in good agreement with theoretical predictions. These results show that it is possible to quantitatively measure the quantum-to-classical behavior. This also showed that SE is a weak form of quantum measurement in which many such events necessarily will have a larger effect as this causes a bias of the walk.

We also presented more theoretical results by revisiting the original QW data and exploring a more complete theoretical model that explains the noticeable central cloud region as being more due to the light shift from AC-Stark shift rather than a cloud of atoms possessing higher energy. This theory also presented some possible mitigation techniques that could be readily applied in an experiment by increasing the number of initial states to be used in the ratchet as well as an exchange of coin and gate operators to further reduce the phase offset. Both of these techniques can potentially greatly reduce the time consuming trial and error method of phase compensation.

All of these results tell us that the AOKR based QW is reliable and robust to external perturbations at up to about 15 steps and with some modifications can be refined to more closely resemble ideal QW behavior. Future experiments with quantum search algorithms and topological phenomena should be relatively feasible in ^{87}Rb BEC systems. Recent theoretical investigations indicate that such topology experiments are feasible after considering the light shift, spontaneous emission, and relative phase typical for our system. In such an experiment, a double kicked quantum rotor (DKQR) is applied where two kicks of differing strengths are applied within a single Talbot time period. Between each kick multiple microwave pulses are applied for multiple rotations to observe the topological phase transitions in the mean chiral displacement. It is predicted that if the phase noise is kept to a minimum

and the light-shift is compensated such a DKQR could be used successfully to observe such transitions. The possible results of this experiment could provide an alternative method to predict the behavior of special materials that are studied in condensed matter physics such as topological insulators. Such an experiment further illustrates the exciting possibilities of this still new and rapidly growing field of quantum information.

REFERENCES

[1] Girish S Agarwal and Pradyumna K Pathak, *Quantum random walk of the field in an externally driven cavity*, Physical Review A **72** (2005), no. 3, 033815.

[2] Yakir Aharonov, Luiz Davidovich, and Nicim Zagury, *Quantum random walks*, Physical Review A **48** (1993), no. 2, 1687.

[3] Leslie Allen and Joseph H Eberly, *Optical resonance and two-level atoms*, vol. 28, Courier Corporation, 1987.

[4] Marcelo Alonso and Edward J Finn, *Fundamental university physics. vol. 3: Quantum and statistical physics*, (1968).

[5] H Ammann, R Gray, I Shvarchuck, and N Christensen, *Quantum delta-kicked rotor: Experimental observation of decoherence*, Physical review letters **80** (1998), no. 19, 4111.

[6] Mike H Anderson, Jason R Ensher, Michael R Matthews, Carl E Wieman, and Eric A Cornell, *Observation of bose-einstein condensation in a dilute atomic vapor*, science **269** (1995), no. 5221, 198–201.

[7] TM Apostol, *Mathematical analysis. reading*, 1957.

[8] Arthur Ashkin, James M Dziedzic, John E Bjorkholm, and Steven Chu, *Observation of a single-beam gradient force optical trap for dielectric particles*, Optics letters **11** (1986), no. 5, 288–290.

[9] Ghazal Behinaein, Vijayashankar Ramareddy, Peyman Ahmadi, and Gil S Summy, *Exploring the phase space of the quantum δ-kicked accelerator*, Physical review letters **97** (2006), no. 24, 244101.

[10] Peter F Bernath, *Spectra of atoms and molecules*, Oxford university press, 2020.

[11] Ethan Bernstein and Umesh Vazirani, *Quantum complexity theory*, SIAM Journal on computing **26** (1997), no. 5, 1411–1473.

[12] Nabhendra Bisnik and Alhussein Abouzeid, *Modeling and analysis of random walk search algorithms in p2p networks*, Second International Workshop on Hot Topics in Peer-to-Peer Systems, IEEE, 2005, pp. 95–103.

[13] Felix Bloch, *Nuclear induction*, Physical review **70** (1946), no. 7-8, 460.

[14] Nikolai Bolik, Caspar Groiseau, Jerry H. Clark, Alexander Gresch, Siamak Dadras, Gil S. Summy, Yingmei Liu, and Sandro Wimberger, *Light-shift-induced behaviors observed in momentum-space quantum walks*, Phys. Rev. A **106** (2022), 033307.

[15] Nikolai Bolik, Caspar Groiseau, Jerry H. Clark, Gil S. Summy, Yingmei Liu, and Sandro Wimberger, *Detecting topological phase transitions in a double kicked quantum rotor*, Phys. Rev. A **106** (2022), 043318.

[16] AM Bonch-Bruevich, NN Kostin, VA Khodovoi, and VV Khromov, *Changes in the atomic absorption spectrum in the field of a light wave i*, Sov. Phys. JETP **29** (1969), no. 1, 82–85.

[17] Brian Harold Bransden and Charles Jean Joachain, *Physics of atoms and molecules*, Pearson Education India, 2003.

[18] M Brune, JM Raimond, P Goy, L Davidovich, and S Haroche, *Realization of a two-photon maser oscillator*, Physical review letters **59** (1987), no. 17, 1899.

[19] Eugene Butkov, *Mathematical physics*, Addison-Wesley, 1968.

[20] GW Castellan, *Physical chemistry*, (1971).

[21] C Madaiah Chandrashekar, *Implementing the one-dimensional quantum (hadamard) walk using a bose-einstein condensate*, Physical Review A **74** (2006), no. 3, 032307.

[22] Boris V Chirikov, *A universal instability of many-dimensional oscillator systems*, Physics reports **52** (1979), no. 5, 263–379.

[23] Steven Chu, *Nobel lecture: The manipulation of neutral particles*, Reviews of Modern Physics **70** (1998), no. 3, 685.

[24] JH Clark, C Groiseau, ZN Shaw, S Dadras, C Binegar, S Wimberger, GS Summy, and Y Liu, *Quantum to classical walk transitions tuned by spontaneous emissions*, Physical Review Research **3** (2021), no. 4, 043062.

[25] Richard Courant, *Differential and integral calculus, volume 2*, vol. 2, John Wiley & Sons, 2011.

[26] Siamak Dadras, *Discrete-time quantum walk of a bose-einstein condensate in momentum space*, Ph.D. thesis, Ph. D. thesis, Oklahoma State University, 2018.

[27] Siamak Dadras, Alexander Gresch, Caspar Groiseau, Sandro Wimberger, and Gil S Summy, *Quantum walk in momentum space with a bose-einstein condensate*, Physical review letters **121** (2018), no. 7, 070402.

[28] Jean Dalibard and Claude Cohen-Tannoudji, *Laser cooling below the doppler limit by polarization gradients: simple theoretical models*, JOSA B **6** (1989), no. 11, 2023–2045.

[29] Itzhack Dana, Vijayashankar Ramareddy, Ishan Talukdar, and Gil S Summy, *Experimental realization of quantum-resonance ratchets at arbitrary quasimomenta*, Physical review letters **100** (2008), no. 2, 024103.

[30] Kendall B Davis, M-O Mewes, Michael R Andrews, Nicolaas J van Druten, Dallin S Durfee, DM Kurn, and Wolfgang Ketterle, *Bose-einstein condensation in a gas of sodium atoms*, Physical review letters **75** (1995), no. 22, 3969.

[31] Kendall B Davis, M-O Mewes, and Wolfgang Ketterle, *An analytical model for evaporative cooling of atoms*, Applied Physics B **60** (1995), no. 2, 155–159.

[32] Nikolai Borisovich Delone and Vladimir P Krainov, *Ac stark shift of atomic energy levels*, Physics-Uspekhi **42** (1999), no. 7, 669.

[33] Wolfgang Demtröder, *Laser spectroscopy 2: experimental techniques*, Springer, 2015.

[34] Andrei Derevianko and Hidetoshi Katori, *Colloquium: Physics of optical lattice clocks*, Reviews of Modern Physics **83** (2011), no. 2, 331.

[35] Bipin R. Desai, *Quantum mechanics with basic field theory*, 2009.

[36] Elizabeth A Donley, Thomas P Heavner, Filippo Levi, MO Tataw, and Steven R Jefferts, *Double-pass acousto-optic modulator system*, Review of Scientific Instruments **76** (2005), no. 6, 063112.

[37] Liwei Duan, *Quantum walk on the bloch sphere*, Physical Review A **105** (2022), no. 4, 042215.

[38] Richard P Feynman, Frank L Vernon Jr, and Robert W Hellwarth, *Geometrical representation of the schrödinger equation for solving maser problems*, Journal of applied physics **28** (1957), no. 1, 49–52.

[39] Conor Finn, *Chaotic control theory applied to the chirikov standard map*, University of Warwick, 2012.

[40] Shmuel Fishman, DR Grempel, and RE Prange, *Chaos, quantum recurrences, and anderson localization*, Physical Review Letters **49** (1982), no. 8, 509.

[41] G. Floquet, *Sur les équations différentielles linéaires à coefficients périodiques*, Ann. de l'Ecole Norm. Sup. (2) **12** (1883), 47–88.

[42] Christopher J Foot, *Atomic physics*, vol. 7, OUP Oxford, 2004.

[43] Mark Fox, *A student's guide to atomic physics*, Cambridge University Press, 2018.

[44] David Judson Gary, *Exploration of photon echo in a bose-einstein condensate*, Ph.D. thesis, Oklahoma State University, 2019.

[45] R Gommers, S Denisov, and F Renzoni, *Quasiperiodically driven ratchets for cold atoms*, Physical review letters **96** (2006), no. 24, 240604.

[46] Phillip L Gould, George A Ruff, and David E Pritchard, *Diffraction of atoms by light: The near-resonant kapitza-dirac effect*, Physical review letters **56** (1986), no. 8, 827.

[47] David J Griffiths and Darrell F Schroeter, *Introduction to quantum mechanics*, Cambridge university press, 2018.

[48] C Groiseau, *Discrete-time quantum walks in momentum space*, Ph.D. thesis, 2017.

[49] Caspar Groiseau, Alexander Wagner, Gil S Summy, and Sandro Wimberger, *Impact of lattice vibrations on the dynamics of a spinor atom-optics kicked rotor*, Condensed Matter **4** (2019), no. 1, 10.

[50] Caspar Groiseau and Sandro Wimberger, *Spontaneous emission in quantum walks of a kicked bose-einstein condensate*, Physical Review A **99** (2019), no. 1, 013610.

[51] Lov K Grover, *A fast quantum mechanical algorithm for estimating the median*, arXiv preprint quant-ph/9607024 (1996).

[52] ———, *Quantum mechanics helps in searching for a needle in a haystack*, Physical review letters **79** (1997), no. 2, 325.

[53] Theodor W Hänsch and Arthur L Schawlow, *Cooling of gases by laser radiation*, Optics Communications **13** (1975), no. 1, 68–69.

[54] Walter A. Harrison, *Solid state theory*, McGraw-Hill, 1970, International Series in Pure and Applied Physics.

[55] M Zahid Hasan and Charles L Kane, *Colloquium: topological insulators*, Reviews of modern physics **82** (2010), no. 4, 3045.

[56] Harald F Hess, *Evaporative cooling of magnetically trapped and compressed spin-polarized hydrogen*, Physical Review B **34** (1986), no. 5, 3476.

[57] Terrell L Hill, *An introduction to statistical thermodynamics*, Courier Corporation, 1986.

[58] Derek YH Ho and Jiangbin Gong, *Topological effects in chiral symmetric driven systems*, Physical Review B **90** (2014), no. 19, 195419.

[59] Felix M Izrailev, *Simple models of quantum chaos: Spectrum and eigenfunctions*, Physics Reports **196** (1990), no. 5-6, 299–392.

[60] Max Jammer, *The conceptual development of quantum mechanics*, McGraw-Hill, 1966.

[61] Wilfred Kaplan, *Operational methods for linear systems*, Addison-Wesley Publishing Company, 1962.

[62] Michal Karski, Leonid Förster, Jai-Min Choi, Andreas Steffen, Wolfgang Alt, Dieter Meschede, and Artur Widera, *Quantum walk in position space with single optically trapped atoms*, Science **325** (2009), no. 5937, 174–177.

[63] Julia Kempe, *Quantum random walks: an introductory overview*, Contemporary Physics **44** (2003), no. 4, 307–327.

[64] ———, *Discrete quantum walks hit exponentially faster*, Probability theory and related fields **133** (2005), no. 2, 215–235.

[65] Anatole Kenfack, *Gravity effect on quantum resonance ratchet transport of cold atoms*, Physical Review A **104** (2021), no. 3, 033321.

[66] Johannes Kepler, *De cometis libelli tres i. astronomicus, theoremata continens de novam... iii. astrologicus, de significationibus cometarum annorum motu cometarum... ii. physicus, continens physiologiam cometarum 1607 et 1618*, De cometis libelli tres I. astronomicus.

[67] Wolfgang Ketterle, Kendall B Davis, Michael A Joffe, Alex Martin, and David E Pritchard, *High densities of cold atoms in a dark spontaneous-force optical trap*, Physical review letters **70** (1993), no. 15, 2253.

[68] Takuya Kitagawa, *Topological phenomena in quantum walks: elementary introduction to the physics of topological phases*, Quantum Information Processing **11** (2012), no. 5, 1107–1148.

[69] Bruce G Klappauf, Windell H Oskay, Daniel A Steck, and Mark G Raizen, *Observation of noise and dissipation effects on dynamical localization*, Physical review letters **81** (1998), no. 6, 1203.

[70] Morris Kline, *Mathematical thought from ancient to modern times*, Oxford, 1972.

[71] Frank B Knight, *On the random walk and brownian motion*, Transactions of the American Mathematical Society **103** (1962), no. 2, 218–228.

[72] John Michael Kosterlitz and David James Thouless, *Ordering, metastability and phase transitions in two-dimensional systems*, Journal of Physics C: Solid State Physics **6** (1973), no. 7, 1181.

[73] Stefan Kuhr, *A controlled quantum system of individual neutral atoms*, (2003).

[74] SJM Kuppens, KL Corwin, KW Miller, TE Chupp, and CE Wieman, *Loading an optical dipole trap*, Physical review A **62** (2000), no. 1, 013406.

[75] Peter Lebedew, *Untersuchungen über die druckkräfte des lichtes*, Annalen der Physik **311** (1901), no. 11, 433–458.

[76] Paul D Lett, Richard N Watts, Christoph I Westbrook, William D Phillips, Phillip L Gould, and Harold J Metcalf, *Observation of atoms laser cooled below the doppler limit*, Physical review letters **61** (1988), no. 2, 169.

[77] Frédéric Magniez, Ashwin Nayak, Peter C Richter, and Miklos Santha, *On the hitting times of quantum versus random walks*, Algorithmica **63** (2012), no. 1, 91–116.

[78] Wilhelm Magnus and Stanley Winkler, *Hill's equation*, Courier Corporation, 2013.

[79] Peter J Martin, Phillip L Gould, Bruce G Oldaker, Andrew H Miklich, and David E Pritchard, *Diffraction of atoms moving through a standing light wave*, Physical Review A **36** (1987), no. 5, 2495.

[80] John Mcgervey, *Introduction to modern physics*, Elsevier, 2012.

[81] Donald Allan McQuarrie, *Mathematical methods for scientists and engineers*, University science books, 2003.

[82] N David Mermin, *The topological theory of defects in ordered media*, Reviews of Modern Physics **51** (1979), no. 3, 591.

[83] D Meschede, Herbert Walther, and G Müller, *One-atom maser*, Physical review letters **54** (1985), no. 6, 551.

[84] Harold J Metcalf, *Pv d. straten, laser cooling and trapping*, 1999.

[85] Jiating Ni, *State dependance of quantum ratchets*, Ph.D. thesis, Oklahoma State University, 2017.

[86] Jiating Ni, Siamak Dadras, Wa Kun Lam, Rajendra K Shrestha, Mark Sadgrove, Sandro Wimberger, and Gil S Summy, *Hamiltonian ratchets with ultra-cold atoms*, Annalen der Physik **529** (2017), no. 8, 1600335.

[87] Jiating Ni, Wa Kun Lam, Siamak Dadras, Mario F Borunda, Sandro Wimberger, and Gil S Summy, *Initial-state dependence of a quantum resonance ratchet*, Physical Review A **94** (2016), no. 4, 043620.

[88] William D Phillips, *Nobel lecture: Laser cooling and trapping of neutral atoms*, Reviews of Modern Physics **70** (1998), no. 3, 721.

[89] William D Phillips and Harold Metcalf, *Laser deceleration of an atomic beam*, Physical Review Letters **48** (1982), no. 9, 596.

[90] Renato Portugal, *Quantum walks and search algorithms*, vol. 19, Springer, 2013.

[91] Warat Puengtambol, Prapong Prechaprapranwong, and Unchalisa Taetragool, *Implementation of quantum random walk on a real quantum computer*, Journal of Physics: Conference Series, vol. 1719, IOP Publishing, 2021, p. 012103.

[92] Xiao-Liang Qi and Shou-Cheng Zhang, *Topological insulators and superconductors*, Reviews of Modern Physics **83** (2011), no. 4, 1057.

[93] Eric L Raab, Mara Prentiss, Alex Cable, Steven Chu, and David E Pritchard, *Trapping of neutral sodium atoms with radiation pressure*, Physical review letters **59** (1987), no. 23, 2631.

[94] Mark G Raizen, *Quantum chaos with cold atoms*, Advances in Atomic, Molecular, and Optical Physics **41** (1999), no. 43, 199.

[95] MG Raizen, FL Moore, JC Robinson, CF Bharucha, and Bala Sundaram, *An experimental realization of the quantum-kicked rotor*, Quantum and Semiclassical Optics: Journal of the European Optical Society Part B **8** (1996), no. 3, 687.

[96] Frederick Reif, *Fundamentals of statistical and thermal physics*, Waveland Press, 2009.

[97] Kennard E. H. Richtmyer F.K. and Cooper John N., *Introduction to modern physics*, McGraw-Hill, 1969.

[98] Donald Rogers, *Einstein's other theory: the planck-bose-einstein theory of heat capacity*, Princeton University Press, 2005.

[99] Mark Sadgrove, Munekazu Horikoshi, Tetsuo Sekimura, and Ken'ichi Nakagawa, *Rectified momentum transport for a kicked bose-einstein condensate*, Physical review letters **99** (2007), no. 4, 043002.

[100] Mark Sadgrove, Terry Mullins, Scott Parkins, and Rainer Leonhardt, *The effect of amplitude noise on the quantum and diffusion resonances of the atom optics kicked rotor*, Physica E: Low-dimensional Systems and Nanostructures **29** (2005), no. 1-2, 369–374.

[101] Mark Sadgrove and Sandro Wimberger, *A pseudoclassical method for the atom-optics kicked rotor: from theory to experiment and back*, Advances in Atomic, Molecular, and Optical Physics, vol. 60, Elsevier, 2011, pp. 315–369.

[102] MS Santhanam, Sanku Paul, and J Bharathi Kannan, *Quantum kicked rotor and its variants: Chaos, localization and beyond*, Physics Reports **956** (2022), 1–87.

[103] Leonard I. Schiff, *Quantum mechanics*, McGraw-Hill, 1968.

[104] Hector Schmitz, Robert Matjeschk, Ch Schneider, Jan Glueckert, Martin Enderlein, Thomas Huber, and Tobias Schaetz, *Quantum walk of a trapped ion in phase space*, Physical review letters **103** (2009), no. 9, 090504.

[105] Florian Schreck and Klaasjan van Druten, *Laser cooling for quantum gases*, Nature Physics **17** (2021), no. 12, 1296–1304.

[106] Jon H Shirley, *Interaction of a quantum system with a strong oscillating field*, Ph.D. thesis, California Institute of Technology, 1963.

[107] Peter W Shor, *Algorithms for quantum computation: discrete logarithms and factoring*, Proceedings 35th annual symposium on foundations of computer science, Ieee, 1994, pp. 124–134.

[108] Rajendra Kumar Shrestha, *Applications of the atom-optical kicked rotor*, Oklahoma State University, 2013.

[109] RK Shrestha, J Ni, WK Lam, GS Summy, and S Wimberger, *Dynamical tunneling of a bose-einstein condensate in periodically driven systems*, Physical Review E **88** (2013), no. 3, 034901.

[110] RK Shrestha, J Ni, WK Lam, S Wimberger, and GS Summy, *Controlling the momentum current of an off-resonant ratchet*, Physical Review A **86** (2012), no. 4, 043617.

[111] RK Shrestha, S Wimberger, J Ni, WK Lam, and GS Summy, *Fidelity of the quantum δ-kicked accelerator*, Physical Review E **87** (2013), no. 2, 020902.

[112] Anthony E Siegman, *Lasers*, University science books, 1986.

[113] Joseph W. Simmons and Mark J. Guttmann, *States, waves and photons: A modern introduction to light*, Addison-Wesley, 1970.

[114] Johannes Stark, *Beobachtungen über den effekt des elektrischen feldes auf spektrallinien. i. quereffekt*, Annalen der Physik **348** (1914), no. 7, 965–982.

[115] Daniel A Steck, *Rubidium 87 d line data*, (2001).

[116] Francis Su, *Convergence of random walks on the circle generated by an irrational rotation*, Transactions of the American Mathematical Society **350** (1998), no. 9, 3717–3741.

[117] Gil Summy and Sandro Wimberger, *Quantum random walk of a bose-einstein condensate in momentum space*, Physical Review A **93** (2016), no. 2, 023638.

[118] Robert Swendsen, *An introduction to statistical mechanics and thermodynamics*, Oxford University Press, USA, 2020.

[119] Henry Fox Talbot, *Lxxvi. facts relating to optical science. no. iv*, The London, Edinburgh, and Dublin Philosophical Magazine and Journal of Science **9** (1836), no. 56, 401–407.

[120] Ishan Talukdar, Rajendra Shrestha, and GS Summy, *Sub-fourier characteristics of a δ-kicked-rotor resonance*, Physical review letters **105** (2010), no. 5, 054103.

[121] Ben C Travaglione and Gerald J Milburn, *Implementing the quantum random walk*, Physical Review A **65** (2002), no. 3, 032310.

[122] Maimaitiyiming Tusun, Yang Wu, Wenquan Liu, Xing Rong, and Jiangfeng Du, *Experimental implementation of a continuous-time quantum random walk on a solid-state quantum information processor*, Chinese Physics B **28** (2019), no. 11, 110302.

[123] Alban Urvoy, Zachary Vendeiro, Joshua Ramette, Albert Adiyatullin, and Vladan Vuletić, *Direct laser cooling to bose-einstein condensation in a dipole trap*, Physical review letters **122** (2019), no. 20, 203202.

[124] Martin Varbanov, Hari Krovi, and Todd A Brun, *Hitting time for the continuous quantum walk*, Physical Review A **78** (2008), no. 2, 022324.

[125] Jingbo Wang and Kia Manouchehri, *Physical implementation of quantum walks*, Springer, 2013.

[126] Kunkun Wang, Yuhao Shi, Lei Xiao, Jingbo Wang, Yogesh N Joglekar, and Peng Xue, *Experimental realization of continuous-time quantum walks on directed graphs and their application in pagerank*, Optica **7** (2020), no. 11, 1524–1530.

[127] Amir Waxman, *Coherent manipulations of the rubidium atom ground state*, Ben Gurion University, 2008.

[128] Sandro Wimberger, Italo Guarneri, and Shmuel Fishman, *Quantum resonances and decoherence for δ-kicked atoms*, Nonlinearity **16** (2003), no. 4, 1381.

[129] David J Wineland, Carl E Wieman, and Stephen Judson Smith, *Atomic physics 14: Fourteenth international conference on atomic physics*, American Institute of Physics Conference Series, vol. 323, 1994.

[130] DJ Wineland and H Dehmelt, *Proposed $1014\delta\nu/\nu$ laser fluorescence spectroscopy on tl+ mono-ion oscillator iii (side band cooling)*, Bull. Am. Phys. Soc **20** (1975), no. 4, 637–637.

[131] Jizhou Wu, Wei-Wei Zhang, and Barry C Sanders, *Topological quantum walks: Theory and experiments*, Frontiers of Physics **14** (2019), no. 6, 1–6.

[132] Feng Xia, Jiaying Liu, Hansong Nie, Yonghao Fu, Liangtian Wan, and Xiangjie Kong, *Random walks: A review of algorithms and applications*, IEEE Transactions on Emerging Topics in Computational Intelligence **4** (2019), no. 2, 95–107.

[133] Dizhou Xie, Tian-Shu Deng, Teng Xiao, Wei Gou, Tao Chen, Wei Yi, and Bo Yan, *Topological quantum walks in momentum space with a bose-einstein condensate*, Physical Review Letters **124** (2020), no. 5, 050502.

[134] Mannucci M. A. Yanofsky N. S., *Quantum computing for computer scientists*, 2008.

[135] Longwen Zhou and Jiangbin Gong, *Floquet topological phases in a spin-1/2 double kicked rotor*, Physical Review A **97** (2018), no. 6, 063603.

APPENDIX A

In this appendix I discuss the theory of laser cooling and trapping which is crucial to realize a Bose-Einstein Condensate (BEC).

To create BECs one must first cool atoms down to the critical temperature and to achieve the necessary phase space density. One of these critical steps is the creation of a Magnetic-Optical Trap (MOT) which cools a sample of atoms down to $10^{-6}K$ and a speed of $\approx$ 10 cm s^{-1}. The realization of a MOT is itself dependent upon the technique and theory of laser cooling. In this chapter I will summarize and derive those parts of laser cooling theory that are necessary for our system.

Photon Recoil and Bloch Equations

Introduction

To realize a BEC one must take a gas of atoms at room temperature (25° C or 298.15 K) where the average speed[1] is $\approx$ 671.331 m/s and cool them down to around 170 nK with a speed of just a few thousands of μm/s. Such a difference represents a nearly 10^6 factor in reduction of speed and also shows the challenges that were present in realizing a BEC and lead to a series of Nobel Prizes for the scientists for the various crucial steps to this goal. Although it had been speculated by Kepler [66] regarding comet tails pointing away from the sun and experimentally known since the early twentieth century that electromagnetic radiation exerts a force on matter [75], it was only in the 1970s after advent of lasers did the

[1]For nitrogen (N_2) at $T = 298.15K$, the average speed $\bar{c}$, is given by $\bar{c} = \sqrt{\frac{8k_BT}{\pi m}}$ where $k_B = 1.380 \cdot 10^{-23}$ is the Boltzmann constant. This average speed formula is derived in any text on statistical thermodynamics or physical chemistry[20].

idea of using light to decrease the momentum of atoms [130, 53, 88] suggest the feasibility of directly cooling a gas of neutral atoms. Shortly afterwards, W. D. Phillips demonstrated that on resonance laser light could deflect a beam of neutral sodium atoms [89] leading to further advances in laser cooling.

The general idea behind laser cooling is quite simple as it involves using laser light to slow down a moving atom in a gas. This occurs because the photons in the laser light has lower energy than the moving atom and when the photon bounces off of the atom energy is transferred and the atom slows down. This laser cooling was first demonstrated by Steven Chu in 1986 [8, 93] who also received the Nobel Prize in Physics in 1997 for this work [23].

Because individual photons possess a very small amount of energy, the use of photons to slow an atom down from the hundreds of meters per second down to tenths of meter per second is similar to using a ping-pong ball to slow down a train. However, in theory it is possible to change the speed and direction of such a train if enough ping-pong balls are used. In a similar manner we can use photons to kick atoms in the opposite direction of the photon before it is absorbed by the atom. However, only photons of a certain frequency are able to do this as we will see.

Basics of Photon Recoil

Here we outline the basic idea of photon recoil that forms the basis of laser cooling as detailed in Refs. [33, 42]. If we consider an atom of rest mass m_0 possessing an energy E_i, initial velocity $\mathbf{v}_i$ and momentum $\mathbf{p}_i = m_0\mathbf{v}_i$. If this atom is then subject to a photon of energy $\hbar\omega_{ik} = E_k - E_i$ and momentum $\hbar\mathbf{k}$ it will be excited to the state E_k. As a result, the atom then has a momentum change of $p_k = p_i + \hbar k$. Now, consider the relativistic momentum of the photon in terms of the two levels given in Eq. A.1 [33]

$$\hbar\omega_{ik} = \sqrt{p_k^2c^2 + (m_0c^2 + E_k)^2} - \sqrt{p_i^2c^2 + (m_0c^2 + E_i)^2}. \tag{A.1}$$

Expanding Eq. A.1 as a Taylor series we obtain Eq. A.2[33]

$$\omega_{ik} = \omega_0 + \boldsymbol{k} \cdot \boldsymbol{v}_i - \omega_0 \frac{v_i^2}{2c^2} + \frac{\hbar\omega_0^2}{2m_0c^2} + \cdots . \tag{A.2}$$

The first term in this series is the frequency $\omega_0 = E_k - E_i$ is the absorption frequency. The second and third terms are the linear and quadratic Doppler terms respectively. The fourth term here represents the photon recoil energy due to conservation of momentum. Combining this with a similar result for emission gives us the resulting relative frequency shift [33]

$$\Delta\omega = \frac{\hbar\omega_0^2}{m_0c^2}. \tag{A.3}$$

These results show us that a laser beam of a certain[33] frequency can cause an atom experience a change in energy through photon recoil and thus could indeed be slowed down in velocity. The theory behind such a procedure can be found in the optical Bloch equations which we will outline next.

Bloch Equations

Now that we have some idea of how photons can cause a change in the momentum and energy of an atom we can now derive the optical Bloch equations necessary to understand the creation of the Magnetic Optical Trap (MOT). If we consider the force from light applied to an atom we express this as the expectation value of the force operator in quantum mechanics [84] in Eq. A.4

$$\hat{F} = \langle \mathcal{F} \rangle = \frac{d}{dt}\langle p \rangle. \tag{A.4}$$

Because this is a time varying operator the time derivative of such an operator is given by [17] Eq. A.5

$$\frac{d}{dt}\langle A \rangle = \frac{i}{\hbar}\langle [\mathcal{H}, \mathcal{A}] \rangle. \tag{A.5}$$

Applying Eq. A.5 to the momentum, p, we have Eq. A.6 where $p = -i\hbar\frac{\partial \mathcal{H}}{\partial z}$

$$[\mathcal{H}, p] = i\hbar\frac{\partial \mathcal{H}}{\partial z}. \tag{A.6}$$

From this we can now write [84] the force on the atom as in Eq. A.7

$$F = -\left\langle \frac{\partial \mathcal{H}}{\partial z} \right\rangle = -\nabla\mathcal{H}. \tag{A.7}$$

Now noting that the total Hamiltonian is given by $\mathcal{H} = H_0 + H'(t)$, where H_0 and $H'(t)$ are the time-independent and time-dependent Hamiltonians respectively, we write the expectation value of Eq. A.7 as given by Eq. A.8 where ρ is the density matrix [84]

$$\langle \mathcal{F} \rangle = \mathrm{Tr}(\rho F). \tag{A.8}$$

The time evolution of the density matrix using Eq. A.5 is

$$\frac{d}{dt}\langle \rho \rangle = \frac{i}{\hbar}\left[\mathcal{H}, \rho\right]. \tag{A.9}$$

The time independent Hamiltonian, H_0, has eigenvalues and eigenfunctions given by $E_n = \hbar\omega_n$ and $\phi_n(\boldsymbol{r})$ respectively. These eigenfunctions are also linearly independent and form a complete set. To find the force on the atoms we apply the time dependent Schrodinger equation, Eq. A.10 [84]

$$\mathcal{H}\psi(\boldsymbol{r}, t) = i\hbar\frac{\partial \psi(\boldsymbol{r}, t)}{\partial t}. \tag{A.10}$$

Because of the completeness of the eigenfunctions we can expand $\psi(\boldsymbol{r}, t)$ in terms of $\phi_n(\boldsymbol{r})$ as in Eq. A.11 [84]

$$\mathcal{H}\psi(\boldsymbol{r}, t) = [H_0 + H'(t)]\sum_k c_k(t)\phi_k(\boldsymbol{r}). \tag{A.11}$$

Multiplying both sides of Eq. A.11 by the complex conjugate $\phi_j^*(\boldsymbol{r})$ and integrating over all space we obtain [84]

$$i\hbar\frac{dc_j(t)}{dt} = c_j(t)E_j + \sum_k c_k(t)H'_{jk}(t), \tag{A.12}$$

where we have $H'_{jk}(t) = \langle\phi_j|H'(t)|\phi_k\rangle$. Eq. A.12 represents a general solution for any number of excited states. For the case of only two states, g (ground) and e (excited), this becomes a two state atom and is well known as the Rabi two-level atom. From this we arrive at a coupled system involving two differential equations [3]

$$\begin{aligned} i\hbar\frac{c_g(t)}{dt} &= c_g(t)(E_g + H'_{gg}) + c_e(t)H'_{ge}(t) \\ i\hbar\frac{c_e(t)}{dt} &= c_e(t)(E_e + H'_{ee}) + c_g(t)H'_{eg}(t). \end{aligned} \tag{A.13}$$

The interaction terms, $H'_{ge}(t)$ and $H'_{eg}(t)$, are related by $H'_{ge}(t) = H'^*_{eg}(t)$ and are defined as

$$H'_{ge}(t) = -\boldsymbol{\mu}\cdot\boldsymbol{E}(\boldsymbol{r},t), \tag{A.14}$$

where $\boldsymbol{E}(\boldsymbol{r}$ is the electric field and $\boldsymbol{\mu} = q\langle e|\boldsymbol{r}|g\rangle$ is the dipole moment [10] of the atom with electric charge, q, and position, $\boldsymbol{r}$. Because H' possesses odd parity[2] only the opposite parity states of the atom can couple through this dipole interaction $H'_{ee}(t) = H'_{gg}(t) = 0$ giving the matrix form of the Hamiltonian as

$$\mathcal{H} = \begin{bmatrix} 0 & -\boldsymbol{\mu}\cdot\boldsymbol{E}^*(\boldsymbol{r},t) \\ -\boldsymbol{\mu}\cdot\boldsymbol{E}(\boldsymbol{r},t) & \hbar\omega_e \end{bmatrix}. \tag{A.15}$$

Now we can find the time evolution of the density matrix by substituting Eq. A.15 into Eq. A.9 to obtain the resultant matrix equation

$$\begin{bmatrix} \dot{\rho_{gg}} & \dot{\rho^*_{eg}} \\ \dot{\rho_{eg}} & \dot{\rho_{ee}} \end{bmatrix} = i\begin{bmatrix} \Omega^*(\boldsymbol{r},t)\rho_{eg} - \Omega(\boldsymbol{r},t)\rho^*_{eg} & \omega_e\rho^*_{eg} - \Omega^*(\boldsymbol{r},t)u \\ -\omega_e\rho_{eg} + \Omega^*(\boldsymbol{r},t)u & -\Omega^*(\boldsymbol{r},t)\rho_{eg} + \Omega(\boldsymbol{r},t)\rho^*_{eg} \end{bmatrix}, \tag{A.16}$$

[2]Odd parity arises if, *e.g* $\psi(x) = -\psi(-x)$. See any modern physics[97] or quantum mechanics[103] text.

where the Rabi frequency is defined as $\Omega(\boldsymbol{r},t) = \boldsymbol{\mu}\cdot\boldsymbol{E}(\boldsymbol{r},t)/\hbar$ and the population difference $u = \rho_{gg} - \rho_{ee}$. If the system is closed the total population will be conserved, thus $\rho_{ee}+\rho_{gg} = 1$ and $\rho_{eg} = \rho^*_{ge}$. With this we can now write the optical Bloch equations [84]

$$\begin{aligned}\frac{d\rho_{eg}(t)}{dt} &= -\frac{\gamma}{2}\rho_{eg} - i\omega_e\rho_{eg} + i\Omega(\boldsymbol{r},t)u \\ \frac{du}{dt} &= \gamma(1-u) + i(\Omega^*(\boldsymbol{r},t)\rho_{eg} - \Omega(\boldsymbol{r},t)\rho^*_{eg}).\end{aligned} \tag{A.17}$$

Here the spontaneous emission rate, γ, is defined as $\gamma = \frac{\omega_\ell^3\mu^2}{3\pi\epsilon_0\hbar c^3}$ where ω_ℓ is the laser frequency. The first term in Eq. A.17 was introduced to take the effects of spontaneous emission into account during the time evolution of the density matrix. Now if we let $\rho_{eg} = \sigma_{eg}e^{-i\omega_\ell t}$ and $\boldsymbol{E}(\boldsymbol{r},t) = \boldsymbol{E}(\boldsymbol{r})\cos(\omega_\ell t)$ then Eq. A.17 becomes [84, 108]

$$\begin{aligned}\frac{d\sigma_{eg}}{dt} &= -(\gamma/2 - i\delta)\sigma_{eg} + \frac{iu\Omega^*(\boldsymbol{r})}{2} \\ \frac{du}{dt} &= \gamma(1-u) + i(\Omega^*(\boldsymbol{r})\sigma_{eg} - \Omega(\boldsymbol{r})\sigma^*_{eg}).\end{aligned} \tag{A.18}$$

The higher frequency $2\omega_{ell}$ terms where ignored because they average to zero, this is known as the rotating wave approximation [42]. Also, the laser detuning from the atomic transition is given by $\delta = \omega_\ell - \omega_e$. The steady state solutions (*i.e.* $\frac{d\sigma_{eg}}{dt} = 0$ and $\frac{du}{dt} = 0$) of Eq. A.18 are given by [84, 108]

$$\begin{aligned}\sigma_{eg} &= \frac{2\Omega(-\delta + i\frac{\gamma}{2})}{\gamma^2\left[1 + \left(\frac{2\delta}{\gamma}\right)^2 + 4\left(\frac{\Omega}{\gamma}\right)^2\right]} \\ u &= \frac{1 + \left(\frac{2\delta}{\gamma}\right)^2}{\left[1 + \left(\frac{2\delta}{\gamma}\right)^2 + 4\left(\frac{\Omega}{\gamma}\right)^2\right]}.\end{aligned} \tag{A.19}$$

Now we are able to calculate the force operator using the conservation of population and the fact that we can calculate ρ_{gg} and ρ_{ee}. If we consider the case of an electric field produced by a traveling wave in the z-direction given by $E(z) = E_0\cos(kz - \omega_\ell t)$ we can write the

force operator as [108]

$$F = \begin{bmatrix} 0 & \mu\frac{\partial E^*(z)}{\partial z} \\ \mu\frac{\partial E^(z)}{\partial z} & 0 \end{bmatrix}. \tag{A.20}$$

Now we can write Eq. A.8 as

$$\begin{aligned} \langle \mathcal{F} \rangle &= \mathrm{Tr}(\rho F) \\ &= \mu\frac{\partial E}{\partial z}\sigma^*_{eg}e^{i\omega_\ell t} + \mu\frac{\partial E^*}{\partial z}\sigma_{eg}e^{-i\omega_\ell t}. \end{aligned} \tag{A.21}$$

Substituting σ_{eg} from Eq. A.19 into Eq. A.21 yields the force on a stationary atom [108]

$$F = \frac{\hbar k\gamma s}{2\left[1 + \left(\frac{2\delta}{\gamma}\right)^2 + s\right]}, \tag{A.22}$$

where the saturation parameter is defined as $s = \left(\frac{2\Omega}{\gamma}\right)^2$ or, in terms of intensity as $s = I/I_s$ where I, $I_s = \frac{\pi hc}{3\lambda^3\tau}$ are respectively the intensity of the laser light and saturation intensity with upper state lifetime τ. Now, let's consider an atom moving with a velocity v and apply these results. Such an atom will experience a Doppler shift of $\pm kv$ in the frequency of the applied laser. Here, the plus or minus sign represents an atom moving toward or away from the direction of the beam respectively. As a result, this atom will experience a detuned laser frequency, $\delta \pm kv$, and thus the overall force on the moving atom is then [84]

$$F = \pm\frac{\hbar k\gamma s}{2\left[1 + \left(\frac{2(\delta \mp kv)}{\gamma}\right)^2 + s\right]}, \tag{A.23}$$

where again the plus and minus sign represent the force on an atom moving toward or away from the laser beam. Now, if we have an atom in two counter propagating beams along the

z-direction the net force then becomes [84, 108]

$$F = \frac{\hbar k \gamma s}{2\left[1 + \left(\frac{2(\delta - kv)}{\gamma}\right)^2 + s\right]} - \frac{\hbar k \gamma s}{2\left[1 + \left(\frac{2(\delta + kv)}{\gamma}\right)^2 + s\right]}. \tag{A.24}$$

If we consider the limit where the Doppler shift is small compared to δ, Eq. A.24 then becomes $F = -\beta v$ where β represents the damping coefficient and is defined as [84, 108]

$$\beta = \frac{8\hbar k^2 s \delta}{\gamma\left[1 + \left(\frac{2\delta}{\gamma}\right)^2 + s\right]^2}. \tag{A.25}$$

Interpreting Eq. A.25 tells us that if we have laser light with a frequency detuned below the resonant frequency ($i.e\ \delta < 0$) atoms that move toward the light source will experience a Doppler shift closer to atomic resonance (blue shift) whereas atoms moving away from the source will experience a Doppler shift (red shift) further away from resonance. As a result, the atoms will absorb more photons from the counter-propagating beams and result in a decreased velocity. If three pairs of such counter-propagating beams are used in orthogonal directions to each other the atoms will then experience a damping force in all three dimensions regardless of the direction of the atoms' velocity. Because this force is dependent on the velocity of the atoms it is thus non-conservative. The force from this optical setup utilizing laser beams where the frequency is detuned below atomic resonance is what served as the basis for laser cooling techniques and eventual realization of a MOT.

Limitations of Laser Cooling

Until very recently [123, 105], the ability to cool atoms down by purely using the damping force was limited due to the random nature of the photon scattering process used to create the optical molasses. Such a random process caused a diffusion of the atoms in momentum space and thus the temperature of the atoms would actually increase. As a result, a steady state is

eventually reached whereupon the limiting temperature, known as the Doppler temperature T_D, is reached and is defined as

$$T_D = \frac{\hbar\gamma}{2k_B}, \tag{A.26}$$

where γ is the natural line width. For ^{87}Rb atoms this Doppler temperature is 146μK. However, in 1988 [76] it was discovered during laser cooling experiments involving Sodium that a temperature below the Doppler temperature could be obtained. This became known as sub-Doppler cooling and it was realized by W. Phillips and his co-workers that the multiple energy levels in the atoms were not considered in the two-level system and thus contributed to further reduce the temperature. This sub-Doppler cooling also became known as polarization gradient cooling as this cooling is due to the gradient in the polarization of the laser beams. This effect was then used by the Cohen-Tanoudji group the following year [28] to reach a further temperature limit determined by the energy from a single photon recoil $E_r = \frac{\hbar^2 k^2}{2m}$ where this new temperature limit is known as the recoil temperature and is given by [84]

$$T_r = \frac{\hbar^2 k^2}{m k_B}. \tag{A.27}$$

The recoil temperature ^{87}Rb is then 360nK.

Magneto-Optical Trap (MOT)

The Magneto-Optical Trap or MOT is one of the most widely used methods to trap neutral atoms and it utilizes both optical and magnetic fields. The first successful MOT was realized in 1987 by E. L. Raab and co-workers [93]. A working MOT depends upon two components, an inhomogeneous magnetic field and near-resonant laser beams arranged appropriately. One of the main advantages in using a MOT is that it is a robust setup as it doesn't rely on precise balance of the counter-propagating beams nor upon a high degree of their polarization. To understand the basic theory behind a MOT let's consider a simple atomic transition scheme with $J_g = 0 \rightarrow J_e = 1$ subjected to an external linearly inhomogeneous magnetic field

$B = B(z) = B_0 z$. The magnetic field then causes a Zeeman split of the excited states into three components $M_e = -1, 0$, and $+1$ as diagrammed in Fig. 41 (Adapted from Metcalf *et al.* [84]). Now, two counter-propagating laser beams possessing opposite circular polarization and detuned below the atomic transition without the magnetic field are applied and thus completing the MOT setup.

The applied magnetic field with $B > 0$ causes a Zeeman shift where the excited states, $M_e = +1$ and $M_e = -1$, are shifted up and down respectively. This shift is reversed to $M_e = \mp 1$ if the field is reversed to $B < 0$. As a result, at a position z' in Fig. 41 the applied magnetic field will tune the $\Delta M = -1$ and $\Delta M = +1$ transitions closer and further away to the resonance respectively [84]. If we let the polarization of the right laser beam be σ_-

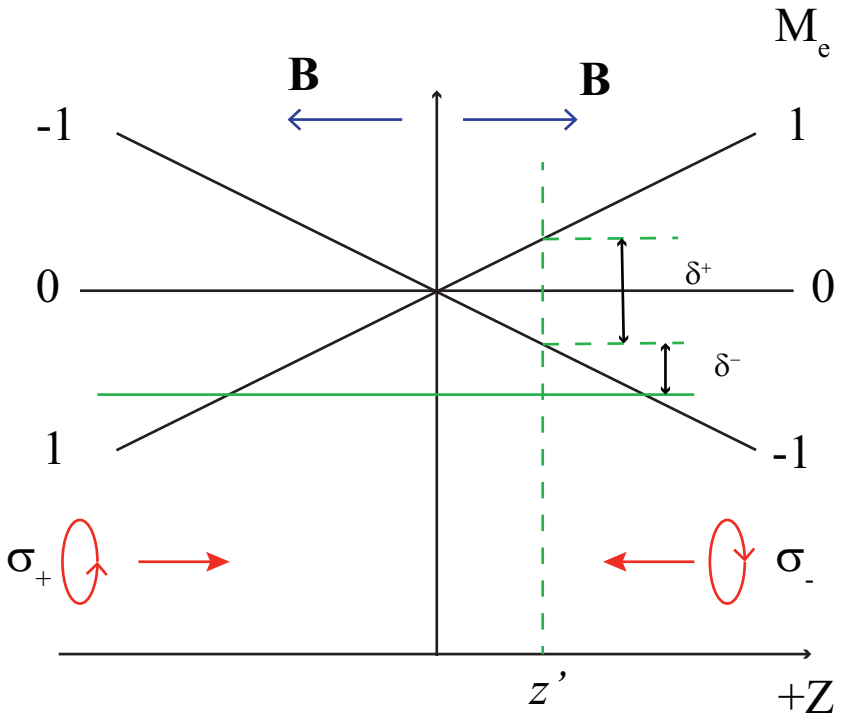

Figure 41: Energy level diagram of a one-dimensional MOT.

and the polarization of the left beam be σ_+ then the atoms will scatter more light from the former beam rather than the latter. This action thus causes the atoms to be driven towards the center of the MOT where the magnitude of the magnetic field is zero. For the other side of the trap the applied magnetic field causes a reversed situation of the right side where the

$\Delta M = +1$ transition is tuned closer to the resonance. This situation thus causes atoms in the σ_+ beam to scatter more light and as a result the atoms are driven towards the center of the trap. The damping force in the optical molasses due to the Doppler effect affects atoms in velocity space while the MOT setup operates in position space. As a result, using the laser light possessing a frequency detuned below resonance and in tandem with the B-field obtains compression and cooling of the atoms. Thus far, this MOT scheme has been in one-dimension but it can easily be extended to three dimensions with the addition of three pairs of such counter-propagating beams. The detuning from each applied laser beam in the presence of the magnetic field is [84]

$$\delta_\pm = \delta \mp \boldsymbol{k} \cdot \boldsymbol{v} \pm \mu' B/\hbar. \tag{A.28}$$

Here, the effective magnetic moment is defined as $\mu' = \mu_B(g_E M_e - g_g M_g)$ where μ_B is the Bohr magneton and g is the Lande' g-factor. As a result, the net force on the atoms becomes [84]

$$F_\pm = \pm\frac{\hbar \boldsymbol{k}\gamma}{2}\frac{s_0}{\left[1 + s_0 + \left(\frac{2\delta_\pm}{\gamma}\right)^2\right]}. \tag{A.29}$$

Here, $s_0 = \left(\frac{2|\Omega|}{\gamma}\right)^2 = \frac{I}{I_s}$

Evaporative Cooling Theory

To achieve the BEC transition it is necessary for the phase space density, $\rho = n\lambda_{dB}^3$, to become greater than 2.612 where n is the density of the particles and λ_{dB} is the de Broglie wavelength[3]. At room temperature the value of this phase space density is $\rho \approx 10^{-6}$ and for an atomic beam this becomes $\rho \approx 10^{-10}$. In Sec. 2.2 it was shown that only very recently that solely using laser cooling to cool atoms was limited by the Doppler and recoil limits. The phase space density at these limits are between $\rho = 10^{-5}$ and $\rho = 10^{-4}$. Using the traditional

[3]See the appendix, "Bose-Einstein Statistics", for a more thorough derivation of Bose-Einstein Condensation.

laser cooling techniques it is possible to achieve temperatures in the microKelvin range without much loss of atoms. This thus increases the density of the atomic gas. Increasing this density leads to a dilemma in which an increase in the collision rate of the atoms with one in an excited state within the gas, known as S+P collisions. Because these collisions are inelastic an energy exchange occurs and thus leading to an increase of heating of the atoms. Because of this effect it is necessary to avoid using near resonant light to attempt to cool atoms further to achieve a BEC. A possible solution to this problem was realized by the use of evaporative cooling and thus leading to an increase in the phase space density. The idea of evaporative cooling was first proposed to be applied to atomic Hydrogen in 1985 by Harald Hess [56]. The idea of evaporative cooling is to preferentially remove atoms from an atomic gas that posses a higher than average energy. Removal of these atoms would then cause a rethermalization of the remaining atoms due to elastic collisions. Because the remaining atoms in the cloud now possess lower temperature and occupy less space the overall phase space density increases. This concept was first applied to alkali atoms with laser cooling in 1994 [129].

Evaporative cooling techniques have been achieved using either magnetic fields or a far-off-resonant optical light source. In our lab the latter was used and its theory of operation will be described for the remainder of this section. The Far-Off-Resonant-Trap or FORT is based on the idea that a laser off atomic resonance creates a potential that is attractive or repulsive depending on whether the light is red or blue detuned from the atomic transitions. The depth of such a trap is dependent upon the intensity of laser and its detuning by[84]

$$U \approx \frac{\hbar I}{4\delta_\ell}. \tag{A.30}$$

However, the spontaneous scattering rate of the FORT dependent upon the square of the detuning in the following way

$$U \approx \frac{\Gamma \hbar I}{4\delta_\ell^2}, \tag{A.31}$$

where Γ is the spontaneous emission rate of the atoms. This results in an advantage of using the FORT because it is possible to achieve a trap with a potential well depth with a reduced scatter rate.

There have been many different models for evaporative cooling developed over the years but we will follow the model proposed by Davis *et. al.* [31] as it is relatively easy to follow. The trap depth in this model is first lowered to a finite energy $\eta k_B T$, afterwards the atoms thermalize due to collisions and then the effect of this on the usual thermodynamic quantities volume, density, and temperature are calculated. The ratio of the atoms remaining in the trap after this cooling process is given by $\nu = \frac{N'}{N}$ and the quantity ${\gamma_T}^4$ measures the temperature of the remaining atoms after the hot atoms are removed. This quantity is defined as [31]

$$\gamma_T = \frac{\log(T'/T)}{\log(\nu)}. \tag{A.32}$$

The values after cooling are represented here by the primed quantities. With this we can now state the scaled thermodynamic quantities, $N' = N\nu$, $T = T\nu^{\gamma_T}$, and $V' = V\nu^{\gamma_T \xi}$ where the quantity, ξ is dependent upon the type of potential under consideration. If, for example, the trap is a linear potential such as a spherical quadrupole trap then $\xi = 3$. If the potential is harmonic such as in an optical trap then $\xi = 3/2$. The phase space density using the defined quantities becomes scaled as $\rho' = \rho\nu^{[1-\gamma_T(\xi+3/2)]}$ and the collision rate also as $k' = k^{[1-\gamma_T(\xi-1/2)]}$. This re-scaling allows us to utilize the parameters γ_T, ξ, and ν given a value of η we can calculate the evolution of the thermodynamic quantities. For atoms trapped in a trapping potential $U(x, y, z)$ the density of states is [31]

$$D(E) = \frac{2\pi(2M)^{3/2}}{\hbar^3} \int_V \sqrt{E - U(x, y, z)} d^3r. \tag{A.33}$$

[4]Davis *et. al.* used γ in their paper but we are adding a subscript T here to avoid confusion with the natural linewidth, γ.

The fraction of atoms remaining in the trap after lowering its depth to $\eta k_B T$ is given by [31]

$$\nu = \frac{1}{N}\int_0^{\eta k_B T} D(E) e^{-\frac{E-\mu}{k_B T}} dE, \tag{A.34}$$

where the chemical potential is given by μ and the exponential term is due to the Maxwell-Boltzmann distribution of these atoms. Now if we define the reduced energy by $\epsilon = \frac{E}{k_B T}$ and the reduced density of states as $\Delta(\epsilon) = \frac{\epsilon^{\xi+1/2}}{\Gamma(\xi+3/2)}$ with $\Gamma(x)$ being the gamma function then Eq. A.34 can be recast [31] as

$$\nu = \int_0^{\eta} \Delta(\epsilon) e^{-\epsilon} d\epsilon. \tag{A.35}$$

The total energy of the atoms after this lowering is [31]

$$\alpha(\eta) = \int_0^{\eta} \epsilon \Delta(\epsilon) e^{-\epsilon} d\epsilon. \tag{A.36}$$

In terms of $k_B T$ the average total energy by atom is then $\frac{\alpha(\eta)}{\nu(\eta)}$. If we let $\eta \to \infty$ then $\frac{\alpha(\eta)}{\nu(\eta)} = (3/2 + \xi)$ and thus the ratio of the temperature becomes [31]

$$\frac{T'}{T} = \frac{\alpha(\eta)/\nu(\eta)}{\alpha(\infty)/\nu(\infty)}. \tag{A.37}$$

Using Eq. A.37 the quantity defined by Eq. A.32 then becomes [31]

$$\gamma_T = \frac{\log\left(\frac{\alpha(\eta)}{\nu(\eta)\alpha(\infty)}\right)}{\log\left(\nu(\eta)\right)}. \tag{A.38}$$

The above average excess energy that has been carried away by the evaporated atoms is measured by the quantity defined by Eq. A.38. The value of this quantity can be determined if we know the specific type of potential under consideration. If, for example we consider a harmonic trap where $\xi = 3/2$ then we have [31]

$$\nu(\eta) = \frac{1}{\Gamma(3)}\int_0^{\eta} \epsilon^2 e^{-\epsilon} d\epsilon = 1 - \frac{2 + 2\eta + \eta^2}{2e^{\eta}}, \tag{A.39}$$

and

$$\alpha(\eta) = \frac{1}{\Gamma(3)} \int_0^\eta \epsilon^3 e^{-epsilon} d\epsilon = 3 - \frac{6 + 6\eta + 3\eta^2 + \eta^3}{2e^\eta}, \tag{A.40}$$

where the gamma function is defined by $\Gamma(n) = (n-1)!$ [19]. We can see that as ξ increases the phase space density also increases which is due to the volume shrinking faster than the decreasing temperature ($i.e\ T \propto V^\xi$). This process also has the additional effect of increasing the rate of elastic collisions which also increases the rethermalization process. This in turn speeds up the cooling process which eventually reaches the critical phase space density and temperature necessary to create a BEC [6, 30].

Bose-Einstein Statistics

Introduction

Our research in quantum information utilizes a special state of matter known as the Bose-Einstein condensate (BEC) as a basis. This state of matter is governed by the theory of Bose-Einstein statistics which was first formulated by Satyendra Nath Bose and Albert Einstein in 1924 although the first BEC of neutral atoms with dilute gases wasn't realized until 1995. For more on this fascinating history with Bose and Einstein one should consult some of the well-written works covering this [60, 98]. The BEC offers some advantages in this work as it is larger than purely atomic systems and can be rapidly generated to efficiently conduct repeated experiments. In this appendix we will describe some of the general theory of Bose-Einstein condensation first starting with a derivation of the Bose-Einstein distribution before showing how condensation is predicted at very low temperatures and high phase space density.

Bose-Einstein distribution

We consider a collection of n_i particles that can be partitioned into g_i discrete states or cells divided by $g_i - 1$ partitions. Note that Bosons are particles that posses integer spin and

unlike Fermions, multiple particles can occupy a given state. This number of particles is also known as the degeneracy of the state because Bosons are indistinguishable. A simple example of this is shown in Fig. 42. The number of ways that these objects, $n_i + g_i - 1$, can

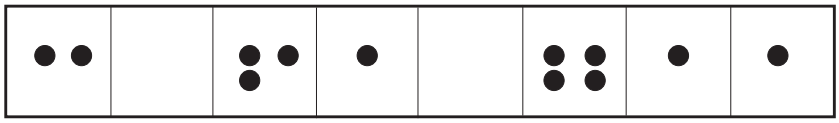

Figure 42: Example of states and particles governed by Bose-Einstein statistics. Here $n_i = 12$, $g_i = 8$, and $g_i - 1 = 7$. Note that this is just one possible arrangement of the total objects, $n_i + g_i - 1 = 27$.

be arranged is given by

$$(n_i + g_i - 1)!. \tag{A.41}$$

However, because the particles are identical and indistinguishable all of the permutations that differ by the ordering of the particles only are the same. Thus we have to divide Eq. (A.41) by $n_i!$. This same observation also holds true for the permutations of the divisions and thus we must also divide Eq. (A.41) by $(g_i - 1)!$. This then gives us for the total possible permutations [4]

$$\frac{(n_i + g_i - 1)!}{n_i!(g_i - 1)!}. \tag{A.42}$$

The total partition probability for all possible permutations among the energy levels is obtained by the product of each expression given by Eq. (A.42) for each energy level

$$P = \prod_i \frac{(n_i + g_i - 1)!}{n_i!(g_i - 1)!}. \tag{A.43}$$

Now we need to find the most probable partition by the use of Lagrange multiples and considering the maximum of $\ln(P)$. Taking the logarithm of Eq. 3 we have

$$\ln(P) = \sum_i [\ln((n_i + g_i - 1)!) - \ln(n_i!) - \ln((g_i - 1)!)]. \tag{A.44}$$

Applying Stirling's formula, $\ln(x!) = x\ln(x) - x$, we have [81]

$$\ln(P) = \sum_i [(n_i + g_i - 1)\ln(n_i + g_i - 1) - n_i \ln(n_i) - (g_i - 1)\ln(g_i - 1)]. \tag{A.45}$$

Now we set $\delta \ln(P) = 0$ and obtain

$$-\delta(\ln(P)) = \sum_i [-\ln(n_i + g_i - 1) + \ln(n_i)] = 0. \tag{A.46}$$

Applying the Lagrangian multipliers $\alpha \sum_i \delta n_i = 0$, and $\beta \sum_i \epsilon_i \delta n_i = 0$ to Eq. 6 where ϵ_i is an energy level. This then gives

$$\sum_i [-\ln(n_i + g_i - 1) + \ln(n_i) + \alpha + \beta\epsilon_i] = 0. \tag{A.47}$$

The equilibrium condition is reached if the term in brackets is equal to zero, i.e.

$$-\ln(n_i + g_i - 1) + \ln(n_i) + \alpha + \beta\epsilon_i = 0. \tag{A.48}$$

Since $n_i + g_i - 1 \gg 1$ we can drop the one and obtain

$$-\ln(n_i + g_i) + \ln(n_i) + \alpha + \beta\epsilon_i = 0. \tag{A.49}$$

Solving this equation for n_i gives us the Bose-Einstein distribution

$$n_i = \frac{g_i}{e^{\alpha + \beta\epsilon_i} - 1}. \tag{A.50}$$

As we will see this distribution will exhibit very interesting behavior at very low temperatures giving rise to the famous BEC.

Bose-Einstein Condensation

As mentioned above the Bose-Einstein distribution describes the behavior of particles that are Bosons. Examples of Bosons include alpha particles, photons, and deuterons. Also included here are neutral atoms where the sum of the spins of their particles are an integer multiple. In our case for ^{87}Rb the total number of particles is 124 and thus has an integer spin allowing for its use in creating a BEC. It is also interesting to note that prior to 1995 with the realization of the first BEC the behavior of Bosons at very low temperatures was only observed in supercooled ^{4}He [80, 57]. In Eq. 10 we let the chemical potential be defined as $\alpha = -\mu\beta$ where $\beta = \frac{1}{kT}$ giving us

$$n_i = \frac{g_i}{e^{\beta(\epsilon_i - \mu)} - 1}. \tag{A.51}$$

The Boson distribution in continuous form can be written as [118]

$$N = \int_0^\infty \frac{D(\epsilon)}{e^{\beta(\epsilon_i - \mu)} - 1} d\epsilon, \tag{A.52}$$

where the density of states, $D(\epsilon)$, is defined as

$$D(\epsilon) = \frac{V}{4\pi^2} \left(\frac{2m}{\hbar^2}\right)^{\frac{3}{2}} \epsilon^{\frac{1}{2}}. \tag{A.53}$$

Combining Eq. 12 and Eq. 13 we have

$$N = \int_0^\infty \frac{V}{4\pi^2} \left(\frac{2m}{\hbar^2}\right)^{\frac{3}{2}} \epsilon^{\frac{1}{2}} \frac{1}{e^{\beta(\epsilon_i - \mu)} - 1} d\epsilon. \tag{A.54}$$

Now let $x = \beta\epsilon$ to get

$$N = \frac{V}{4\pi^2} \left(\frac{2m}{\hbar^2}\right)^{\frac{3}{2}} (k_B T)^{\frac{3}{2}} \int_0^\infty \frac{x^{\frac{1}{2}}}{e^{-\beta\mu} e^x - 1} dx. \tag{A.55}$$

Let $\lambda = e^{\beta\mu}$ a quantity defined as the fugacity. We can see that because $\mu < 0$ this fugacity must have the condition $\lambda^{-1} > 1$. Inserting this parameter into Eq. 15 we have

$$N = \frac{V}{4\pi^2}\left(\frac{2m}{\hbar^2}\right)^{\frac{3}{2}}(k_B T)^{\frac{3}{2}}\int_0^\infty \frac{x^{\frac{1}{2}}}{\lambda^{-1}e^x - 1}dx. \tag{A.56}$$

Eq 16 is very significant regarding the behavior of the gas of Bosons because when the temperature, T, is reduced the term $T^{\frac{3}{2}}$ also reduces. However, because the total number of particles is constant this means that the integral will have to increase to compensate. Because the only parameter in the integral that can vary is the fugacity this fugacity would have to in turn decrease to increase the overall value of the integral. However, we noted above that the fugacity cannot decrease below one. If the integral was divergent as $\lambda \to 1$ this would not be an issue, however this integral is convergent for $x = 0$ and $\lambda = 1$. The value of this integral is

$$\int_0^\infty \frac{x^{\frac{1}{2}}}{e^x - 1}dx = \frac{\sqrt{\pi}}{2}\zeta\left(\frac{3}{2}\right) = 1.306\sqrt{\pi} = 2.315. \tag{A.57}$$

Here $\zeta\left(\frac{3}{2}\right)$ is the Riemann zeta function. This analysis shows us that the integral cannot be correct below a certain critical temperature T_C and thus we set the integral to its maximum possible value

$$N = 2.315\frac{V}{4\pi^2}\left(\frac{2m}{\hbar^2}\right)^{\frac{2}{3}}(k_B T_C)^{\frac{2}{3}}. \tag{A.58}$$

Solving for $k_B T_C$ gives us

$$k_b T_C = \left(\frac{2\pi\hbar^2}{m}\right)\left(\frac{N}{2.612V}\right)^{\frac{2}{3}}. \tag{A.59}$$

For temperatures below the critical temperature the equation for the total number of particles has to be modified to include the number of particles in the zero energy state $\epsilon = 0$. This is because Eq. 16 doesn't have a solution for temperatures below the critical temperature. This problem arises from the fact that Eq. 12 is no longer valid at temperatures below T_C. To modify Eq. 12 we only need to add the number of Bosons that occupy the lowest energy

level $\epsilon = 0$ by adding the term N_0

$$N = N_0 + \int_0^\infty \frac{D(\epsilon)}{e^{\beta(\epsilon_i - \mu)} - 1} d\epsilon. \tag{A.60}$$

Using this new distribution Eq. 16 then becomes

$$N = N_0 + \frac{V}{4\pi^2} \left(\frac{2m}{\hbar^2} \right)^{\frac{3}{2}} (k_B T)^{\frac{3}{2}} \int_0^\infty \frac{x^{\frac{1}{2}}}{\lambda^{-1} e^x - 1} dx. \tag{A.61}$$

When the temperature is above the critical temperature the occupation of N_0 is much lower than N and thus can be neglected. Below the critical temperature N_0 becomes comparable to N. The transition at the critical temperature is known as the Bose-Einstein condensation. Below the critical temperature we can write the total number of particles as

$$N = N_0 + N \left(\frac{T}{T_C} \right)^{\frac{3}{2}}. \tag{A.62}$$

Solving this for N_0 gives us

$$N_0 = N \left[1 - \left(\frac{T}{T_C} \right)^{\frac{3}{2}} \right]. \tag{A.63}$$

Eq. 23 shows that as $T \to 0$ the occupation number N approaches the occupation of the ground state N_0 giving the Bose-Einstein condensate.

Floquet Theory

In our research with optically kicked BECs the problem of a second-order differential equation with periodic coefficients arises when one applies the Schrodinger equation to the system. A similar situation also occurs in solid state physics when one considers an electron in a periodic potential due to the crystal structure of a solid, giving rise to what are known as Bloch functions [54]. Such equations are a special case of a class of differential equations known as Mathieu's equations. These equations historically first appeared during the latter half of the 19th century due to analysis of a vibrating elliptical membrane and of the orbit

of the Moon [70]. In 1883 Gaston Floquet published the first paper describing the complete solution and description of the properties of an nth order linear differential equation with periodic coefficients [41]. Such differential equations arise in electrical engineering, solid state theory, and in orbital mechanics. In spite of such applications an elementary detailed solution of this equation is not readily easy to find. Some older differential equations books contain detailed solutions as well as a few articles in The American Journal of Physics. However, most publications in our research that introduce Floquet theory for the AOKR simply state the solution while referring to previous works. If one follows these references back to S. Fishman's original 1982 paper they will find that this refers to a PhD thesis from 1965 studying the quantum dynamics of a system under a strong oscillating field [106, 40]. Another line of explanation is through the use of Bloch theory from solid state physics. This method is applicable because the periodic potential in time can be projected onto a line, thus allowing the use of Bloch theory. In this appendix we will outline in detail solving this differential equation using a more "brute force" approach. Other methods involve group theory which can be found in any solid state physics text. We will first introduce and solve the classical kicked rotor as understanding it will help in solving the case in the quantum regime.

Classical kicked rotor

The classical kicked rotor was first introduced in the late 1970s by Chirikov [22] and it consists of a point mass m constrained to a circle of radius R subjected to a periodic force f or "kicks" as shown in Fig. 43. The Hamiltonian for this system can be written as

$$\mathcal{H} = \frac{L^2}{2I} + fRcos(\theta)\sum_{n=1}^{\infty}\delta(t-nT), \tag{A.64}$$

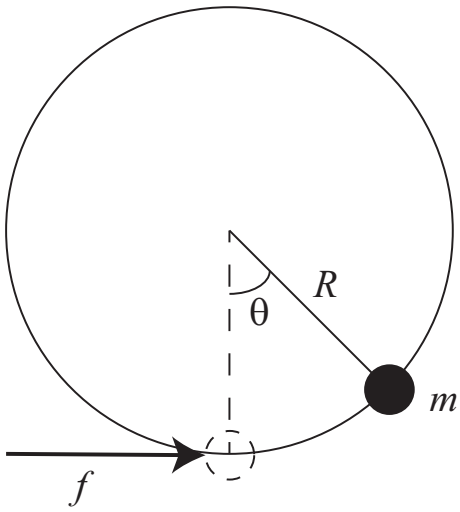

Figure 43: Classical kicked rotor where a periodic force or "kick" is applied to a mass m.

where L, I, and T are the angular momentum, moment of inertia, and period respectively of the system. Applying Hamilton's equations we have

$$\dot{\theta} = \frac{\partial \mathcal{H}}{\partial L} = \frac{L}{I}, \tag{A.65}$$

and

$$\dot{L} = -\frac{\partial \mathcal{H}}{\partial \theta} = fRsin(\theta) \sum_{n=1}^{\infty} \delta(t - nT). \tag{A.66}$$

Integrating these equations over one period from nT to $(n+1)T$ we obtain

$$\theta_{n+1} - \theta_n = \int_{nT}^{(n+1)T} \frac{L}{I} dt = \frac{L_{n+1}T}{I}, \tag{A.67}$$

and

$$L_{n+1} - L_n = \int_{nT}^{(n+1)T} fRsin(\theta) \sum_{n=1}^{\infty} \delta(t - nT) dt = fRsin(\theta_n). \tag{A.68}$$

If we let $\acute{L} = \frac{LT}{I}$ then we obtain the standard map

$$\acute{\theta_{n+1}} = \acute{L_{n+1}} + \theta_n, \tag{A.69}$$

and

$$L_{n+1}^{'} = L_{n}^{'} + ksin(\theta_n), \tag{A.70}$$

where $k = \frac{fRt}{I}$ is the "kicking strength". The standard map in this form allows us to readily plot the results in MATLAB for various values of the respective parameters [39]. The results for a few values of k after 1500 iterations are shown in Fig. 44,45,46. From these figures

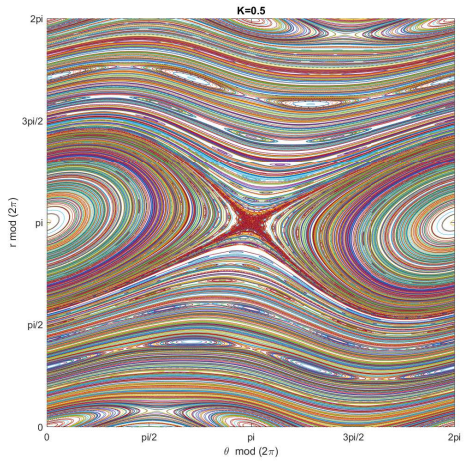

Figure 44: Standard map for $k = 0.5$.

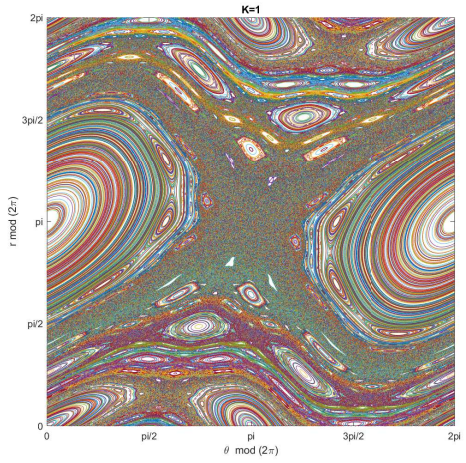

Figure 45: Standard map for $k = 1.0$.

we can see that the system becomes more chaotic as the kick strength is increased and the "islands of stability" gradually vanish. The properties of the classical Chirikov system have been studied extensively over the last few decades.

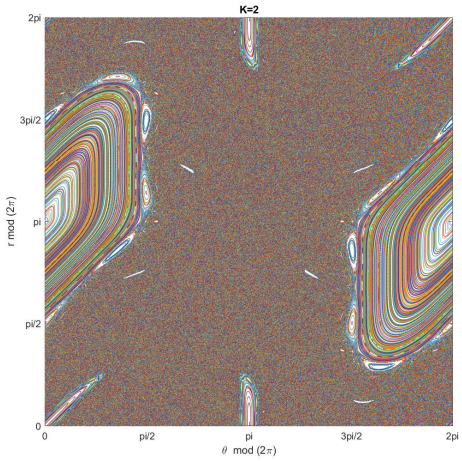

Figure 46: Standard map for $k = 2.0$.

Quantum Kicked Rotor

The above discussion of the classical kicked rotor gives us a good starting point to consider the quantum mechanical case. The form of the Hamiltonian is mostly unchanged other than the use of a modulus function to project the system onto a line. The Hamilton for the AOKR in our experiments is

$$H(\hat{X}, \hat{P}, t) = \frac{\hat{P}^2}{2M} + \hbar\phi_d \cos(G\hat{X}) \sum_{q=0}^{t} \delta(t - qT). \tag{A.71}$$

Here, $\phi_d = \frac{\Omega^2 \Delta t}{8\delta_L}$ is the kicking strength in terms of the Rabi frequency, time duration of the light pulse, and detuning of the laser from the atomic transition. Letting $\mathcal{H} = \frac{MH}{\hbar^2 G^2}$, $t' = \frac{2\pi t}{T_{\frac{1}{2}}}$, $\hat{p} = \frac{\hat{P}}{\hbar G}$, $\tau = \frac{2\pi T}{T_{\frac{1}{2}}}$, and $\hat{x} = G\hat{X}$ where $T_{\frac{1}{2}} = \frac{2\pi M}{\hbar G^2}$ is the half Talbot time we obtain the Hamiltonian in dimensionless form for convenience in our analysis

$$\mathcal{H}(\hat{x}, \hat{p}, t') = \frac{\hat{p}^2}{2} + \phi_d \cos(\hat{x}) \sum_{q=0}^{t} \delta(t' - q\tau). \tag{A.72}$$

We now apply the time dependent Schrodinger equation to this Hamiltonian to obtain

$$-\frac{i}{\hbar}\frac{\partial}{\partial t}|\psi(t)\rangle = \mathcal{H}|\psi(t)\rangle. \tag{A.73}$$

The solution to the time-dependent Schrodinger equation is found by the use of the unitary operator for time evolution. This gives us a general solution for the equation

$$|\psi(t)\rangle = [exp(-\frac{i}{\hbar}\int_0^t \mathcal{H}(t')dt')]_+|\psi(0)\rangle = U(t,0)|\psi(0)\rangle. \tag{A.74}$$

Here the "+" subscript is for correct time ordering. With this we can write

$$U(t,0) = U(t,s)U(s,0). \tag{A.75}$$

We are now able to apply this form of the unitary operator to our Hamiltonian over one period τ, separating the period over an infinitesimal time ϵ

$$U(\tau) = U(\tau-\epsilon,\epsilon)U(\tau+\epsilon,\tau-\epsilon), \tag{A.76}$$

yields

$$U(\tau) = exp(-i\int_\epsilon^{\tau-\epsilon}\mathcal{H}(t)dt)exp(-i\int_{\tau-\epsilon}^{\tau+\epsilon}\mathcal{H}(t)dt). \tag{A.77}$$

The first integral is easy to see because the limits of the integral are outside of the delta function in the potential term. This gives us $e^{-\frac{i\hat{p}^2\tau}{\hbar 2}}$ and this known as the "free evolution" operator due to the presence of the time parameter τ. The second integral becomes independent of time due to the presence of the delta function term. This then gives us $e^{-i\phi_d cos\hat{x}}$. This is known as the "kick" operator as it is dependent upon the kicking strength. With these operators we can write the complete Floquet operator

$$U(\tau) = U_{free}U_{kick} = e^{-\frac{i\hat{p}^2\tau}{\hbar 2}}e^{-i\phi_d cos\hat{x}}. \tag{A.78}$$

From this result follows the general wavefunction solving the Schrodinger equation

$$|\psi(t)\rangle = U(\tau)|\psi(0)\rangle. \tag{A.79}$$

This above method of solution is useful for a single cycle of the quantum kicked rotor. However, in our experiments the QKR is repeated multiple times and is thus periodic. This periodic behavior enables us to project onto a line with $\theta = \hat{x} mod(2\pi)$ and thus allowing us to use Bloch's theorem to find the wavefunction. In the following a proof of this theorem is presented. A similar although more terse treatment can be found in Magnus and Winkler [78] as well as in the work by Kaplan [61]. We start with Schrodinger's equation for a periodic potential $U(x)$ where $U(x + na) = U(x)$ [54]

$$\frac{d^2\psi(x)}{dx^2} + U(x)\psi(x) = 0. \tag{A.80}$$

Because this equation is a second order differential equation, we know that two solutions exist; ψ_1 and ψ_2. We also know that these solutions will also satisfy the above equation, giving us the following two equations

$$\psi_1'' + U\psi_1 = 0, \tag{A.81}$$

and

$$\psi_2'' + U\psi_2 = 0. \tag{A.82}$$

If we multiply both of these by ψ_1 and ψ_2 we have

$$\psi_1''\psi_2 + U\psi_1\psi_2 = 0, \tag{A.83}$$

and

$$\psi_2''\psi_1 + U\psi_2\psi_1 = 0. \tag{A.84}$$

Subtracting these equations then yields

$$\psi_2''\psi_2 - \psi_2''\psi_1 = 0. \tag{A.85}$$

This result is the derivative of the Wronskian

$$\frac{dW}{dx} = 0, \tag{A.86}$$

where W is the determinant

$$W = \begin{vmatrix} \psi_1 & \psi_2 \\ \psi_1' & \psi_2' \end{vmatrix}. \tag{A.87}$$

The periodic property of the potential also allows us to show that

$$\frac{d^2\psi(x+a)}{dx^2} + U(x+a)\psi(x+a) = 0, \tag{A.88}$$

yielding

$$\frac{d^2\psi(x+a)}{dx^2} + U(x)\psi(x+a) = 0. \tag{A.89}$$

With this periodicity in mind we can write our two solutions in the following form

$$\psi_1(x+a) = A\psi_1(x) + B\psi_2(x), \tag{A.90}$$

and

$$\psi_2(x+a) = C\psi_1(x) + D\psi_2(x). \tag{A.91}$$

Writing this system of equations in determinant form

$$\begin{vmatrix} A\psi_1 + B\psi_2 & C\psi_1 + D\psi_2 \\ A\psi_1' + B\psi_2' & C\psi_1' + D\psi_2' \end{vmatrix} = \begin{vmatrix} \psi_1 & \psi_2 \\ \psi_1' & \psi_2' \end{vmatrix} \begin{vmatrix} A & C \\ B & D \end{vmatrix}. \tag{A.92}$$

Because the Wronskian is a constant not equal to zero we conclude that the determinant of coefficients be equal to one

$$\begin{vmatrix} A & C \\ B & D \end{vmatrix} = 1, \tag{A.93}$$

or

$$AD - BC = 1. \tag{A.94}$$

These results allow us to write the solution in the following form

$$\psi(x + a) = \Delta\psi(x), \tag{A.95}$$

and

$$\psi(x) = \alpha\psi_1(x) + \beta\psi_2(x) \tag{A.96}$$

$$\psi(x + a) = \alpha\psi_1(x + a) + \beta\psi_2(x + a). \tag{A.97}$$

Using Eqs. (A.96) and (A.97) we have:

$$\begin{aligned} \psi(x) &= \alpha(A\psi_1(x) + B\psi_2(x)) + \beta(C\psi_1(x) + D\psi_2(x)) \\ &= \alpha[A\psi_1(x) + B\psi_2(x)] + \beta[C\psi_1(x) + D\psi_2(x)] \\ &= (\alpha A + \beta C)\psi_1(x) + (\alpha B + \beta D)\psi_2(x). \end{aligned} \tag{A.98}$$

Notice that the last line of Eq. A.98 resembles the form of Eq. A.97 and so we can write:

$$\psi(x + a) = \Delta\alpha\psi_1(x) + \Delta\beta\psi_2(x). \tag{A.99}$$

This result then gives us the following system of equations:

$$\begin{aligned} \alpha A + \beta C &= \Delta\alpha \\ \alpha B + \beta D &= \Delta\beta, \end{aligned} \tag{A.100}$$

or in matrix form:

$$\begin{bmatrix} A - \Delta & C \\ B & D - \Delta \end{bmatrix} \begin{bmatrix} \alpha \\ \beta \end{bmatrix} = 0. \tag{A.101}$$

Nontrivial solutions exist only if the determinant of the coefficients is zero

$$\begin{vmatrix} A-\Delta & C \\ B & D-\Delta \end{vmatrix} = 0, \tag{A.102}$$

and simplifying this yields

$$\begin{aligned} (A-\Delta)(D-\Delta) - CB &= 0 \\ \Delta^2 - (A+D)\Delta + 1 &= 0 \\ \Delta - (A+D) &= -\Delta^{-1} \\ \Delta + \Delta^{-1} &= (A+D). \end{aligned} \tag{A.103}$$

Now if we take the Wronskian matrix $\begin{bmatrix} A & C \\ B & D \end{bmatrix}$ and let its eigenvalues represented by Δ_+ and Δ_- and using the theorem that the trace of a matrix is equal to the sum of the eigenvalues we find that

$$\begin{aligned} \begin{bmatrix} A & C \\ B & D \end{bmatrix} &= A + D \\ &= \Delta_+ + \Delta_-^-. \end{aligned} \tag{A.104}$$

This result then implies the following

$$\Delta_+ + \Delta_+^{-1} = A + D, \tag{A.105}$$

$$\Delta_- + \Delta_-^{-1} = A + D, \tag{A.106}$$

and

$$\Delta_+ + \Delta_- = A + D. \tag{A.107}$$

From these equations we can see that

$$\Delta_+ = \Delta_-^{-1}. \tag{A.108}$$

The results of implies that Δ is represented by the exponential function

$$\Delta_+ = e^b, \tag{A.109}$$

and

$$\Delta_- = e^{-b}. \tag{A.110}$$

This result implies that we can write the linearly independent solutions ψ_i^1 satisfying

$$\begin{aligned} \psi_1^1(x+a) &= e^b \psi_1^1(x) \\ \psi_2^1(x+a) &= e^b \psi_2^1(x). \end{aligned} \tag{A.111}$$

Real values for b are forbidden as wavefunctions because $x \to \pm\infty$ and so we let $b = ika$ for $k \in \mathbb{R}$. Now we can write without the subscripts

$$\psi(x+a) = e^{\pm ka}\psi(x). \tag{A.112}$$

Since we have

$$\psi x = e^{ika}u(x), \tag{A.113}$$

we finally arrive at

$$u(x+a) = u(x). \tag{A.114}$$

Thus proving Bloch's theorem.

APPENDIX B

QUANTUM TO CLASSICAL WALK TRANSITIONS TUNED BY SPONTANEOUS EMISSIONS

This appendix includes a reprint of Ref. [24]: J. H. Clark, C. Groiseau, Z. N. Shaw, S. Dadras, C. Binegar, S. Wimberger, G. S. Summy, and Y. Liu, *Quantum to Classical Walk Transitions Tuned by Spontaneous Emissions*, Phys. Rev. Research **3**, 043062 (2021)

Quantum to classical walk transitions tuned by spontaneous emissions

J. H. Clark,[1] C. Groiseau,[2,3] Z. N. Shaw,[1] S. Dadras,[4] C. Binegar,[1] S. Wimberger,[5,6,*] G. S. Summy,[1,†] and Y. Liu[1,‡]

[1]*Department of Physics, Oklahoma State University, Stillwater, Oklahoma 74078, USA*
[2]*Dodd-Walls Centre for Photonic and Quantum Technologies, New Zealand*
[3]*Department of Physics, University of Auckland, Auckland 1010, New Zealand*
[4]*TOPTICA Photonics Inc., 5847 County Road 41, Farmington, New York 14424, USA*
[5]*Dipartimento di Scienze Matematiche, Fisiche e Informatiche, Università di Parma, Campus Universitario, 43124 Parma, Italy*
[6]*INFN–Sezione di Milano-Bicocca, gruppo collegato di Parma, 43124 Parma, Italy*

(Received 17 August 2021; accepted 4 October 2021; published 22 October 2021)

We have realized a quantum walk in momentum space with a rubidium spinor Bose-Einstein condensate by applying a periodic kicking potential as a walk operator and a resonant microwave pulse as a coin toss operator. The generated quantum walks appear to be stable for up to ten steps and then quickly transit to classical walks due to spontaneous emissions induced by laser beams of the walk operator. We investigate these quantum to classical walk transitions by introducing well-controlled spontaneous emissions with an external light source during quantum walks. Our findings demonstrate a scheme to control the robustness of the quantum walks and can also be applied to other cold atom experiments involving spontaneous emissions.

DOI: 10.1103/PhysRevResearch.3.043062

I. INTRODUCTION

Quantum walks (QWs) have been actively studied in many experimental systems, such as photons, lattice-confined atoms, and trapped ions, since the first theoretical model was introduced in 1993 [1–7]. Possessing spin degrees of freedom, spinor Bose-Einstein condensates (BECs) have also been suggested as ideal candidates for QW implementation [8]. Two important components of QWs are a walk operator to shift a walker in positions or momentum space and a coin toss operator to determine the direction that the walker shifts in each step [9]. In this work, a rubidium spinor BEC subjected to a series of periodic optical pulses, which can be described as an atom-optics kicked rotor, is utilized to create a QW in momentum space [10–13]. These periodic pulses construct one-dimensional optical lattices and act as a walk operator in momentum space. Resonant microwave pulses, entangling two hyperfine spin states, are the coin toss operator. In contrast to classical random walks with Gaussian distributions, QWs distribute ballistically because atoms conducting QWs can be in a superposition state [1,10,11]. Other advantages of QWs studied in this paper include hitting target points faster than classical walks, fast propagation, and entanglement between internal and external degrees of freedom [1,14]. QWs thus have many proposed and realized applications in various research fields including quantum information, metrology, and topological phenomena [15].

In this work, we demonstrate that quantum walks generated in momentum space can be stable for up to 10 steps and then quickly transit to classical walks due to spontaneous emission (SE) induced by the laser beams imprinting a momentum change. The SE effects have been observed in our previous experiments and are pervasive in other experiments utilizing atom-optics kicked rotors [16–18]. In principle, the SE effects could be inherently present in most experiments involving a quantum system and the impact of these effects on quantum measurements increases as the duration of the experiment increases. To better understand the SE effects, we investigate the SE-tuned quantum to classical walk transitions by introducing well-controlled SE events with an additional laser which does not interfere with the kick or shift laser used in our QW experiments. Those effects are manifold since SE acts as projective measurement in the internal electronic spin degree of freedom of the atom. On the other hand, SE has the twofold effect on the external center-of-mass degree of freedom of the atoms in our BECs: First, it changes the quasimomentum and hence the conditions of being in the QW or not, see Refs. [10,11], and, second, it biases the QW toward the direction of the ground state into which the electronic degree is projected. This is also contrary to previous experiments [16] with just one effective internal state in which SE only had an influence on the quantum-resonance condition and hence on the external degree of freedom. In our experiments, the probability of a SE event and the induced decoherence appear to increase with the evolution of time, i.e., with the number of steps in a QW. We also confirm the SE events lead to a biased momentum distribution, which agrees well with our numerical simulations. Our findings demonstrate a scheme to control the robustness

*sandromarcel.wimberger@unipr.it
†gil.summy1@gmail.com
‡yingmei.liu@okstate.edu

of quantum walks and can also be applied to other cold atom experiments involving spontaneous emissions [19,20].

II. THEORETICAL PREDICTIONS

Similarly to our previous works, we describe each QW step with an operator $\hat{\mathbf{U}}_{\text{step}} = \hat{\mathbf{T}}\hat{\mathbf{M}}$ [10,11]. A unitary walk operator $\hat{\mathbf{T}}$ implemented by atom-optics kicked rotors entangles the internal (i.e., spin) and external degrees of freedom, which leads to a momentum change of $p_m = m\hbar P_0$ [10–13]. Here P_0 is the wave vector of the one-dimensional lattice, $\hbar$ is the reduced Planck's constant, and m is an integer number. The coin operator $\hat{\mathbf{M}}$, created by a microwave pulse resonant with the transition between $|F = 1, m_F = 0\rangle$ and $|F = 2, m_F = 0\rangle$ states of ^{87}Rb atoms, produces a superposition of these two internal states. We apply a controlled amount of SE during a QW sequence using an independently controlled laser, which excites atoms from the $|F = 2\rangle$ ground state resonantly to the $|F' = 3\rangle$ excited state. The laser coupling $\Omega = \gamma\sqrt{\frac{I}{2I_s}}$ is small compared to the excited state hyperfine splitting between $|F' = 3\rangle$ and $|F' = 2\rangle$, so that the $|F = 2\rangle \rightarrow |F' = 2\rangle$ transition can be assumed to be too far detuned to create a significant population in $|F' = 2\rangle$. Here I is the intensity of the laser, I_s is the saturation intensity, and γ is the decay rate [21]. Due to selection rules, the atom can only decay from $|F' = 3\rangle$ back to $|F = 2\rangle$, corresponding to a projection of the atom onto $|F = 2\rangle$. The SE pulse is long enough that we can assume the atom reaches the steady state (the coin pulse should not interfere with that) meaning that the effective SE rate γ_{eff} is given by the natural line width times the steady-state population of $|F' = 3\rangle$ as follows [21],

$$\gamma_{\text{eff}} = \frac{\gamma}{2}\frac{I/I_s}{1 + I/I_s}, \tag{1}$$

from which we get the probability of a SE event per pulse

$$\rho = \gamma_{\text{eff}} t_{\text{SE}}. \tag{2}$$

Technically, γ_{eff} and ρ change during a single trajectory. The probability of the first decay overall and in each further decay has to be scaled down by a factor 2 since the atom will be either exactly or close to an equal superposition of the two ground states. So the given rate represents an upper limit, good only for a couple of microseconds after a SE event. We estimate $\rho \approx 0.35$ for a SE power of 3 μW for our experimental system, as elaborated in Sec. IV.

Since the SE light is introduced 30 μs after the start of the coin, SE events will interrupt the coin pulse at random times, the partial action of the coin operator in between two events of time delay t is

$$e^{i\frac{\pi t}{4T}\hat{\sigma}_x} = \begin{bmatrix} \cos\left(\frac{\pi t}{4T}\right) & i\sin\left(\frac{\pi t}{4T}\right) \\ i\sin\left(\frac{\pi t}{4T}\right) & \cos\left(\frac{\pi t}{4T}\right) \end{bmatrix}, \tag{3}$$

where T is the total length of the coin pulse.

This means that the state ψ of the internal degree of freedom at the end of the coin sequence is only determined by the time of the last SE event $t' \in [0.29, 0.58] \times T$ and thus given by

$$|\psi_{\text{int}}\rangle = \cos\left[\frac{\pi(T - t')}{4T}\right]|2\rangle + i\sin\left[\frac{\pi(T - t')}{4T}\right]|1\rangle. \tag{4}$$

Here $|1\rangle$ and $|2\rangle$ represent the two internal states, $|F = 1, m_F = 0\rangle$ and $|F = 2, m_F = 0\rangle$, respectively. Equation (4) clearly shows that SE creates an imbalance in the internal state of the atoms toward $|F = 2\rangle$, which gets transferred to the populations and results in a biased momentum distribution (see our simulations in Fig. 1). The initial external states in momentum space are given by

$$|\psi_{\text{ext}}\rangle = 1/\sqrt{2}(|n = 0\rangle + e^{i\phi}|n = 1\rangle). \tag{5}$$

Each SE event also affects the external degree of freedom by shifting the quasimomentum q by a random amount. Contrary to SE induced by the kicking beams [12], the atom does not incur any recoil from the absorption of a photon from the SE beam due to its perpendicular alignment to the walk axis. Note that SE is not only a phase scrambling because it affects both the internal (projection on to hyperfine levels) and external (shifting of the quasimomentum) degrees of freedom. Possible heating during the experiment is taken into account during these simulations by considering an initial distribution of the quasimomentum, Δ_q. This quasimomentum represents the distribution of the BEC and is selected to best represent the experimental conditions. Also, possible recoil from emission is taken into account in the theoretical model.

In our simulations, we draw up to three Poisson-distributed times and perform the partial coin operator from the largest time that is still inside the coin duration. We also add the corresponding amount of random recoil (here taken to be uniformly distributed). Typical simulation results for five-step quantum walks at two kicking strengths k are shown in Fig. 1, which clearly show transitions from quantum walks to classic walks as the SE probability ρ increases.

III. EXPERIMENTAL PROCEDURES

Each experimental sequence starts with a BEC of approximately 4×10^4 ^{87}Rb atoms at the $|F = 1, m_F = 0\rangle$ state. The BEC is then subjected to Bragg, walk operator kicking, and microwave pulses. A schematic outlining of the pulse sequences is shown in Fig. 2. The walk operator kicking pulse and Bragg pulse are realized with the same two counter-propagating laser beams that intercept on the BEC, although the Bragg pulse has a longer duration to drive the BEC into the state $|\psi_{\text{ext}}\rangle = 1/\sqrt{2}(|n = 0\rangle + e^{i\phi}|n = 1\rangle)$ [10,22]. We control populations of the two internal states $|1\rangle$ and $|2\rangle$ using the microwave (coin toss) pulses resonant with the $|1\rangle$ to $|2\rangle$ transition.

The standard QW of i number of steps is created with a sequence of pulses described by the operator $(\hat{\mathbf{U}}_{\text{step}})^i = [\hat{\mathbf{T}}\hat{\mathbf{M}}(\pi/2, -\pi/2)]^{i-1}[\hat{\mathbf{T}}\hat{\mathbf{M}}(\pi/2, \pi)]$. To ensure that the QW is symmetric the first coin pulse in the sequence is a Hadamard gate, which prepares the initial internal states as $\hat{\mathbf{M}}(\pi/2, \pi)|1\rangle = 1/\sqrt{2}(|1\rangle + |2\rangle)$. For the standard QWs in our experiments an additional phase offset is applied to the coin microwave pulses to cancel out a global phase that acts on the QW due to the kicking pulses [10,23]. A QW that has the proper phase offset is referred to as phase compensated.

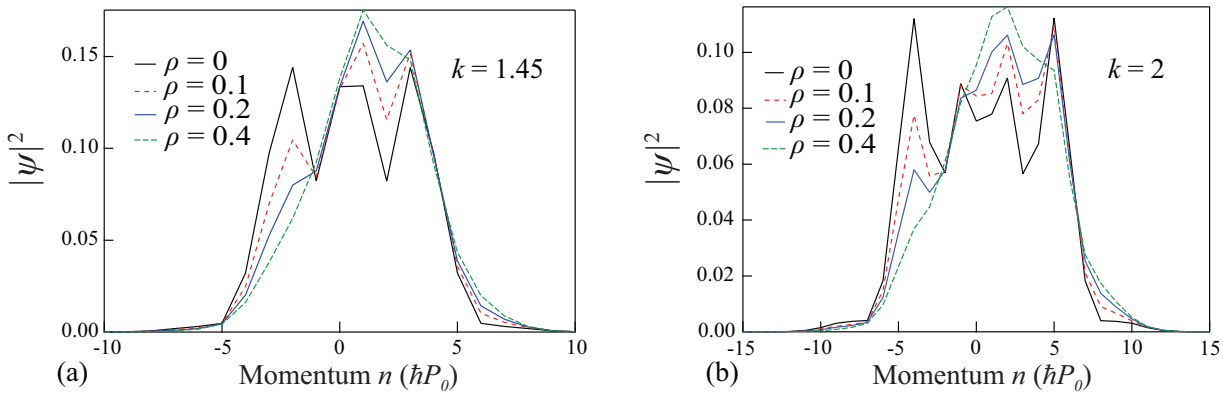

FIG. 1. Simulated momentum distributions of five-step quantum walks at two kicking strengths, $k = 1.45$ (a) and $k = 2.0$ (b), averaged over 10^3 trajectories with $\Delta_q = 0.025\ \hbar P_0$ at various SE probability ρ. Here Δ_q is the width of the quasimomentum q. Note the increasing asymmetry as the probability ρ increases.

During the coin toss pulses a SE light with a pulse duration of 30 μs is added to induce well-controlled SE effects onto the QW. A walk operator kicking pulse is then applied as the walk operator in momentum space followed by a coin toss microwave pulse. This coin toss pulse acts on the internal states to entangle the internal and external degrees of freedom. To avoid interfering with the walk operator kicking pulses, the SE pulses are set to apply only during the microwave coin pulses. This sequence of a coin toss pulse followed by a delta pulse is then repeated until QWs for i number of steps are recorded and time-of-flight images are taken via the standard absorption imaging method [10,23].

IV. RESULTS AND DISCUSSIONS

Figure 3 shows the effects of SE on a five-step QW in which the phase of the walk is noncompensated although the

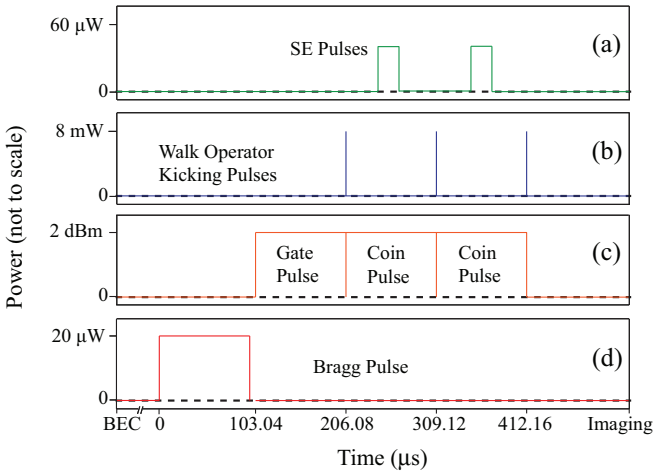

FIG. 2. Schematic diagram showing the sequence of various optical and microwave pulses used in our experiments. (a) The sequence of SE pulses each with a duration of 30 μs. (b) The sequence of the walk operator kicking pulses. (c) The sequence of the Hadamard gate and coin toss microwave pulses. The time duration of each of these pulses is 103.04 μs. (d) The sequence of the Bragg pulse with a duration of 103.04 μs. Axes are not to scale.

phase of the microwave pulses is held constant throughout the data run. The walk operator kicking pulse strength during the noncompensated QWs is kept at $k = 1.45$, which has been proved to yield ideal QWs [10,23]. The time-of-flight images shown in Fig. 3(a) indicate that the population of the atoms shifts toward the positive momentum states as the SE probability ρ increases. This observation confirms the prediction of Fig. 1, i.e., SE creates an imbalance in the internal state of the atoms toward the $|2\rangle$ state leading to a biased momentum distribution because the projection of the $|2\rangle$ state moves in the direction of positive momenta. This shift in momentum is quantitatively analyzed in Fig. 4(c). In addition, the overall population of atoms present also decreases as ρ increases. The effective decay rate of the QW is estimated from the observed exponential atom losses as ρ increases [see the solid lines in Fig. 3(b) and Fig. 3(c)]. A typical example of our SE calibrations is shown in Fig. 3(c) which plots the condensate fraction of a BEC versus the duration of a single SE pulse at a fixed SE power of 3 μW. The BEC is first prepared in the $F = 2$ state before being subjected to a SE pulse of light increasing in 50-μs intervals. The exponential fitting of this data indicates that the probability of SE events at this power is $\rho = 0.35$, as shown in Fig. 3(c).

We repeat the above experiment with a properly compensated QW generated at a higher kicking strength of $k \simeq 2$ to ensure that the QW distribution is broader than those created with the lower kicking strength. We scan the SE probability up to $\rho = 0.84$ with an average of eight runs per power setting. The observed distribution of the QWs does not show noticeable differences beyond this ρ value. Typical time-of-flight images of the compensated QWs are shown in Fig. 4(d), which indicate that the atoms in the compensated walks also shift toward the positive momentum states as the SE probability ρ increases. The decay of the QW distribution can be more easily discerned from the momentum distributions, as displayed in Figs. 4(a) and 4(b). We also extract the mean momentum and mean energy from the noncompensated and compensated QW data, and respectively show them as a function of the SE probability ρ in Fig. 4(c) and Fig. 4(e). A positive shift in the mean momentum as the SE pulses become more powerful is confirmed in Fig. 4(c) for both compensated and noncompensated QWs. In the case of the compensated QWs the mean

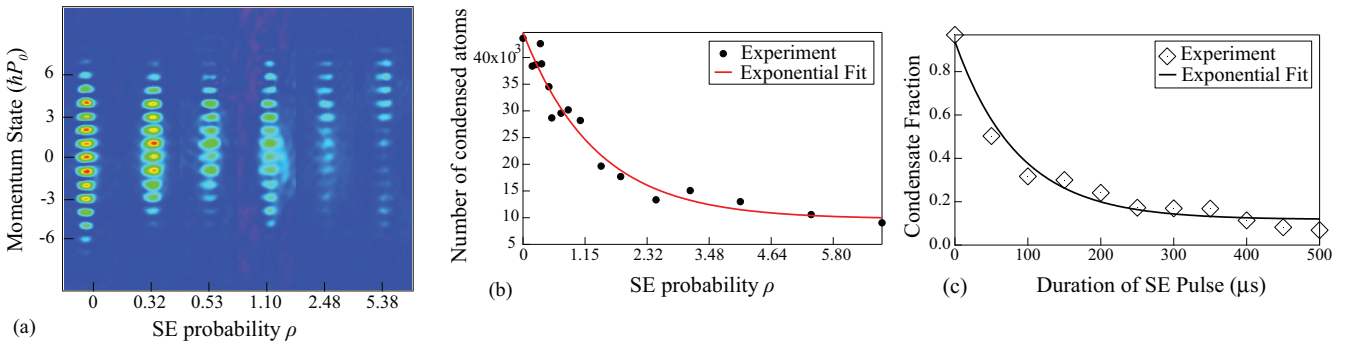

FIG. 3. (a) Time-of-flight images of a phase noncompensated five-step QW under various SE probability ρ at the kicking strength $k = 1.45$ and the SE pulse duration of 30 μs. (b) The number of condensed atoms versus ρ in the noncompensated QWs shown in panel (a). (c) The condensate fraction versus SE pulse duration for a single BEC subjected to a pulse of SE light with a power of 3.0 μW. Solid lines in panel (b) and panel (c) are exponential fits (see text).

momentum is initially negative due to the phase of the applied microwave coin pulses being larger than 2π thus causing an initial bias toward negative mean momentum. For a standard QW in our experiments this phase on the coin microwave pulses is normally below $(2k + \pi)$ to cancel out a global phase that acts on the QW due to the kicking pulses [10,23]. Although this bias can adversely affect the momentum distribution of a QW that evolves in time, it does not prevent the observation of the positive shift in mean momentum as the SE probability ρ increases. This is because the same microwave coin phase is applied throughout an experiment as the SE probability is scanned. On the other hand, Fig. 4(e) implies the mean energy remains constant for the compensated QWs as the SE probability ρ increases within the range of 0 to 0.85, which agrees with our simulations shown in Fig. 5(b).

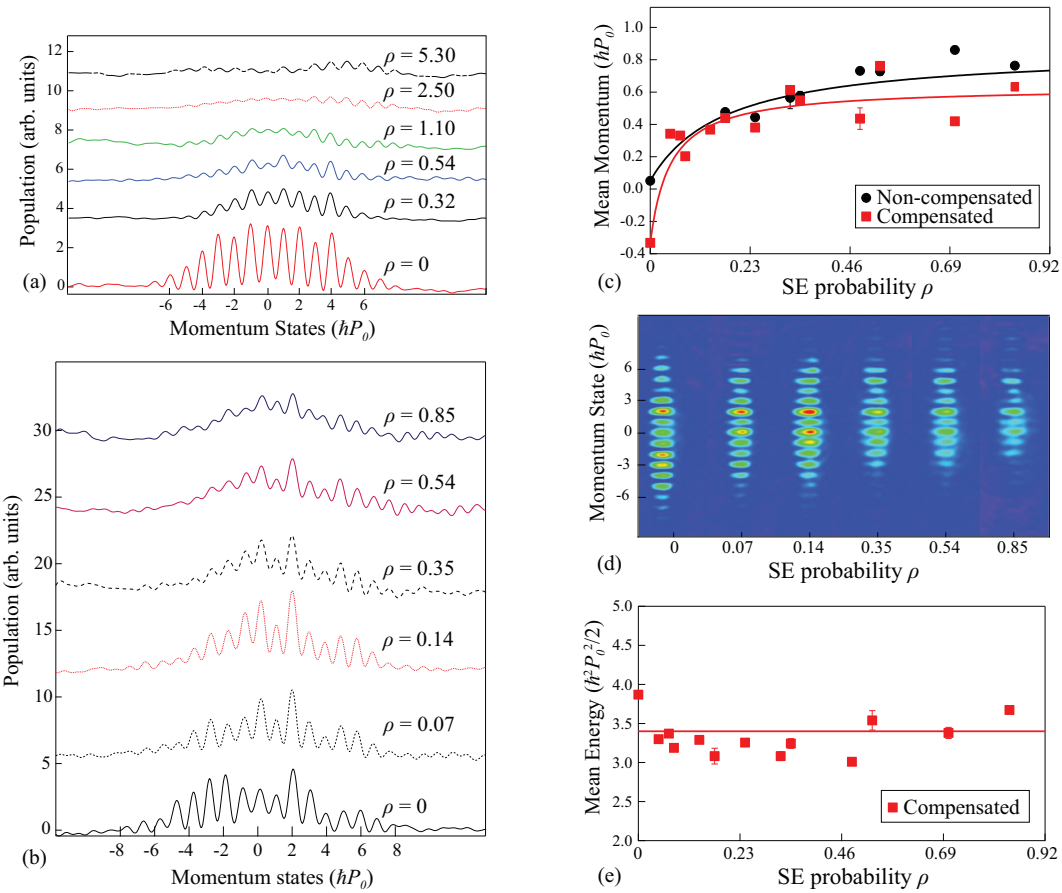

FIG. 4. Typical momentum distributions of (a) a phase noncompensated five-step QW and (b) a phase compensated five-step QW at various ρ and at a fixed SE pulse duration of 30 μs (see text). Each momentum distribution is vertically shifted by a constant offset for visual clarity. (c) The mean momentum extracted from panels (a) and (b) as a function of ρ. (d) Typical time-of-flight images in the compensated QWs. (e) The mean energy extracted from panel (b) versus ρ. Solid lines in panel (c) and panel (e) are fitting curves to guide the eye.

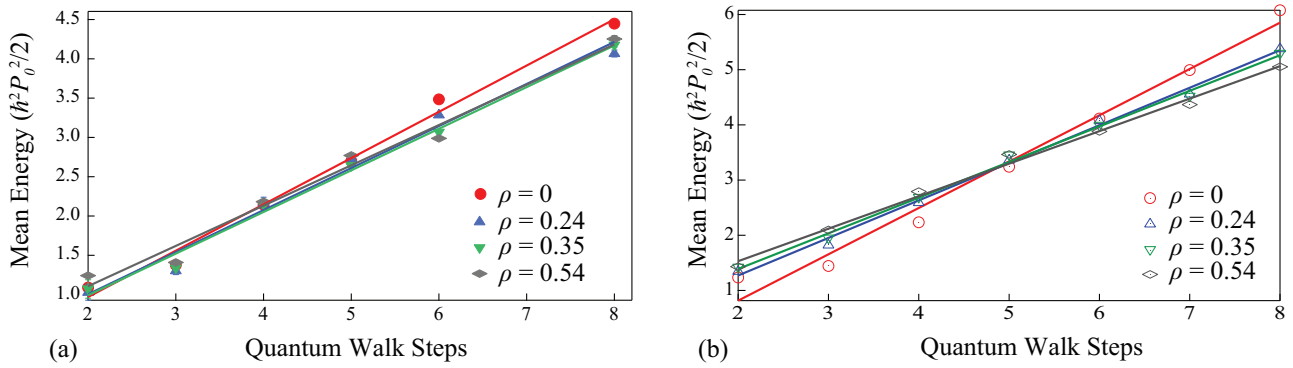

(c)

SE Probability	Experimental Rate R	Theoretical Rate R
$\rho = 0$	0.58	0.84
$\rho = 0.24$	0.53	0.68
$\rho = 0.35$	0.52	0.64
$\rho = 0.54$	0.51	0.58

FIG. 5. (a) The extracted mean energy as a function of the QW steps at various SE probability ρ and $k = 1.4$. (See text.) (b) Theoretical predictions based on the experimental conditions for the data shown in panel (a). The solid lines in both panels represent the linear fitting functions. (c) Rate R extracted from panel (a) and panel (b) (see text).

Our data in Fig. 3 and Fig. 4 indicate that the quantum to classical walk transitions happen at around $\rho = 0.58$, much lower than the maximum SE probability studied in this paper. To clearly demonstrate the transition of walks from displaying quantum to classical behaviors under the applied SE pulses, we conduct similar experiments on walks of various numbers of steps. For each step, the kicking strength is kept at $k = 1.4$ to reduce the probability of extra SE events induced by the kicking beams. The mean energy extracted from these experiments is plotted as a function of the QW steps for various ρ in Fig. 5(a), which shows that the mean energy increases with increasing number of steps at a rate R. Each data set in Fig. 5(a) is fit with a linear function and the rate R is calculated and tabulated in Fig. 5(c). The rate R appears to increase as ρ reduces and reach the largest value at $\rho = 0$, as shown by the red markers in Fig. 5(a) and in Fig. 5(c). Our observations shown in Fig. 5 agree well with a predicted signature of quantum to classical walk transitions, i.e., QWs have larger mean energy than classical walks at a given step because QWs distribute ballistically while classical walks follow Gaussian distributions [1,10,11]. Figure 5 thus indicates that the QWs gradually transit to classical walks with less mean energy as the applied SE effect becomes powerful enough to destroy the entanglement of the two internal spin states. These results suggest that the rate R could potentially be used as a good indicator for the quantum to classical walk transitions especially if only small numbers of walk steps are achievable. We also conduct theoretical simulations using similar parameters and typical simulation results are shown in Fig. 5(b) and Fig. 5(c). These simulations confirm that the rate R reduces as the SE probability ρ increases, leading to an increased difference in the mean energy among simulated data taken under various ρ at a high-enough step, as clearly demonstrated by the six-step and eight-step data in Fig. 5(b). Good theory-experiment agreements demonstrated in Fig. 5 thus suggest that the rate R can be an observable to quantify quantum to classical walk transitions. Figure 5 also shows that QWs are able to maintain their robustness when the number of steps is lower than five.

V. CONCLUSIONS AND OUTLOOK

We have presented quantum to classical walk transitions tuned by spontaneous emissions. The SE rate is derived from the observed atom losses during QWs. We have demonstrated that the addition of the SE light yields quantum to classical walk transitions and leads to biased momentum distributions, which can be well explained by our numerical simulations in both the compensated and noncompensated QWs. Our findings suggest a scheme to control the robustness of the quantum walks and demonstrate that the effects of the SE light are intrigue. While a SE event acts as a projective measurement on the internal spin degree of freedom, its effect on the external motion, that is the actually observed quantity, is direct by a change of the necessary resonance conditions for the QW, but also indirect since the motion becomes biased into the direction into which the ground state likes to move. Hence, for the center of mass of our atoms, SE is not a strong but rather a weak form of quantum measurement, with the internal state acting as an ancilla that is actually strongly measured. Many SE events will then necessarily have a larger effect than just one SE event since they bias more the walk into one direction of the external motion. Similar ideas have been put forward, e.g., in Ref. [24]. In conclusion, our results open further possibilities of utilizing the tunable SE light to engage on the theory of measurements in experimentally easily accessible quantum systems.

ACKNOWLEDGMENT

We thank the Noble Foundation for financial support.

[1] J. Wang and K. Manouchehri, *Physical Implementation of Quantum Walks* (Springer, Berlin, 2014).
[2] W. Dur, R. Raussendorf, V. Kendon, and H.-J. Briegel, Quantum walks in optical lattices, Phys. Rev. A **66**, 052319 (2002).
[3] K. Eckert, J. Mompart, G. Birkl, and M. Lewenstein, One- and two-dimensional quantum walks in arrays of optical traps, Phys. Rev. A **72**, 012327 (2005).
[4] H. Schmitz, R. Matjeschk, C. Schneider, J. Glueckert, M. Enderlein, T. Huber, and T. Schaetz, Quantum Walk of a Trapped Ion in Phase Space, Phys. Rev. Lett. **103**, 090504 (2009).
[5] M. Karsk, L. Forster, J. Choi *et al.*, Quantum walk in position space with single optically trapped atoms, Science **325**, 174 (2009).
[6] Y. Aharonov, L. Davidovich, and N. Zagury, Quantum random walks, Phys. Rev. A **48**, 1687 (1993).
[7] A. Alberti and S. Wimberger, Quantum walk of a Bose-Einstein condensate in the Brillouin zone, Phys. Rev. A **96**, 023620 (2017).
[8] C. M. Chandrashekar, Implementing the one-dimensional quantum (Hadamard) walk using a Bose-Einstein condensate, Phys. Rev. A **74**, 032307 (2006).
[9] J. Kempe, Quantum random walks-an introductory overview, Contemp. Phys. **44**, 307 (2003).
[10] S. Dadras, A. Gresch, C. Groiseau, S. Wimberger, and G. S. Summy, Experimental realization of a momentum-space quantum walk, Phys. Rev. A **99**, 043617 (2019).
[11] S. Dadras, A. Gresch, C. Groiseau, S. Wimberger, and G. S. Summy, Quantum Walk in Momentum Space with a Bose-Einstein Condensate, Phys. Rev. Lett. **121**, 070402 (2018).
[12] C. Groiseau and S. Wimberger, Spontaneous emission in quantum walks of a kicked Bose-Einstein condensate, Phys. Rev. A **99**, 013610 (2019).
[13] N. Shenvi, J. Kempe, and K. Birgitta Whaley, Quantum random-walk search algorithm, Phys. Rev. A **67**, 052307 (2003).
[14] R. Portugal, *Quantum Walks and Search Algorithms* (Springer, Berlin, 2018).
[15] J. K. Asboth, Symmetries, topological phases, and bound states in the one-dimensional quantum walk, Phys. Rev. B **86**, 195414 (2012).
[16] M. B. d'Arcy, R. M. Godun, G. S. Summy, I. Guarneri, S. Wimberger, S. Fishman, and A. Buchleitner, Decoherence as a probe of coherent quantum dynamics, Phys. Rev. E **69**, 027201 (2004).
[17] M. B. d'Arcy, R. M. Godun, M. K. Oberlather, G. S. Summy, and K. Burnett, Approaching classicality in quantum accelerator modes through decoherence, Phys. Rev. E **64**, 056233 (2001).
[18] R. K. Shrestha, J. Ni, W. K. Lam, G. S. Summy, and S. Wimberger, Dynamical tunneling of a Bose-Einstein condensate in periodically driven systems, Phys. Rev. E **88**, 034901 (2013).
[19] S. Chai and M. F. Andersen, Enhancing survival resonances with engineered dissipation, Phys. Rev. Research **2**, 033194 (2020).
[20] S. Chai, J. Fekete, and M. F. Andersen, Measuring the local gravitational field using survival resonances in a dissipatively driven atom-optics system, Phys. Rev. A **98**, 063614 (2018).
[21] Daniel A. Steck, Rubidium 87 D Line Data, available online at http://steck.us/alkalidata (revision 2.2.2, 9 July 2021).
[22] Y. Torii, Y. Suzuki, M. Kozuma, T. Sugiura, T. Kuga, L. Deng, and E. W. Hagley, Mach-Zehnder Bragg interferometer for a Bose-Einstein condensate, Phys. Rev. A **61**, 041602(R) (2000).
[23] S. Dadras, Discrete-time quantum walk of a Bose-Einstein condensate in momentum space, Ph.D. thesis, Oklahoma State University, 2018.
[24] B. Tamir and E. Cohen, Introduction to weak measurements and weak values, Quanta **2**, 7 (2013).

APPENDIX C

LIGHT-SHIFT-INDUCED BEHAVIORS OBSERVED IN MOMENTUM-SPACE QUANTUM WALKS

This appendix includes a reprint of Ref. [14]: N. Bolik, C. Groiseau, J. H. Clark, A. Gresch, S. Dadras, G. S. Summy, Y. Liu, and S. Wimberger *Light-shift-induced behaviors observed in momentum-space quantum walks*, Phys. Rev. A **106**, 033307 (2022)

Light-shift-induced behaviors observed in momentum-space quantum walks

Nikolai Bolik,[1] Caspar Groiseau,[2] Jerry H. Clark,[3] Alexander Gresch,[4] Siamak Dadras,[5] Gil S. Summy,[3,6] Yingmei Liu,[3,*] and Sandro Wimberger[7,8,†]

[1]*Institute of Theoretical Physics, Heidelberg University, Philosophenweg 16, 69120 Heidelberg, Germany*
[2]*Departamento de Física Teórica de la Materia Condensada and Condensed Matter Physics Center (IFIMAC), Universidad Autónoma de Madrid, 28049 Madrid, Spain*
[3]*Department of Physics, Oklahoma State University, Stillwater, Oklahoma 74078-3072, USA*
[4]*Quantum Technology Research Group, Heinrich Heine University Düsseldorf, Universitätsstraße 1, 40225 Düsseldorf, Germany*
[5]*TOPTICA Photonics Inc., 5847 County Road 41, Farmington, New York 14424, USA*
[6]*Airy3D, 5445 Avenue de Gaspé Suite 230, Montréal, Québec H2T 3B2, Canada*
[7]*Dipartimento di Scienze Matematiche, Fisiche e Informatiche, Università di Parma, Parco Area delle Scienze 7/A, 43124 Parma, Italy*
[8]*INFN, Sezione di Milano Bicocca, Gruppo Collegato di Parma, Parco Area delle Scienze 7/A, 43124 Parma, Italy*

(Received 5 May 2022; accepted 19 August 2022; published 7 September 2022)

Over the last decade there have been many advances in studies of quantum walks (QWs) including a momentum-space QW recently realized in our spinor Bose-Einstein condensate system. This QW possessed behaviors that generally agreed with theoretical predictions; however, it also showed momentum distributions that were not adequately explained by the theory. We present a theoretical model which proves that the coherent dynamics of the spinor condensate is sufficient to explain the experimental data without invoking the presence of a thermal cloud of atoms as in the original theory. Our numerical findings are supported by an analytical prediction for the momentum distributions in the limit of zero-temperature condensates. This current model provides more complete explanations to the momentum-space QWs that can be applied to study quantum search algorithms and topological phases in Floquet-driven systems.

DOI: 10.1103/PhysRevA.106.033307

I. INTRODUCTION

Quantum walks (QWs) have been under intensive investigation over the last two decades since they can outrun classical algorithms for many practical problems [1–3]. For example, the Grover search algorithm may be viewed as a quantum walk algorithm [2]. Due to quantum interference of various passes during quantum walks, they exhibit quite different features when compared to their classical counterpart for which, in contrast, randomness and stochasticity play a crucial role [1]. Similar to classical random walks there are essentially two types of quantum analogs: discrete-time and continuous-time quantum walks. In contrast to the latter, an additional coin degree of freedom characterizes the former, where the state of the coin determines the walker's direction in the next step.

We apply a theoretical model to the discrete-time quantum walk implemented in our previous works [4–6] with spinor Bose-Einstein condensates (BECs), consisting of ^{87}Rb atoms with an internal spin-$\frac{1}{2}$ degree of freedom. In contrast to most other experimental realizations [7–23], this QW occurs in quantized momentum space due to time-periodic kicks applied to the condensate. The experiments in Refs. [4–6] used the two ground-state Zeeman sublevels $|F = 1, m_F = 0\rangle$ and $|F = 2, m_F = 0\rangle$ of a Rubidium BEC to form an effective spin-$\frac{1}{2}$ system. The BEC is periodically subjected to pulses of standing-wave light generated by a laser tuned between the two ground states and a third excited level. The underlying description is that of the atom-optics kicked rotor (AOKR) as described in Refs. [24,25], whose Hamiltonian is

$$\hat{\mathcal{H}} = \frac{1}{2}\hat{p}^2 + k\cos(\hat{\theta}) \sum_{j=-\infty}^{\infty} \delta(t - j\tau). \tag{1}$$

Here, $\hat{p}$ and $\hat{\theta}$ represent the momentum and (angular) position operators, respectively, while k is the strength of the laser kick and τ the time delay between consecutive pulses. Since the experiment is performed in a periodic lattice potential, we resort to Bloch's theorem to arrive at the angle description above. This necessitates the introduction of a dimensionless quasimomentum $\beta \in [0, 1)$. The width of the Gaussian-like quasimomentum distribution is experimentally given by the initial temperature of the BEC, where, e.g., a BEC at zero temperature would correspond to a fully resonant system with $\beta = 0$ for all atoms. The typical value of the width of the β distribution in our experimental system is of the order of a few percent in the Brillouin zone, i.e., $\beta_{\mathrm{FWHM}} \approx 0.025$.

The evolution during one period τ is then described by the following Floquet operator:

$$\hat{\mathcal{U}} = \hat{\mathcal{U}}_{\mathrm{f}}\hat{\mathcal{U}}_{\mathrm{k}} = e^{-i\tau\frac{\hat{p}^2}{2}} e^{-i\hat{\sigma}_z k\cos(\hat{\theta})}, \tag{2}$$

*yingmei.liu@okstate.edu
†sandromarcel.wimberger@unipr.it

which factorizes into a free evolution $\hat{\mathcal{U}}_{\rm f}$ and kick operator $\hat{\mathcal{U}}_{\rm k}$. Since $p = n + \beta$, with integer (quantized angula) momenta n, the free evolution equals the identity in quantum resonance conditions, i.e., for an evolution corresponding to a full Talbot time $\tau = 4\pi$ and $\beta = 0$. Under these resonance conditions, the atoms move ballistically in momentum space, i.e., their momenta increase linearly with the number of applied kicks [25,26].

Because the kicking laser is detuned exactly between the two internal ground states [4,6], the potential felt by the two states is identical in size but opposite in sign, which reflects the $\hat{\sigma}_z$ Pauli matrix. The latter fact models a quantum walk whose direction in each step depends on the internal coin state. There is an important difference between our AOKR quantum walk and an ideal quantum walk as defined, e.g., in Ref. [1]. In the latter at any step of the walk a certain position of the walker only couples to the nearest-neighbor positions, while in the AOKR quantum walks the coupling to other momentum classes is given by matrix elements which are Bessel functions of the first kind [6]. *A priori*, both internal states would see the same evolution due to the kicks, i.e., they would move symmetrically under the AOKR evolution. To break this symmetry in the coupling, we use a ratchet effect imposed by an appropriate choice of the initial condition in the walker's space. Those ratchet states are a superposition of at least two neighboring momenta with a relative phase of $e^{i\pi/2}$, i.e.,

$$|\psi_{\rm R}\rangle = \frac{1}{\sqrt{S}} \sum_s e^{is\pi/2} |n = s\rangle \,, \tag{3}$$

where S is the total number of involved momentum classes denoted by s. Such initial states can be generated experimentally via Bragg pulses [27,28]. The mean momentum transfer to individual states depends on the sign of the kicking potential that is different for the two internal states, as shown by $\hat{\mathcal{U}}_{\rm k}$ in Eq. (2) [25,29,30]. It turns out to be of crucial importance that for larger number S in Eq. (3) less dispersion occurs in the directed kicking [27,28]. Hence, the best correspondence to an ideal quantum walk is found for large $S \geqslant 3$, while for $S = 2$ differences from ideal walks are visible in the central part of the walker's probability distribution [31].

The coin operator is realized by a Rabi coupling between the two internal states of the atoms. This coupling is mediated by resonant microwave (MW) pulses, inducing a unitary rotation on the Bloch sphere given by

$$\hat{M}(\alpha, \chi) = \begin{pmatrix} \cos\left(\frac{\alpha}{2}\right) & e^{-i\chi} \sin\left(\frac{\alpha}{2}\right) \\ -e^{i\chi} \sin\left(\frac{\alpha}{2}\right) & \cos\left(\frac{\alpha}{2}\right) \end{pmatrix}, \tag{4}$$

where α and χ are real angles. An additional $\hat{\sigma}_z$ rotation is implementable by an accessible third angle that was not considered in Refs. [4,6,31] and will also not be considered in this paper. The experimental QWs in Ref. [4–6] were described by the following sequence of unitary operations:

$$\hat{\mathcal{U}}^j_{\rm step} = [\hat{\mathcal{U}}\hat{Y}]^j \hat{\mathcal{U}}\hat{W}, \tag{5}$$

realizing $j \in \mathbb{N}$ steps of the walk applied to an initial state expressed by Eq. (3). Here

$$\hat{W} = \hat{M}\left(\frac{\pi}{2}, 0\right) = \frac{1}{\sqrt{2}} \begin{pmatrix} 1 & 1 \\ -1 & 1 \end{pmatrix} \tag{6}$$

and

$$\hat{Y} = \hat{M}\left(\frac{\pi}{2}, -\frac{\pi}{2}\right) = \frac{1}{\sqrt{2}} \begin{pmatrix} 1 & i \\ i & 1 \end{pmatrix} \tag{7}$$

are two different coins that initialize and execute the walk, respectively. It is important that the two coins must be different in order to guarantee a symmetric evolution of the walker (see Ref. [1]). The kick strength on the order of $k \approx 1.5$ proves to resemble well an ideal walk with only nearest neighbor couplings [4–6,31]. For example, the experiments reported in Refs. [4–6] used $k = 1.2$, $k = 1.45$, and $k = 1.8$. After j steps, the momentum distribution of both internal states is measured using the standard absorption imaging procedure to yield the final observable $P(n, j) = P_{|1\rangle}(n, j) + P_{|2\rangle}(n, j)$. Note that all the experimental realizations so far implemented walks with only $S = 2$, e.g., an initial ratchet state of the form

$$|\psi_{\rm R}\rangle = \frac{1}{\sqrt{2}}(|n = 0\rangle + i\,|n = 1\rangle). \tag{8}$$

Numerical simulations of the walk given by Eq. (5) showed a good resemblance to the ideal quantum walk [31], with ballistically moving side peaks and little probability at the center around $n = 0$. However, the experiments observed a large nonvanishing part of the momentum distribution that stayed close to $n = 0$ throughout the entire evolution of up to $j = 15$ steps [4–6]. This observation was initially explained in Ref. [4] by a rather large residual thermal atomic cloud that would make up about 10% to 15% of all the measured atoms. A thermal cloud would correspond to much hotter atoms uniformly distributed across the entire Brillouin zone $\beta \in [0, 1)$. All nonresonant quasimomenta ($\beta \neq 0$) essentially do not respond to the kicks and hence will move little and not contribute at all to the expected ballistic flanks in the distribution. In this paper we suggest a more complete theoretical interpretation of the experimental data, not involving a thermal cloud but based on the concurrence of a sequence of effects that resulted in a deviation of the experimentally measured walks from the theoretical expectation. These effects include a different choice of the phase angle χ in Eq. (4) and the specific form of the ratchet initial state in Eq. (8), both reflecting the fact that we are dealing with an AOKR quantum walk. Note that residual peaks at low momenta observed in the AOKR quantum walk would not appear in an ideal quantum walk.

II. THEORETICAL MODEL

A. Theory of the light shift

The physical explanation is based on the additional light shift that starts playing a role in the spinor AOKR, described in detail in Refs. [32,33]. For clarity of the argument, we shall briefly present its origin here.

During a kick, the dynamics of the standard AOKR are described by interaction terms between the ground and excited

state of the form

$$\hat{H}_{\rm int} = \frac{\Omega}{2}|g\rangle\langle e|\cos\left(\frac{\hat{\theta}}{2}\right)e^{i\Delta t} + \text{H.c.}, \tag{9}$$

where Δ is the detuning and Ω the Rabi frequency of the laser.

The effective dynamics obtained after adiabatically eliminating the excited state are described by an AC-Stark shift of the ground states $|g\rangle$ from the coherent drive of the kicking laser, i.e.,

$$\hat{H}_{\rm eff} = \frac{\Omega^2}{8\Delta}|g\rangle\langle g|(\cos(\hat{\theta}) + 1), \tag{10}$$

where we used $\cos^2\frac{\theta}{2} = \frac{1}{2}(\cos\theta + 1)$ and the rate corresponds to the kick strength before the time integration over the duration of the kick pulse τ_p, e.g. $k = \frac{\Omega^2}{8\Delta}\tau_p$.

In the standard AOKR this constant offset (term with no $\cos\theta$-dependence) can be disregarded as there is only a single level. In our spinor AOKR, after the adiabatic elimination of the excited state, two ground states remain, each with such an AC-Stark shift (of opposite sign due to opposite detuning). Transitions between the two ground states can get discarded in rotating wave approximation. Thus, we are left with

$$\hat{H}_{\rm eff} = \frac{\Omega^2}{8\Delta}\hat{\sigma}_z(\cos(\hat{\theta}) + 1), \tag{11}$$

and effectively we have an additional energy difference or light shift between the two ground states which can no longer be discarded.

B. Light-shift compensation in the experiment

As just introduced and shown in full detail in Refs. [32,33], the Hamiltonian for an AOKR with two different internal states contains an additional constant AC-Stark shift [34] between the two energy levels. Comparing the physically effectively implemented Hamiltonian from Eq. (11) with the QKR-Hamiltonian from Eq. (1), this light shift induces a phase whenever a kick is applied, giving an effective kick of the form

$$\hat{\mathcal{U}}_{\rm k,eff} = e^{-i\hat{\sigma}_z k(1+\cos(\hat{\theta}))}. \tag{12}$$

This means that there is a relative phase of $2k$ for each application of the kick operator, i.e., for each step of the walk. This light-shift phase needs to be compensated in the experiment since it would lead to a different evolution with respect to the theoretical prediction [note that the new terms in Eq. (12) would adversely affect the phase evolution in the internal degree of freedom changing the overall interference pattern]. A compensation with a $\hat{\sigma}_z$ phase gate with a third Bloch angle $\gamma = k$ by an additional MW pulse would be possible. The experiments reported in Refs. [4–6], however, used the phase χ of Eq. (4) as a free parameter in order to best compensate the light shift phase. Several runs were made for various choices of χ and finally the value, with which the walk was most symmetric around $n = 0$, was used in all other experiments in Refs. [4–6]. The absolute value of χ as well as a possibly present third Bloch angle γ were under limited experimental control, and the aforementioned compensation procedure seemed to make this fact irrelevant.

The experiments may have, for instance, easily exchanged the coin $\hat{Y}$ by the coin $\hat{G}_H$ in the walk, effectively resulting in a new sequence, e.g.,

$$\hat{\mathcal{U}}^j_{\rm step} = [\hat{\mathcal{U}}\hat{G}_{\rm H}]^j\hat{\mathcal{U}}\hat{Y}, \tag{13}$$

The $\hat{Y}$ and $\hat{G}_H$ curves in Fig. 1(a) show that such an exchange of the two coins indeed has dramatic effects on the quality of the walk. The operator $\hat{G}_H$ is the Hadamard gate defined as [6]

$$\hat{G}_{\rm H} = \frac{1}{\sqrt{2}}\begin{pmatrix}1 & 1\\ 1 & -1\end{pmatrix}. \tag{14}$$

While momentum distributions of the QWs represented by Eqs. (13) and (5) are mirror symmetric around $n = 0$ since both coins are perfectly balanced (all giving unbiased walks), the actual final distributions look very different. Assuming that only a MW pulse expressed by Eq. (4) was applied as stated in Refs. [4–6] with $\alpha = \pi/2$ fixed, the combined effect of a MW pulse and the light shift could have been of the form

$$\hat{M}\left(\frac{\pi}{2}, \chi\right)e^{-ik\hat{\sigma}_z} = \frac{1}{\sqrt{2}}\begin{pmatrix}e^{-ik} & e^{-i(\chi+k)}\\ -e^{i(\chi-k)} & e^{ik}\end{pmatrix} \tag{15}$$

$$= \frac{e^{-ik}}{\sqrt{2}}\begin{pmatrix}1 & e^{-i(\chi-2k)}\\ -e^{i\chi} & e^{i2k}\end{pmatrix}. \tag{16}$$

In the last step we extracted a global phase e^{-ik} that is not important for the following discussion. Generally, the phase χ cannot fully remove the effect of the light shift phase here. The quantum walk can, however, still be made symmetric around $n = 0$ by the choice $\chi = 2k = \pi \mod (2\pi)$, which would yield an effective MW operation. Hence, the aforementioned swapping of the two different coin operators could have occurred in the experiments. For example, with a kick strength of $k \approx 1.5$ the light shift phase gives a value close to $2k \approx \pi$ [see Eq. (7)]. Small deviations from the condition for $1.2 < k < 1.8$ appear not to change the global picture, as will be later shown in more detail in Sec. II F. In that sense, the light-shift and its experimentally incomplete compensation is the physical reasoning for the potentially implemented sequence from Eq. (13).

C. Alternative MW pulse: Hadamard gate

We have just seen that the actually implemented MW pulses in the experiment may be close to Hadamard gates $\hat{G}_{\rm H}$. In contrast to the original $\hat{W}$ pulses, $\hat{G}_{\rm H}$ pulses have the minus sign on the diagonal. Both pulses, however, are completely unbiased leading to walks with sidepeaks moving symmetrically outwards in a ballistic manner. We find that the difference in the signs of $\hat{W}$ and $\hat{G}_H$ matrix elements has no consequence for an ideal quantum walk with just nearest-neighbor couplings. For our AOKR walks, however, the different sign induces significantly different behavior. Figure 1(a) shows a numerical example derived for a perfectly resonant walk ($\beta = 0$). Our simulation results for the here proposed QW [see Eq. (13)] clearly indicate that the bulk of its momentum distributions has a larger probability to remain in the center ($n = 0$), as shown by the black curve in Fig. 1(a).

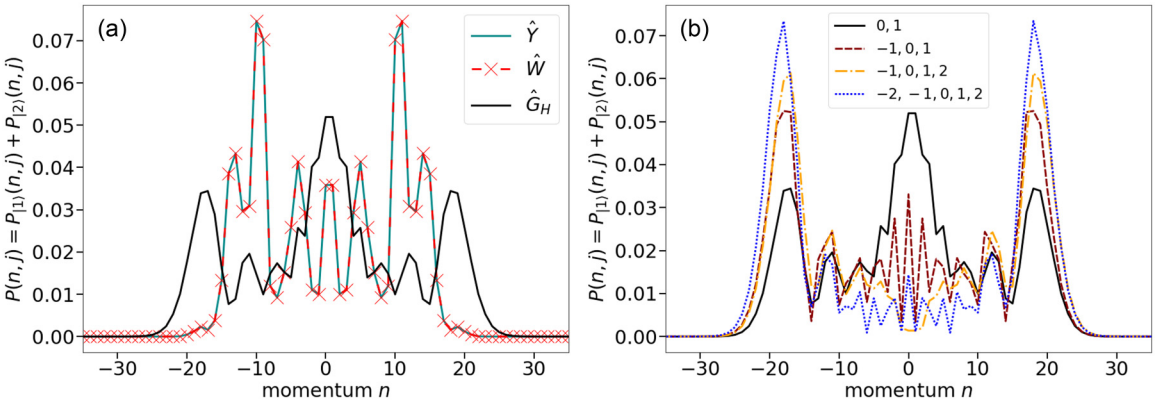

FIG. 1. The walker's distributions are shown after $j = 20$ steps for an AOKR discrete-time quantum walk. The kick strength is set at the experimental value $k = 1.45$. In (a) different walk protocols are shown. The distributions are computed by evolving the initial state in momentum space given by Eq. (8). The label $\hat{Y}$ resembles the walk that is initialized by $\hat{W}$ and the evolution is executed with the $\hat{Y}$ coin. $\hat{W}$ and $\hat{G}_H$ are initialized by the $\hat{Y}$ coin and then their respective walk is executed by $\hat{W}$ or $\hat{G}_{\mathrm{H}}$. $\hat{Y}$ and $\hat{W}$ produce the same momentum distributions for all times. The AOKR walks in (b) are implemented by the $\hat{Y}$ coin and executed by the $\hat{G}_{\mathrm{H}}$ coin. The different labels denote the momentum classes included in the initial state, as denoted by s in Eq. (3). The broader the initial state is in momentum space, the more the peak in the central region vanishes. One should remember that only the state expressed by Eq. (8) (solid black line) was experimentally implemented in Refs. [4–6].

D. Initial-state dependence

As described previously, an important difference between an ideal quantum walk and the AOKR walks discussed in this paper are the initial states in the walker's space [4]. The initial state experimentally implemented was expressed by Eq. (8) with two involved momenta. As described in Refs. [27–30], the state is constructed to be concentrated in position space at the rising (falling) flanks of the potential where the force impulse towards the left (right) is maximal. It is exactly this effect that leads to directed ratchetlike motion. The more momentum states that are included in the initial state, the more densely peaked is the wave function in position (angle) space. For a highly dense wave function in position space, the directed motion works with minimal dispersion. This dispersion is a specific problem in our AOKR walk with respect to an ideal quantum walk. Hence, it is indeed not too surprising that the AOKR QWs become more similar to ideal QWs when using "better" ratchet initial states. This is seen in Fig. 1(b) for the walk with the new Hadamard coin $\hat{G}_{\mathrm{H}}$ during the evolution steps. The artificial clumping at the center of the momentum distributions disappears when more momentum classes are included in the initial states [see Fig. 1(b)].

It is known that an ideal quantum walk does not display a central peak from the start, independently of the initial state (see Ref. [1]). The consequence is that an ideal walk does not display any difference between the various implementations using the different balanced coins described above. In the end, the dominant central peak, displayed when using the $\hat{G}_{\mathrm{H}}$ coin, can be seen as an artifact from AOKR realization when using the simplest initial state. This central peak disappears when adding more momentum classes to the initial state [see Fig. 1(b)]. This provides a clear prediction that could easily be checked in future experiments.

In other words, the experimentally observed residual central peak is actually a relic of the AOKR dynamics. This behavior is expected when in the walk protocol due to light shift effects the effectively implemented coin during the walk is $\hat{G}_H$ and not $\hat{Y}$, as initially intended. Even when this is the case, the central peak is only visible for an initial ratchet state sufficiently narrow in momentum space.

E. Analytic solution

A comparison between the numerical implementation of the walk given by Eq. (13) and the corresponding analytical solution derived from Eq. (17) is shown in Fig. 2. The full calculation for the analytical expression is somewhat lengthy and reveals little insight as it closely follows Refs. [32,33]. Therefore, we only present here the final result for the momentum distributions, while the calculation in full detail can be found in the Supplemental Material [35]. The final momentum

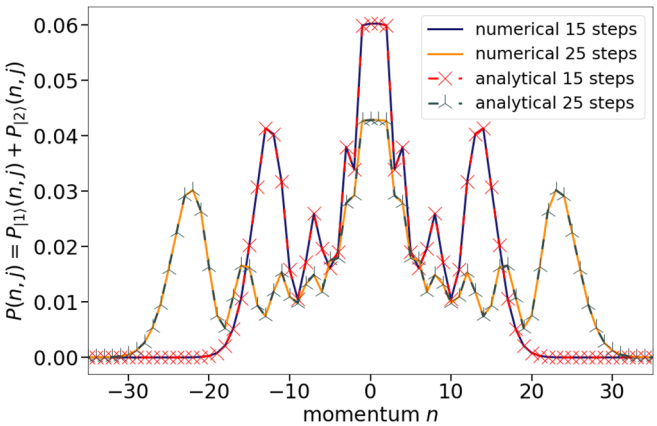

FIG. 2. Comparison between numerical implementation of the walk and its analytical solution, as derived from Eq. (17). As exemplary cases we show the final momentum distributions for $j = 15$ and $j = 25$ steps, with a kick strength $k = 1.45$. The initial state in momentum space is given by Eq. (8).

distribution is

$$P(n,j) = P_{|1\rangle}(n,j) + P_{|2\rangle}(n,j) = \frac{1}{2^{j+1}S}\Bigg[\left(\sum_{l=0}^{N}\sum_{s} a_{l,1}(-1)^s J_{(n-s)}((N-2l-1)k)\right)^2 + \left(\sum_{l=0}^{N}\sum_{s} a_{l,2}(-1)^s J_{(n-s)}((N-2l+1)k)\right)^2 + \left(\sum_{l=0}^{N}\sum_{s} a_{l,1}(-1)^s J_{(n-s)}(-(N-2l-1)k)\right)^2 + \left(\sum_{l=0}^{N}\sum_{s} a_{l,2}(-1)^s J_{(n-s)}(-(N-2l+1)k)\right)^2\Bigg]. \tag{17}$$

Here $J_\alpha(x)$ are Bessel functions of the first kind and the coefficients $a_{l,1/2}$ are given by

$$\begin{aligned} a_{l,1} = {} & \frac{1}{2^N}\sum_{u=0}^{N/2}\sum_{m=0}^{l}\left(\binom{N}{2u} - \binom{N}{2u+1}\right)\binom{u}{m}\binom{N-2m}{l-m}(-1)^{N-l+m}\,8^m \\ & + \frac{1}{2^N}2\sum_{u=0}^{N/2}\sum_{m=0}^{l-1}\binom{N}{2u+1}\binom{u}{m}\binom{N-2m-1}{l-m-1}(-1)^{N-l+m}\,8^m \\ & - \frac{1}{2^N}2\sum_{u=0}^{N/2}\sum_{m=0}^{l}\binom{N}{2u+1}\binom{u}{m}\binom{N-2m-1}{l-m}(-1)^{N-l+m}\,8^m \end{aligned} \tag{18}$$

and

$$a_{l,2} = \frac{1}{2^N}\sum_{u=0}^{N/2}\sum_{m=0}^{l}\binom{N+1}{2u+1}\binom{u}{m}\binom{N-2m}{l-m}(-1)^{-l+m}8^m, \tag{19}$$

with $N \equiv j-1$. The sum over s in Eq. (17) denotes the sum over the involved momentum classes in the initial state given by Eq. (3). Note that the momentum distribution is found to be of the same analytical form as those discussed in Ref. [33]. The coefficients only differ from previous results by a factor $(-1)^{-l}$ within the sums. These additional factors change the interference patterns in such a way that the different walk protocols, as discussed in Sec. II C, lead to different momentum distributions. Since the result above is valid for an arbitrary number of walk steps, we arrived at a full understanding of the two different QWs with the two coins $\hat{Y}$ and $\hat{W}$ (or rather $\hat{G}_{\mathrm{H}}$) interchanged.

F. Comparison between theoretical explanations

We have put forward an alternative way of understanding the central peaks around zero momentum in the experimental implementations of the AOKR quantum walks. To simulate experimental systems, we must include the finite width in the initial quasimomentum distribution of the spinor BECs mentioned in Sec. I. This is best done numerically by averaging over a reasonable ensemble of quasimomenta β [33]. Nonresonant β induces a phase scrambling [25,26], making the walks less ballistic with the effect of reducing the population in the ballistically moving side peaks. The value of β, drawn from a Gaussian distribution of a certain width β_{FWHM}, was estimated in the experiments as $\beta_{\mathrm{FWHM}} \approx 0.025$ (see Refs. [4,6]). The numerical walks are obtained as an average over 1000 realizations, with each realization involving a value of β being randomly drawn from the corresponding Gaussian.

In the left panels of Fig. 3, the walks are implemented by the $\hat{G}_{\mathrm{H}}$ coin, while the right panels feature the implementation of Eq. (16). In other words, while the left panels show the walk that we argue to be responsible for the experimentally observed momentum distributions, the right panels show theoretical predictions using experimental parameters based on the originally proposed $\hat{W}$ coin and an incorrectly chosen compensation phase [see Eq. (16)] with $\chi = \pi$ and $k = 1.45$. As anticipated in Sec. II B, the latter two protocols given by Eqs. (13) and (16) essentially lead to the same momentum distributions for all choices of $\beta_{\mathrm{FWHM}} = 0$ in Figs. 3(a) and 3(b), $\beta_{\mathrm{FWHM}} = 0.01$ in Figs. 3(c) and 3(d), and $\beta_{\mathrm{FWHM}} = 0.025$ in Figs. 3(e) and 3(f). With increasing β_{FWHM}, the side peaks and the central regions become less and less distinct and the ballistic side peaks tend to fade out.

Similar behavior is seen in our experimental data [4–6]. Figure 4(a) shows a typical experimental result adapted from Ref. [4]. We find good theory-experiment agreements by comparing Fig. 4(a) with Fig. 4(b) that shows the predictions of our current model [see Eq. (13)]. First, we observe in both Figs. 4(a) and 4(b) a central part that does not evolve far away from the origin and the two side peaks that evolve ballistically away from their initial position in momentum space. Second, the observed and predicted rates of the spread of these side peaks in momentum space with increasing number of steps appear comparable. Our current interpretation shown in Fig. 4(b) would also be in reasonable agreement with the originally guessed temperature of the BEC with $\beta_{\mathrm{FWHM}} \approx 0.025$, when the fading of the side peaks is considered. Figure 4(c) shows momentum distributions of the QW given by the previous theoretical model [see Eq. (5)] after a residual thermal cloud of atoms is added into the BECs.

The thermal cloud was originally assumed as a possible solution for the appearance of the prominent central region.

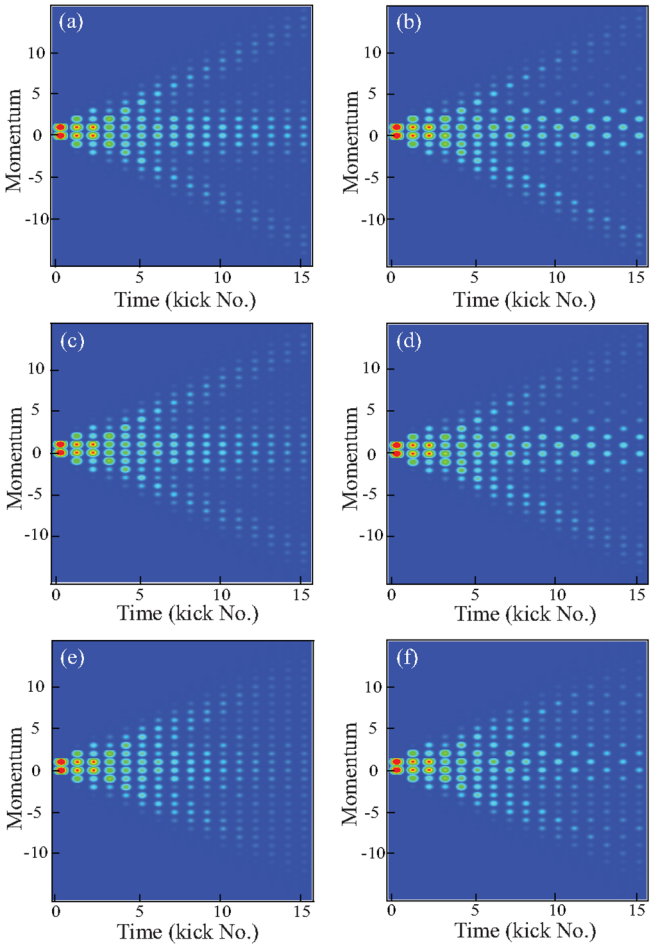

FIG. 3. Numerical simulations of AOKR quantum walks with $k = 1.45$ and different quasimomentum distributions with $\beta_{\mathrm{FWHM}} = 0$ (a,b), $\beta_{\mathrm{FWHM}} = 0.01$ (c,d), and $\beta_{\mathrm{FWHM}} = 0.025$ (e,f), all averaged over 1000 values of β. Left panels: implemented with the $\hat{G}_{\mathrm{H}}$ coin. Right panels: executed with Eq. (16) at $\chi = \pi$. It can be seen that despite the small deviations, as discussed in Sec. II B, both protocols essentially follow the same behavior, making both likely to correspond to the actual experimental data.

Thermal atoms essentially will not follow the kicking evolution [25,26] and hence remain close to the center. The experimentally intended $\hat{Y}$ protocol does not display this behavior, as can be seen from Fig. 1. However, the QWs shown in Fig. 4(c) appear to be different from our experimental observations, i.e., the predicted QWs lack the significantly contributing central region and the structures of the side peaks are of a quite different shape.

The mean energies of the present and original theoretical models were calculated and plotted as a function of time in Fig. 5 for comparison. It can be seen that the energy using $\hat{G}_H$ coin increases faster than that of the previous model. The increase in mean energy for the $\hat{Y}$ coin has a linear form, while the $\hat{G}_H$ coin increases more quadratically. Note that quantum resonant AOKR walks possess a quadratic increase in mean energy, corresponding to a ballistic motion in momentum space. In the presence of a strong off-resonant β distribution

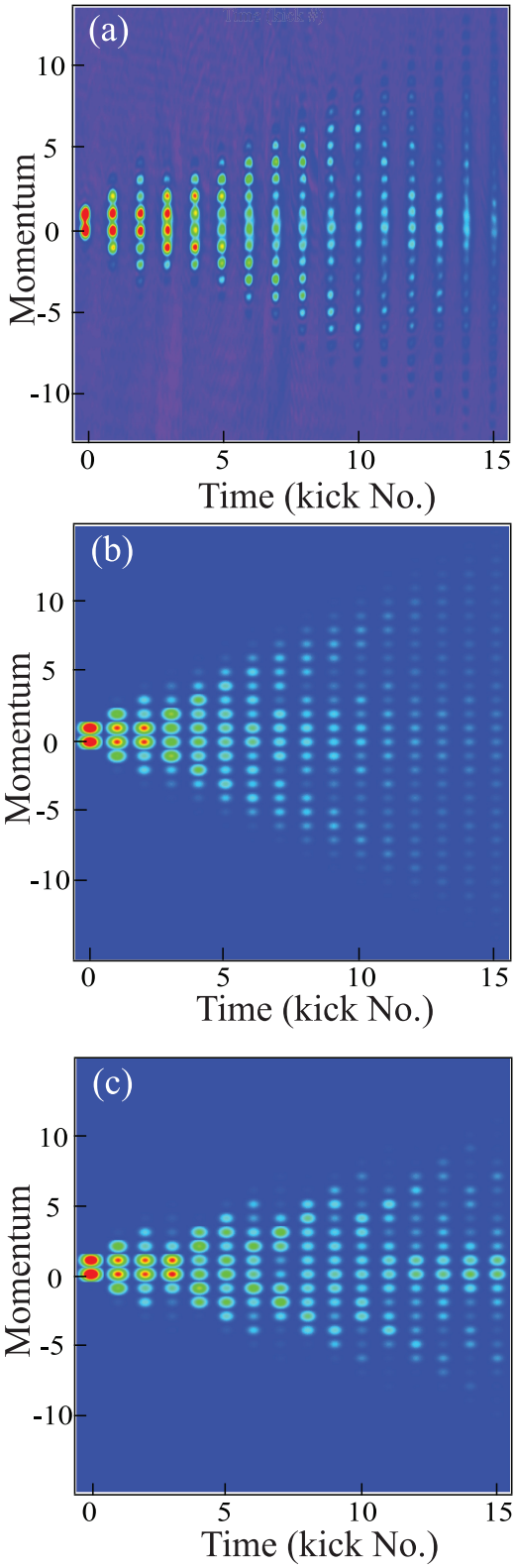

FIG. 4. AOKR quantum walks with $k = 1.45$. (a) Experimental data adapted from Ref. [4]. (b) Numerical simulation derived from our current theoretical model [see Eq. (13)] with $\beta_{\mathrm{FWHM}} = 0.025$ and using initial $\hat{Y}$ rotation and $\hat{G}_H$ coins. (c) Numerical simulation derived from the previous theoretical model [see Eq. (5)] by adding a cloud of thermal atoms to the BEC part (see text).

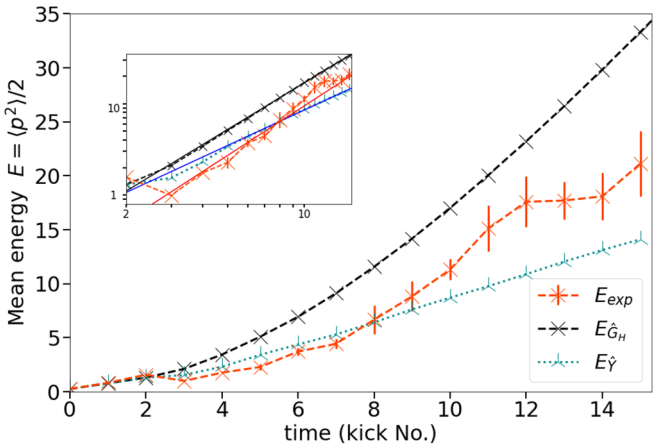

FIG. 5. Comparison between the mean kinetic energies calculated from the walks seen in Fig. 4 with $\beta_{\mathrm{FWHM}} = 0.025$. The energy, E_{exp}, is extracted from the experimental walk data from Fig. 4(a). $E_{\hat{G}_{\mathrm{H}}}$ and $E_{\hat{Y}}$ denote the mean energy for the walk executed by the $\hat{G}_H$ coin [Fig. 4(b)] and the $\hat{Y}$ coin [Fig. 4(c)], respectively. The inset shows the energies on a double logarithmic scale with power-law exponents extracted by the fits (solid lines), giving 1.8 ± 0.2 for the experimental data and 1.7 ± 0.1 ($E_{\hat{G}_{\mathrm{H}}}$) and 1.3 ± 0.1 ($E_{\hat{Y}}$) for the two theoretical models. The apparent better agreement between the fits for E_{exp} and $E_{\hat{G}_{\mathrm{H}}}$ confirms the better scaling of the model. The asymptotic exponent of 2 expected for a ballistic walk is hardly reached for quantum walks with just 15 steps.

like the residual thermal cloud from the original theory, the energy increases only linearly [25,26]. The data shown for a small number of up to 15 steps maximum show that the asymptotic regimes are rarely met.

The mean energy extracted from experimental data presented in Fig. 4(a) is also plotted in Fig. 5. The experimentally obtained energy increases with more quadratic than linear behavior, which is more consistent with current theory and contradicts the presence of a thermal cloud as originally hypothesized. The comparison is yet more complicated since the experimental suffered from a series of well-known issues; see Ref. [6]. The effect most relevant in our context is the fading out of the ballistic peaks in the experimental momentum distributions due to atom number fluctuations and small atom losses. Each time slice is obtained from a new experimental run, and hence also the relative normalization of the atomic density might be an issue. All this may have consequences on the second moment of the distribution that is proportional to the energy plotted in Fig. 5. Counting less in the tails of the distribution typically leads to an underestimation of the mean energy [26].

In the Supplemental Material [35], we also show further comparisons between our current theoretical model [see Eq. (13)] and the previous experimental data, in particular similar plots as in Fig. 4 for other values of the kick strength and a more direct matching of the momentum distributions for a specific case.

III. CONCLUSION

We have introduced a more complete theoretical explanation for the peculiar behavior observed in the discrete-time quantum walks implemented with the AOKR platform in Refs. [4–6]. We argue that the coin operations acting on the internal states of the atoms may have been different from the original proposal discussed in [31]. This difference, induced by the experimental calibration of the coin parameters together with an additional AC-Stark shift present in the setup, may have led to less efficient quantum walks with a large population remaining close to the starting site of the walker. Our hypothesis may be checked in future experiments by either controlling much better the MW phases at compensated light shift or using ratchet states with less dispersion [28] as initial states for the walks.

The understanding of the experimental results is of importance for further applications of walks realized with the AOKR platform. Our analysis implies that the realized walks may have had a higher quality than expected in the following manner: the central population seemingly not participating in the walker's evolution is actually an artificial interference effect induced by a nonoptimal coin and therefore an ingredient of the system itself. This effect makes the AOKR platform look even better for the quantum simulation of nontrivial walks and the investigation of applications such as quantum search algorithms [36] or of topological phases in Floquet-driven systems [37].

ACKNOWLEDGMENTS

A.G. acknowledges support by the Deutsche Forschungsgemeinschaft (German Research Foundation), Project No. 441423094. J.H.C. and Y.L. thank the Noble Foundation for financial support.

[1] J. Kempe, Quantum random walks: An introductory overview, Contemp. Phys. **44**, 307 (2003).
[2] R. Portugal, *Quantum Walks and Search Algorithms* (Springer, New York, 2018)
[3] N. B. Lovett, S. Cooper, M. Everitt, M. Trevers, and V. Kendon, Universal quantum computation using the discrete-time quantum walk, Phys. Rev. A **81**, 042330 (2010).
[4] S. Dadras, A. Gresch, C. Groiseau, S. Wimberger, and G. S. Summy, Quantum Walk in Momentum Space with a Bose-Einstein Condensate, Phys. Rev. Lett. **121**, 070402 (2018).
[5] J. H. Clark, C. Groiseau, Z. N. Shaw, S. Dadras, C. Binegar, S. Wimberger, G. S. Summy, and Y. Liu, Quantum to classical walk transitions tuned by spontaneous emissions, Phys. Rev. Research **3**, 043062 (2021).
[6] S. Dadras, A. Gresch, C. Groiseau, S. Wimberger, and G. S. Summy, Experimental realization of a momentum-space quantum walk, Phys. Rev. A **99**, 043617 (2019).
[7] P. M. Preiss, R. Ma, M. E. Tai, A. Lukin, M. Rispoli, P. Zupancic, Y. Lahini, R. Islam, and M. Greiner, Strongly correlated quantum walks in optical lattices, Science **347**, 1229 (2015).

[8] W. Dür, R. Raussendorf, V. M. Kendon, and H.-J. Briegel, Quantum walks in optical lattices, Phys. Rev. A **66**, 052319 (2002).

[9] K. Eckert, J. Mompart, G. Birkl, and M. Lewenstein, One- and two-dimensional quantum walks in arrays of optical traps, Phys. Rev. A **72**, 012327 (2005).

[10] A. Steffen, A. Alberti, W. Alt, N. Belmechri, S. Hild, M. Karski, A. Widera, and D. Meschede, Digital atom interferometer with single particle control on a discretized space-time geometry, Proc. Natl. Acad. Sci. U.S.A. **109**, 9770 (2012).

[11] T. Groh, S. Brakhane, W. Alt, D. Meschede, J. K. Asbóth, and A. Alberti, Robustness of topologically protected edge states in quantum walk experiments with neutral atoms, Phys. Rev. A **94**, 013620 (2016).

[12] M. Karski, L. Förster, J.-M. Choi, A. Steffen, W. Alt, D. Meschede, and A. Widera, Quantum walk in position space with single optically trapped atoms, Science **325**, 174 (2009).

[13] C. M. Chandrashekar, Implementing the one-dimensional quantum (Hadamard) walk using a Bose-Einstein condensate, Phys. Rev. A **74**, 032307 (2006).

[14] B. C. Travaglione and G. J. Milburn, Implementing the quantum random walk, Phys. Rev. A **65**, 032310 (2002).

[15] F. Zähringer, G. Kirchmair, R. Gerritsma, E. Solano, R. Blatt, and C. F. Roos, Realization of a Quantum Walk with One and Two Trapped Ions, Phys. Rev. Lett. **104**, 100503 (2010).

[16] H. Schmitz, R. Matjeschk, C. Schneider, J. Glueckert, M. Enderlein, T. Huber, and T. Schaetz, Quantum Walk of a Trapped Ion in Phase Space, Phys. Rev. Lett. **103**, 090504 (2009).

[17] H. B. Perets, Y. Lahini, F. Pozzi, M. Sorel, R. Morandotti, and Y. Silberberg, Realization of Quantum Walks with Negligible Decoherence in Waveguide Lattices, Phys. Rev. Lett. **100**, 170506 (2008).

[18] A. Peruzzo, M. Lobino, J. C. Matthews, N. Matsuda, A. Politi, K. Poulios, X.-Q. Zhou, Y. Lahini, N. Ismail, K. Wörhoff *et al.*, Quantum walks of correlated photons, Science **329**, 1500 (2010).

[19] F. Cardano, A. D'Errico, A. Dauphin, M. Maffei, B. Piccirillo, C. de Lisio, G. De Filippis, V. Cataudella, E. Santamato, L. Marrucci *et al.*, Detection of Zak phases and topological invariants in a chiral quantum walk of twisted photons, Nat. Commun. **8**, 15516 (2017).

[20] C. Chen, X. Ding, J. Qin, Y. He, Y.-H. Luo, M.-C. Chen, C. Liu, X.-L. Wang, W.-J. Zhang, H. Li *et al.*, Observation of Topologically Protected Edge States in a Photonic Two-Dimensional Quantum Walk, Phys. Rev. Lett. **121**, 100502 (2018).

[21] H. Tang, X.-F. Lin, Z. Feng, J.-Y. Chen, J. Gao, K. Sun, C.-Y. Wang, P.-C. Lai, X.-Y. Xu, Y. Wang *et al.*, Experimental two-dimensional quantum walk on a photonic chip, Sci. Adv. **4**, eaat3174 (2018).

[22] K. Poulios, R. Keil, D. Fry, J. D. A. Meinecke, J. C. F. Matthews, A. Politi, M. Lobino, M. Gräfe, M. Heinrich, S. Nolte, A. Szameit, and J. L. OBrien, Quantum Walks of Correlated Photon Pairs in Two-Dimensional Waveguide Arrays, Phys. Rev. Lett. **112**, 143604 (2014).

[23] A. Schreiber, K. N. Cassemiro, V. Potoček, A. Gábris, P. J. Mosley, E. Andersson, I. Jex, and C. Silberhorn, Photons Walking the Line: A Quantum Walk with Adjustable Coin Operations, Phys. Rev. Lett. **104**, 050502 (2010).

[24] M. G. Raizen, Quantum chaos with cold atoms, Adv. At. Mol. Opt. Phys. **41**, 43 (1999).

[25] M. Sadgrove and S. Wimberger, A pseudo-classical method for the atom-optics kicked rotor: from theory to experiment and back, Adv. At. Mol. Opt. Phys. **60**, 315 (2011).

[26] S. Wimberger, I. Guarneri, and S. Fishman, Quantum resonances and decoherence for delta-kicked atoms, Nonlinearity **16**, 1381 (2003).

[27] J. Ni, W. K. Lam, S. Dadras, M. F. Borunda, S. Wimberger, and G. S. Summy, Initial-state dependence of a quantum resonance ratchet, Phys. Rev. A **94**, 043620 (2016).

[28] J. Ni, S. Dadras, W. Lam, R. Shrestha, M. Sadgrove, S. Wimberger, and G. S. Summy, Hamiltonian ratchets with ultracold atoms, Ann. Phys. (NY) **529**, 1600335 (2017).

[29] M. Sadgrove, M. Horikoshi, T. Sekimura, and K. Nakagawa, Rectified Momentum Transport for a Kicked Bose-Einstein Condensate, Phys. Rev. Lett. **99**, 043002 (2007).

[30] I. Dana, V. Ramareddy, I. Talukdar, and G. S. Summy, Experimental Realization of Quantum-Resonance Ratchets at Arbitrary Quasimomenta, Phys. Rev. Lett. **100**, 024103 (2008).

[31] G. S. Summy and S. Wimberger, Quantum random walk of a Bose-Einstein condensate in momentum space, Phys. Rev. A **93**, 023638 (2016).

[32] C. Groiseau, Discrete-time quantum walks in momentum space, Master's thesis, Heidelberg University, 2017 (unpublished).

[33] C. Groiseau, A. Gresch, and S. Wimberger, Quantum walks of kicked Bose-Einstein condensates, J. Phys. A: Math. Theor. **51**, 275301 (2018).

[34] N. B. Delone and V. P. Krainov, AC Stark shift of atomic energy levels, Phys. Usp. **42**, 669 (1999).

[35] See Supplemental Material at http://link.aps.org/supplemental/10.1103/PhysRevA.106.033307 for the full analytical computation regarding the momentum distribution and additional numerical comparisons with experimental data for several kicking strengths.

[36] M. Delvecchio, C. Groiseau, F. Petiziol, G. S. Summy, and S. Wimberger, Quantum search with a continuous-time quantum walk in momentum space, J. Phys. B: At., Mol. Opt. Phys. **53**, 065301 (2020).

[37] C. Groiseau, A. Wagner, G. S. Summy, and S. Wimberger, Impact of lattice vibrations on the dynamics of a spinor atom-optics kicked rotor, Condensed Matter **4**, 10 (2019).

APPENDIX D

DETECTING TOPOLOGICAL PHASE TRANSITIONS IN A DOUBLE KICKED QUANTUM ROTOR

This appendix includes a reprint of Ref. [15]: N. Bolik, C. Groiseau, J. H. Clark, G. S. Summy, Y. Liu, and S. Wimberger *Detecting topological phase transitions in a double kicked quantum rotor*, Phys. Rev. A **106**, 043318 (2022)

Detecting topological phase transitions in a double kicked quantum rotor

Nikolai Bolik,[1] Caspar Groiseau,[2] Jerry H. Clark,[3] Gil S. Summy,[3,4,*] Yingmei Liu,[3,†] and Sandro Wimberger[5,6,‡]

[1]*Institute of Theoretical Physics, Heidelberg University, Philosophenweg 16, 69120 Heidelberg, Germany*

[2]*Departamento de Física Teórica de la Materia Condensada and Condensed Matter Physics Center (IFIMAC), Universidad Autónoma de Madrid, 28049 Madrid, Spain*

[3]*Department of Physics, Oklahoma State University, Stillwater, Oklahoma 74078-3072, USA*

[4]*Airy3D, 5445 Avenue de Gaspé Suite 230, Montréal, Québec, Canada H2T 3B2*

[5]*Dipartimento di Scienze Matematiche, Fisiche e Informatiche, Università di Parma, Parco Area delle Scienze 7/A, 43124 Parma, Italy*

[6]*INFN, Sezione di Milano Bicocca, Gruppo Collegato di Parma, Parco Area delle Scienze 7/A, 43124 Parma, Italy*

(Received 14 July 2022; accepted 5 October 2022; published 19 October 2022)

We present a concrete theoretical proposal for detecting topological phase transitions in double kicked atom-optics kicked rotors with internal spin-1/2 degree of freedom. The implementation utilizes a kicked Bose-Einstein condensate evolving in one-dimensional momentum space. To reduce the influence of atom loss and phase decoherence, we aim to keep experimental durations short while maintaining a resonant experimental protocol. Experimental limitations induced by phase noise, quasimomentum distributions, symmetries, and the ac-Stark shift are considered. Our results thus suggest a feasible and optimized procedure for observing topological phase transitions in quantum kicked rotors.

DOI: 10.1103/PhysRevA.106.043318

I. INTRODUCTION

Studies of topological phases have found many applications, including revealing topologically protected edge states in topological insulators [1–5]. Stabilities of topological invariants are translated upon these edge states, enabling them to be stable against a great variety of perturbations. This robustness to decoherence makes topological phenomena intriguing for many potential applications, e.g., in quantum computing [6] and quantum walks [7].

Topological effects can be simulated by periodically driven systems in a well-controlled manner [7–9]. A double kicked quantum rotor (DKQR) with internal spin-1/2 degree of freedom is an example of such a system and therefore a potential candidate to experimentally realize topological phase transitions [10,11]. In the DKQR system a quantity known as a winding number ν is topologically invariant under a wide range of transformations [10]. A similar phenomenon occurs in solid-state systems where holes are preserved under certain transformations due to geometrical topology [12]. Preservation of topological winding numbers requires preservation of chiral symmetry and the band gap [10,11]. A consequence of permanently containing chiral symmetry is that the topological invariant can only change when the system is changed to a configuration in which the band gap closes. This closure not only makes the phase undetermined but also allows for its direct experimental control by scanning a system parameter through it.

The same is true for periodically driven systems with Floquet spectra, as in our case of the DKQR [10]. Here, the quasienergy spectrum itself is periodic, and gaps can be controlled by the driving parameters. Floquet topological states were observed in different experimental settings, including ultracold atom [13,14], photonic [15–17], and phononic and acoustic systems [18–20]. To understand which topological phases the system has, one examines its spectral symmetries and the related "protected gaps" in the quasienergy spectrum of the Floquet Hamiltonian; see, e.g., Refs. [7,21,22]. In our DKQR systems, the gaps and the phases can be tuned by the kicking strengths, as described in detail in Ref. [10].

The experimental setup under consideration as described in Ref. [23] consists of a Bose-Einstein condensate (BEC) with two Zeeman hyperfine states $|1\rangle$ and $|2\rangle$ participating in the dynamics, effectively forming a spin-1/2 system. The DKQR is based on a singly quantum kicked rotor (QKR) [24,25] and is described by the Hamiltonian

$$\hat{\mathcal{H}} = \frac{\hat{p}^2 \otimes \mathbf{1}}{2} + k_1 \cos(\hat{\theta}) \otimes \hat{\sigma}_x \cdot \sum_{n=0}^{\infty} \delta(t - 2n\tau) + k_2 \sin(\hat{\theta}) \otimes \hat{\sigma}_y \cdot \sum_{n=0}^{\infty} \delta(t - (2n+1)\tau). \quad (1)$$

Here, $\hat{p}$ and $\hat{\theta}$ are the momentum and angular position operators, respectively, τ describes the duration between two kicks of different kicking strengths k_1 and k_2, and the Pauli matrices $\hat{\sigma}_x$ and $\hat{\sigma}_y$ act on the internal spin-1/2 degree of freedom. Under the on-resonance condition of $\tau = 4\pi$ [26–32], corresponding to a full revival (at the Talbot time) of the free evolution of the momentum degree of freedom, the quasiperiodicity of the system can lead to a Hofstadter

*gil.summy1@gmail.com
†yingmei.liu@okstate.edu
‡sandromarcel.wimberger@unipr.it

butterflylike quasienergy spectrum [33–35], resolving a band structure rich in displaying topological properties [10].

The previously proposed experimental sequences for achieving topological phase transitions in DKQRs include a sequence of resonant microwave (MW) and standing-wave kicking laser pulses [10,11]. Similar sequences have been successfully conducted on QKR systems, including ours consisting of ^{87}Rb BECs [23,36,37]. For observing the predicted topological effects, the experimental procedure needs to be carefully designed to overcome a number of experimental challenges. In particular, phase noise arising from random phase fluctuations in the MW pulses and a finite quasimomentum distribution of the BEC must be considered. In this paper we demonstrate how to transform the proposals for detecting topological phases in DKQRs [10,11] into a feasible experimental procedure by presenting solutions to some experimental limitations or challenges that appear in the BEC-based quantum walk and DKQR setups [23,36,37].

II. PREVIOUS THEORETICAL PROPOSALS

We briefly review previous proposals for the measurement of the topological phases in the DKQR setup [10,11]. In these proposals, the MW operations correspond to a Rabi coupling between the two internal states $|F=1, m_F=0\rangle$ and $|F=2, m_F=0\rangle$ of the atoms and are expressed as a unitary rotation on the Bloch sphere:

$$\hat{M}(\alpha,\chi)=\begin{pmatrix}\cos(\frac{\alpha}{2}) & e^{-i\chi}\sin(\frac{\alpha}{2})\\ -e^{i\chi}\sin(\frac{\alpha}{2}) & \cos(\frac{\alpha}{2})\end{pmatrix}. \tag{2}$$

The kicking laser is detuned between these internal states in such a way that the potential is equal in strength but opposite in sign, as expressed by a $\hat{\sigma}_z$ matrix. The kick operators $\hat{K}_1$ and $\hat{K}_2$, differing only by a shift of $\theta=\pi/2$ in position space, are defined as

$$\hat{K}_1=e^{-ik_1\cos(\hat{\theta})\hat{\sigma}_z}, \tag{3}$$

$$\hat{K}_2=e^{-ik_2\sin(\hat{\theta})\hat{\sigma}_z}. \tag{4}$$

As discussed in detail in Ref. [10], the system consists of two chirally symmetric time frames expressed with two Floquet operators, $\hat{U}_1$ and $\hat{U}_2$, possessing chiral symmetry. These operators are best realized as a sequence of MW and kick operators on the atoms' initial wave function, e.g., $|\psi_{\text{in}}\rangle = |n=0\rangle\otimes|2\rangle$, and take the following form:

$$\begin{aligned}\hat{U}_1=&\hat{M}\Big(-\frac{\pi}{2},0\Big)\hat{K}_1^{\frac{1}{2}}\hat{M}\Big(\frac{\pi}{2},0\Big)\hat{M}\Big(-\frac{\pi}{2},\frac{\pi}{2}\Big)\hat{K}_2\hat{M}\Big(\frac{\pi}{2},\frac{\pi}{2}\Big)\\&\cdot\hat{M}\Big(-\frac{\pi}{2},0\Big)\hat{K}_1^{\frac{1}{2}}\hat{M}\Big(\frac{\pi}{2},0\Big),\end{aligned} \tag{5}$$

$$\begin{aligned}\hat{U}_2=&\hat{M}\Big(-\frac{\pi}{2},\frac{\pi}{2}\Big)\hat{K}_2^{\frac{1}{2}}\hat{M}\Big(\frac{\pi}{2},\frac{\pi}{2}\Big)\hat{M}\Big(-\frac{\pi}{2},0\Big)\hat{K}_1\hat{M}\Big(\frac{\pi}{2},0\Big)\\&\cdot\hat{M}\Big(-\frac{\pi}{2},\frac{\pi}{2}\Big)\hat{K}_2^{\frac{1}{2}}\hat{M}\Big(\frac{\pi}{2},\frac{\pi}{2}\Big),\end{aligned} \tag{6}$$

with

$$\hat{K}_{1,2}^{1/2}\equiv\hat{K}_{1,2}\Big(\frac{k}{2},\theta\Big). \tag{7}$$

Due to the structural similarity of both operators we will further focus on the discussion of $\hat{U}_2$, referred to hereafter as $\hat{\mathcal{U}}$ in this paper. Analogous reasoning can be found for $\hat{U}_1$ but is not explicitly shown here.

As an abstract quantity, the topological winding number is not often directly measurable. Instead a quantity, the mean chiral displacement (MCD), is introduced in this context [10]. In DKQRs the MCD, describing the difference between momentum distributions of the two internal states that evolve under $\hat{\mathcal{U}}$, is defined as

$$\begin{aligned}C(t)&=\langle\psi_t|\hat{n}\otimes-\hat{\sigma}_z|\psi_t\rangle\\&\equiv\langle\psi_0|\hat{\mathcal{U}}^{-t}(\hat{n}\otimes-\hat{\sigma}_z)\hat{\mathcal{U}}^t|\psi_0\rangle.\end{aligned} \tag{8}$$

The average of the MCD over several discrete evolution steps t converges to half of the topological winding number ν [10]:

$$\bar{C}(t)=\frac{1}{t}\sum_{t_i=1}^{t}C(t_i)\xrightarrow{t\gg1}\frac{\nu}{2}. \tag{9}$$

To observe the topological phase transitions, it is necessary to repeat application of Eq. (6) for a series of configurations of k_1 and k_2 where the empirical results can be compared with the ideal phase diagram computed in Ref. [10].

III. OPTIMIZED EXPERIMENTAL SEQUENCE

The first and last MW rotations within Eq. (6) are inverses of each other. If $\hat{\mathcal{U}}$ is applied subsequently for a larger number of evolution steps $t\in\mathbb{N}$, this sequence of MW rotations and kicks can be simplified as demonstrated in full detail in Appendix A. Considering the full evolution of the system, an alternative expression of $\hat{\mathcal{U}}^t$ is therefore found as

$$\begin{aligned}\hat{\mathcal{U}}^t=&\hat{M}\Big(-\frac{\pi}{2},\frac{\pi}{2}\Big)\hat{K}_2^{\frac{1}{2}}\hat{M}\Big(\frac{\pi}{2},\frac{\pi}{2}\Big)\cdot\Big[\hat{M}\Big(-\frac{\pi}{2},0\Big)\hat{K}_1\hat{M}\Big(\frac{\pi}{2},0\Big)\\&\times\hat{M}\Big(-\frac{\pi}{2},\frac{\pi}{2}\Big)\hat{K}_2\hat{M}\Big(\frac{\pi}{2},\frac{\pi}{2}\Big)\Big]^{t-1}\\&\cdot\hat{M}\Big(-\frac{\pi}{2},0\Big)\hat{K}_1\hat{M}\Big(\frac{\pi}{2},0\Big)\hat{M}\Big(-\frac{\pi}{2},\frac{\pi}{2}\Big)\hat{K}_2^{\frac{1}{2}}\hat{M}\Big(\frac{\pi}{2},\frac{\pi}{2}\Big).\end{aligned} \tag{10}$$

Although this new expression looks more complex, rewriting the sequence in this form significantly reduces the number of operations necessary to realize the complete evolution $\hat{\mathcal{U}}^t$. This is indeed of great interest because it shortens experimental durations, reducing the impact of atom loss and other sources of decoherence (see, e.g., Ref. [23] for a short summary of these effects).

So far each application of the MW operator is assumed to be infinitely short in time corresponding to a fully quantum resonant atom-optics kicked rotor [25,38]. However, this assumption does not apply to typical experiments since every MW rotation has a finite duration $\mathcal{T}$. A free-evolution operator thus needs to be added after each MW operator as follows:

$$\hat{M}(\alpha,\chi)\to e^{-i\frac{\hat{p}^2}{2}\mathcal{T}}\hat{M}(\alpha,\chi). \tag{11}$$

Experimental durations can be further reduced by keeping $\mathcal{T}$ as short as possible. When $\mathcal{T}=4\pi$, the free-evolution operator reduces to unity and thus reflects a full Talbot period. This in turn corresponds to an on-resonance atom-optics kicked rotor [25,38]. In a specific case of Eq. (10), it is

possible to produce a resonant configuration with $\mathcal{T} = \pi$, corresponding to a good MW signal with a quarter Talbot period. In this paper, we consider $\mathcal{T} = \pi$ and free evolution of the form $e^{-i\frac{\hat{p}^2}{2}\pi} \equiv \hat{P}_\pi$. In Appendix B the free-evolution operator is identified with the shift operator $\hat{T}(\hat{\theta}) = e^{i\hat{n}\hat{\theta}}$, where $\theta = \pi$ in position space; thus $\hat{P}_\pi^2 = \hat{T}(\pi)$. As a consequence of introducing the free evolution $\hat{P}_\pi$, every second kick operator experiences an effective inversion:

$$\begin{aligned}\hat{\mathcal{U}}^t \to\ & \hat{P}_\pi \hat{M}\left(-\frac{\pi}{2}, \frac{\pi}{2}\right)\hat{K}_2^{\frac{1}{2}}\hat{M}\left(\frac{\pi}{2}, \frac{\pi}{2}\right) \\ & \times \left[\hat{M}\left(-\frac{\pi}{2}, 0\right)\hat{K}_1^{-1}\hat{M}\left(\frac{\pi}{2}, 0\right)\right. \\ & \left. \cdot\, \hat{M}\left(-\frac{\pi}{2}, \frac{\pi}{2}\right)\hat{K}_2\hat{M}\left(\frac{\pi}{2}, \frac{\pi}{2}\right)\right]^{t-1} \\ & \cdot \hat{M}\left(-\frac{\pi}{2}, 0\right)\hat{K}_1^{-1}\hat{M}\left(\frac{\pi}{2}, 0\right) \\ & \times \hat{M}\left(-\frac{\pi}{2}, \frac{\pi}{2}\right)\hat{K}_2^{\frac{1}{2}}\hat{P}_\pi\hat{M}\left(-\frac{\pi}{2}, \frac{\pi}{2}\right). \end{aligned} \tag{12}$$

More calculation details can be found in Appendix C. Although this free-evolution effect is undesired, it fortunately does not affect the measurement of topological phase transitions as discussed in Sec. III A. Note that this induced inversion symmetry [see Eq. (12)] simplifies the observation of topological phase transitions in our ^{87}Rb system where the required π pulse has a duration of $\approx$26 μs achievable via a high-power MW amplifier [23,36,37,39]. If $\hat{\mathcal{U}}^t$ is computed for a MW rotation of $\mathcal{T} = \pi$ without the simplification using Eq. (10), the resultant operator sequence is antiresonant inducing periodic oscillations in momentum space. This is understood analytically and verified with numerical calculations. Therefore a combination of our proposal [see Eqs. (10) and (12)] and setting $\mathcal{T} = \pi$ is needed for an optimized experimental sequence for realizing topological phase transitions in DKQRs.

A. Inversion symmetry

A finite duration $\mathcal{T} = \pi$ of each MW rotation results in every second kick operator being effectively inverted (see Appendix C), i.e.,

$$\hat{K}_1 = e^{-ik_1\cos(\hat{\theta})\hat{\sigma}_z} \to e^{+ik_1\cos(\hat{\theta})\hat{\sigma}_z}, \tag{13}$$

$$\hat{K}_2 = e^{-ik_2\sin(\hat{\theta})\hat{\sigma}_z} \to e^{-ik_2\sin(\hat{\theta})\hat{\sigma}_z}. \tag{14}$$

Instead of a relative shift of $\theta = \pi/2$ in position space in between the two kicks [see Eqs. (3) and (4)], Eqs. (13) and (14) indicate that the relative shift is $\theta = -\pi/2$. This is equivalent to an inversion in position or angle space around the zero angle. As a result, momentum distributions of the internal states evolve along opposite directions. This causes the expectation value of momentum for each internal state respectively to change sign, as illustrated in Fig. 1.

Equations (8) and (9) also indicate that the topological curves computed from the average MCD change their signs due to introducing the finite MW duration of $\mathcal{T} = \pi$. This does not change the underlying physics, and thus the expected phase transitions are still visible although with a change in sign. This undesired effect can be compensated by changing

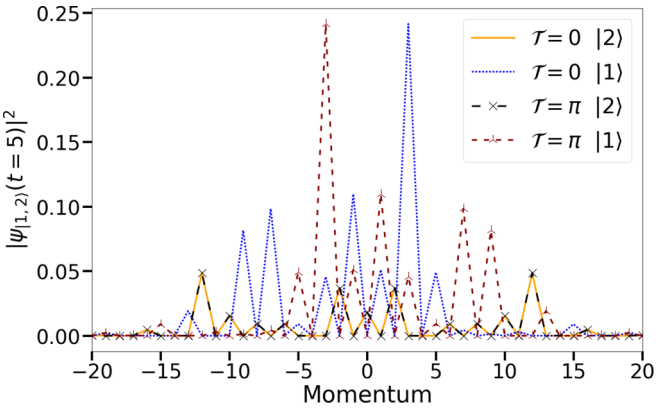

FIG. 1. Momentum distributions of the internal states after $t = 5$ applications of $\hat{\mathcal{U}}$ for $k_1 = \frac{\pi}{2}$ and $k_2 = 2.5\pi$. The initial state is $|\psi_{\text{in}}\rangle = |n = 0\rangle \otimes |2\rangle$. $\mathcal{T} = 0$ corresponds to fully resonant conditions, while $\mathcal{T} = \pi$ specifies MW pulses with the finite duration. If $\mathcal{T} = \pi$ is chosen, the momentum distributions of the internal states are mirrored respectively to the ideal case. Note that the initial state $|2\rangle$ evolves symmetrically in momentum space, thus not contributing to the MCD.

several phase angles of the MW operators. For instance, we find that

$$\begin{aligned}&\hat{M}\left(-\frac{\pi}{2}, 0\right)e^{-ik_1\cos(\hat{\theta})\hat{\sigma}_z}\hat{M}\left(\frac{\pi}{2}, 0\right) \\ &\quad = \hat{M}\left(\frac{\pi}{2}, 0\right)e^{ik_1\cos(\hat{\theta})\hat{\sigma}_z}\hat{M}\left(-\frac{\pi}{2}, 0\right). \end{aligned} \tag{15}$$

This change in the phases within the MW rotations causes a change in sign in the exponent and thus compensates for the aforementioned change of the two internal states.

B. Initial state dependence

Momentum distributions are good observables in QKR and quantum walk experiments, as shown in Refs. [23,36,37], where the complete momentum distribution $P(t) = P(t)_{|1\rangle} + P(t)_{|2\rangle}$ is measured over one experimental cycle. The momentum distributions for the two internal states, $P(t)_{|1\rangle}$ and $P(t)_{|2\rangle}$, however, need to be measured separately to compute the MCD using Eq. (8). This may double the experimental effort, because one MCD measurement requires two consecutive experimental cycles with one cycle addressing one individual state in systems similar to those shown in Refs. [24,25]. The presence of additional symmetries can ease this requirement because a state symmetrically evolving in momentum space has a zero mean momentum and no contribution to the MCD. Therefore, if one of the internal states is symmetric in momentum space, the information of the topological winding number can be conveniently extracted from the momentum distributions of the other internal state. As a result this effectively reduces the number of experimental measurements in practice. A good example is illustrated in Fig. 1.

IV. STABILITY

Some experimental imperfections, for example, fluctuations in kicking strengths and pulse durations, have little effect

on the MCD measurements [10] because the kicks can be timed with good precision and resonant atom-optics kicked rotors are intrinsically stable with respect to such imperfections [25]. In this section we focus on three unavoidable experimental limitations impacting phase evolutions of the system. First, we will investigate the most crucial problem of uncontrolled phases of the MW pulses. There are many MW pulses during a single experimental cycle [see Eq. (12)]; thus these phase errors would accumulate quickly. Second, different quasimomenta result in coherent but unwanted deviations from quantum resonance in atom-optics kicked rotors. It is necessary to verify whether the typical spread in momentum reported previously [23,36,37] has some impact on the measurement of topological phases. The third problem arises from a relative energy shift between the two internal states. This leads to a relative dynamical phase in the evolution that must be corrected.

A. Phase noise

One major source of perturbation originates from fluctuations in the precise timing of the internal MW rotations across the ensemble [23]. This effectively leads to fluctuations in the phase parameter χ in the MW rotation operator $\hat{M}(\alpha, \chi)$ [see Eq. (2)] as follows:

$$\hat{M}(\alpha, \chi) \to \hat{M}(\alpha, \chi + \Delta_\chi), \tag{16}$$

modeled numerically as a time-dependent random walk within an additional dynamical phase $\Delta_\chi = \sum_{i=1}^{l} \delta_{\chi,i}$. Here, $\delta_{\chi,i} \in \text{uniform}[-\phi, \phi]$ is drawn individually for each MW application, and l counts the number of subsequent MW applications.

DKQRs are much more complicated than a single kicked atom-optics kicked rotor (see Refs. [24,25]); however, our experimental system is capable of generating DKQRs with $t \approx 5$ steps [23,36,37]. Figure 2 shows our numerical results of the MCD using Eq. (8) with 1000 noise trajectories, and topological diagrams using Eq. (9) with a time average over up to $t = 5$ applications of $\hat{\mathcal{U}}$. Similar to Ref. [11], our simulations keep the kick strength k_1 at $\pi/2$ while scanning k_2 within a range of $k_2 \in [0,\ 2.5\pi]$. Here, both kick strengths are expressed in dimensionless units. Scanning k_2 reveals topological phase transitions for each configuration of the kick strengths where the band gap in the Floquet spectrum closes [10]. A typical example is shown in Fig. 2, which indicates that the signature of the topological phase transitions decays continuously as ϕ increases but remains visible for $\phi \leqslant \pi/3$ [see the red curves in Fig. 2). Therefore the MW phase noise should be kept within $\phi < \pi/3$ in experiments.

B. Finite quasimomentum distributions

The periodicity of the kicking potential enables the use of Bloch's theorem with the momentum expressed as $p = n + \beta$. Here, n is an integer, and β is the dimensionless quasimomentum. Up to this point, we have exclusively discussed the case of $\mathcal{T} = \pi$ and $\beta = 0$; however, experiments with BECs usually start at a momentum close to $n = 0$ with a finite width Δ_β in the Brillouin zone. For example, Δ_β is found to be 0.025 in Refs. [23,36,37]. To model this finite quasimomentum distribution, a Gaussian distribution with zero mean value and full width at half maximum (FWHM) $\Delta_\beta = 0.025$ is used in our calculations. Figure 2 shows topological phase transitions as a function of the phase noise ϕ when different quasimomentum distributions are considered. Comparisons between Fig. 2(a) and Fig. 2(b) indicate that the quasimomenta present in experiments have little effect on the topological diagrams.

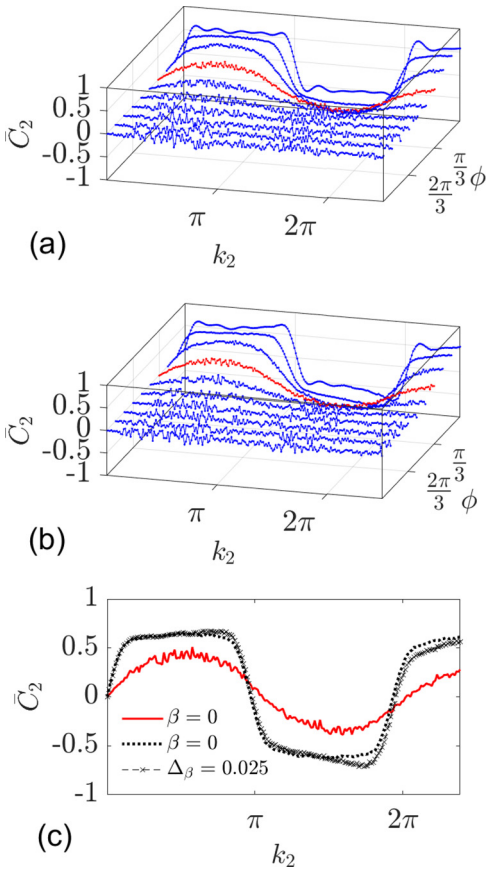

FIG. 2. (a) and (b) The predicted MCD and topological phase diagrams as a function of the noise strength ϕ when $\beta = 0$ (a) and $\Delta_\beta = 0.025$ (b) derived for our proposed sequence equation (12) at $\mathcal{T} = \pi$. The change in sign is compensated using Eq. (15), and the MCD is computed exploiting the symmetry of the initial state $|\psi_{\text{in}}\rangle = |n = 0\rangle \otimes |2\rangle$ as discussed in Sec. III B. The red curves correspond to $\phi = \pi/3$, the maximum phase noise acceptable for observing topological phase transitions. (c) The thick black dotted curve and thin black dashed curve with crosses represent cuts at $\phi = \pi/9$ from (a) and (b), respectively, and the red solid curve corresponds to a cut at $\phi = \pi/3$ from (a). While the steps are visible at small noise strength ϕ (see the black curves), they get washed out as ϕ becomes larger than $\pi/3$. For each k_2, the topological number is averaged over 1000 noise trajectories in all cases (see text).

C. Light-shift compensation

Our system has two internal hyperfine states; the kicking potential created by a virtual transition to a third state thus creates an additional energy gap between the two states. In our system, an atom-optics kicked rotor with two internal states, this light (or ac-Stark) shift effectively changes the kicking

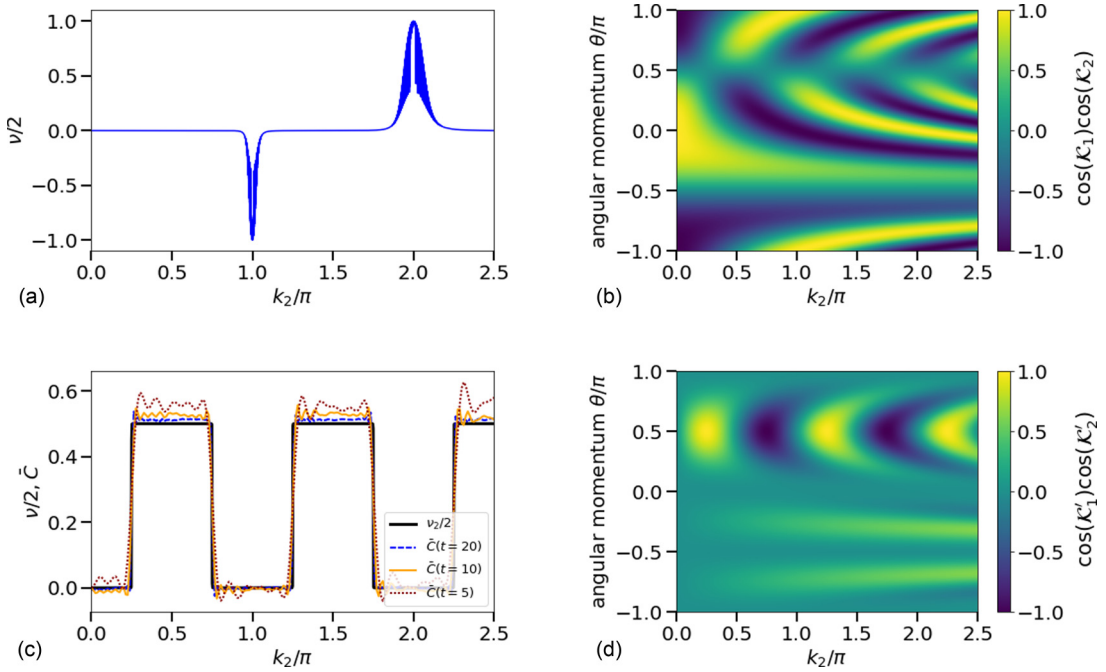

FIG. 3. (a) The winding number and (b) values of the function $\cos(\mathcal{K}_1)\cos(\mathcal{K}_2)$ derived from Eqs. (18) and (19), respectively, when light-shift effects are *not* compensated. (c) The winding number and (d) values of the function $\cos(\mathcal{K}_1)\cos(\mathcal{K}_2)$ derived from Eqs. (20) and (21), respectively, when light-shift effects are effectively compensated. In (c), the averaged MCD converges to the predicted phase transitions (black solid curve) as the evolution step t increases. If the $\cos(\mathcal{K}_1)\cos(\mathcal{K}_2)$ function changes sign, the topological phase changes thus implying instabilities. This is satisfied everywhere in (b) while only at specific points in (d); see the text.

potential to [40–42]

$$\hat{\mathcal{K}} \equiv 2k \cdot \cos^2\left(\frac{\hat{\theta}}{2}\right) = k(\cos(\hat{\theta}) + 1), \tag{17}$$

where the constant term independent of the angle θ represents the shift of the internal states. The total energy shift to be corrected for is thus $2k$ for a single kick of the kicking strength k in our atom-optics kicked rotor systems and the quantum walk experiments [23,36,37], because the second internal state effectively sees a kick with an opposite sign.

To observe topological phases, it is important to have a relative shift of $\Delta\theta = \pi/2$ in position space between the two kicks $\hat{K}_1$ and $\hat{K}_2$ [see Eqs. (3) and (4)]. The effective kick operators are then

$$\hat{K}_{1,\text{eff}} = e^{-ik_1\hat{\sigma}_z(\cos(\hat{\theta})+1)} \equiv e^{-i\hat{\sigma}_z\hat{\mathcal{K}}_1}, \tag{18}$$

$$\hat{K}_{2,\text{eff}} = e^{-ik_2\hat{\sigma}_z(\sin(\hat{\theta})+1)} \equiv e^{-i\hat{\sigma}_z\hat{\mathcal{K}}_2}. \tag{19}$$

The effective kick potentials are described by $\hat{\mathcal{K}}_1$ and $\hat{\mathcal{K}}_2$. No topological phase transitions are observed if these operators are implemented without compensating light shifts as shown in Fig. 3(a). This is because a topological winding number can only change if $\cos(\mathcal{K}_1)\cos(\mathcal{K}_2) = \pm 1$ corresponding to a closing band gap (see Ref. [10]). Figure 3(b) shows that this condition is always fulfilled within the simulated range of k_2; thus it becomes impossible to distinguish between topological phase transitions and possible instability, if light shifts are not compensated. This suggests that compensation of light shifts is necessary for observation of topological phase transitions in experiments.

In walk experiments as reported in Refs. [23,36,37], compensation of light shifts was done by adjusting the phase of MW pulses. Such a procedure is necessary for each kick in the DKQR system, where two kicks have different kicking strengths. Our simulations, however, indicate that compensating one of the two kicking pulses is sufficient. For example, a simpler method of compensation can be conducted by correcting the light shift originating from k_1; therefore the kicking operators are

$$\hat{K}_{1,\text{eff}} \to e^{-ik_1\hat{\sigma}_z\cos(\hat{\theta})} \equiv e^{-i\hat{\sigma}_z\hat{\mathcal{K}}'_1}, \tag{20}$$

$$\hat{K}_{2,\text{eff}} \to e^{-ik_2\hat{\sigma}_z\sin(\hat{\theta})}e^{-i(k_2-k_1)\hat{\sigma}_z} \equiv e^{-i\hat{\sigma}_z\hat{\mathcal{K}}'_2}, \tag{21}$$

where the effective kick dynamics described by $\hat{\mathcal{K}}'_1$ and $\hat{\mathcal{K}}'_2$ are partially compensated. This compensation may not remove light-shift effects completely; however, it is adequate for observing topological phase transitions as shown in Figs. 3(c) and 3(d). Our calculations show that the number of topological phase transitions doubles in the same range of k_2 when the light shift is compensated. This implies that it may be possible to observe topological phase transitions by scanning k_2 even in a smaller range after light shifts are effectively compensated.

V. CONCLUSION

We have investigated the feasibility of measuring topological phase transitions with the DKQR platform and demonstrated how impacts of decoherence and experimental durations can be minimized by setting the duration of each MW rotation at $\mathcal{T} = \pi$ corresponding to a quarter of the Talbot period. A proper choice of initial states possessing an

inversion symmetry is found to further simplify experimental realizations.

Our results have suggested that a successful protocol for observing topological phase transitions must minimize the phase noise to $\phi \leqslant \pi/3$ and at least partially compensate the light-shift effects. Compensating light-shift effects can also facilitate experiments as it doubles the number of expected topological steps within the same k_2 scanning range. Our findings have thus confirmed that the DKQR is a promising platform to realize and measure topological phases in a time-dependent Floquet setup.

ACKNOWLEDGMENT

J.H.C. and Y.L. thank the Noble Foundation for financial support.

APPENDIX A: SIMPLIFICATION OF ORIGINAL PROPOSED SEQUENCE

For the evolution operator $\hat{\mathcal{U}}$ the first and the last MW rotation are inverse to each other:

$$\hat{M}\left(\frac{\pi}{2},0\right)=\hat{M}\left(-\frac{\pi}{2},0\right)^{-1},\quad \hat{M}\left(-\frac{\pi}{2},\frac{\pi}{2}\right)=\hat{M}\left(\frac{\pi}{2},\frac{\pi}{2}\right)^{-1}. \tag{A1}$$

When $\hat{\mathcal{U}}$ is applied subsequently, this can be exploited to reduce the amount of necessary MWs and kicks in $\hat{\mathcal{U}}$. It is sufficient to study this effect for $\hat{\mathcal{U}}^2$.

$$\hat{\mathcal{U}}^2=\left(\hat{M}\left(-\frac{\pi}{2},\frac{\pi}{2}\right)\hat{K}_2^{\frac{1}{2}}\hat{M}\left(\frac{\pi}{2},\frac{\pi}{2}\right)\hat{M}\left(-\frac{\pi}{2},0\right)\hat{K}_1\hat{M}\left(\frac{\pi}{2},0\right)\hat{M}\left(-\frac{\pi}{2},\frac{\pi}{2}\right)\hat{K}_2^{\frac{1}{2}}\hat{M}\left(\frac{\pi}{2},\frac{\pi}{2}\right)\right)^2 \tag{A2}$$

$$=\hat{M}\left(-\frac{\pi}{2},\frac{\pi}{2}\right)\hat{K}_2^{\frac{1}{2}}\hat{M}\left(\frac{\pi}{2},\frac{\pi}{2}\right)\hat{M}\left(-\frac{\pi}{2},0\right)\hat{K}_1\hat{M}\left(\frac{\pi}{2},0\right)\hat{M}\left(-\frac{\pi}{2},\frac{\pi}{2}\right)K_2^{\frac{1}{2}} \tag{A3}$$

$$\cdot\hat{K}_2^{\frac{1}{2}}\hat{M}\left(\frac{\pi}{2},\frac{\pi}{2}\right)\hat{M}\left(-\frac{\pi}{2},0\right)\hat{K}_1\hat{M}\left(\frac{\pi}{2},0\right)\hat{M}\left(-\frac{\pi}{2},\frac{\pi}{2}\right)\hat{K}_2^{\frac{1}{2}}\hat{M}\left(\frac{\pi}{2},\frac{\pi}{2}\right) \tag{A4}$$

$$=\hat{M}\left(-\frac{\pi}{2},\frac{\pi}{2}\right)\hat{K}_2^{\frac{1}{2}}\hat{M}\left(\frac{\pi}{2},\frac{\pi}{2}\right)\hat{M}\left(-\frac{\pi}{2},0\right)\hat{K}_1\hat{M}\left(\frac{\pi}{2},0\right)\hat{M}\left(-\frac{\pi}{2},\frac{\pi}{2}\right)\hat{K}_2\hat{M}\left(\frac{\pi}{2},\frac{\pi}{2}\right) \tag{A5}$$

$$\cdot\hat{M}\left(-\frac{\pi}{2},0\right)\hat{K}_1\hat{M}\left(\frac{\pi}{2},0\right)\hat{M}\left(-\frac{\pi}{2},\frac{\pi}{2}\right)\hat{K}_2^{\frac{1}{2}}\hat{M}\left(\frac{\pi}{2},\frac{\pi}{2}\right). \tag{A6}$$

APPENDIX B: CONDITIONS NECESSARY FOR SEQUENCE RESONANCE CONSIDERATIONS

We consider the free-evolution operator $\hat{P}=e^{-i\frac{\hat{p}^2}{2}\mathcal{T}}$ for a quarter Talbot time $\mathcal{T}=\pi$. Using Bloch's theorem, we can decompose momentum $\hat{p}$ into an integer and a quasimomentum β: $\hat{p}=\hat{n}+\beta$, with $\beta\in[0,1)$. In the following we choose resonant values for β, for instance, $\beta=0$ [25], to simplify the discussion. We can identify similarly to Refs. [38,43] the free-evolution operator with the shift operator in momentum space:

$$\hat{P}_\pi^2=(e^{-i\frac{\hat{n}^2}{2}\pi})^2=e^{-i\hat{n}^2\pi}=\begin{cases}1 & n=2j\\ -1 & n=2j+1\end{cases}\equiv e^{-i\hat{n}\pi}\equiv\hat{T}(\pi). \tag{B1}$$

$\hat{T}(\pi)$ can thus denote the shift operator in angular momentum space for $\theta=\pi$. The free-evolution operator for the two-state system commutes with the microwave operators since the entries of the MW matrix are scalar values.

$$\hat{P}=e^{-i\frac{(\hat{n}+\beta)^2}{2}\tau\otimes\mathbf{1}}=e^{-i\frac{(\hat{n}+\beta)^2}{2}\tau}\cdot\mathbf{1} \tag{B2}$$

$$\Rightarrow\hat{P}\hat{M}(\alpha_1,\chi_1)\hat{P}\hat{M}(\alpha_2,\chi_2)=\hat{M}(\alpha_1,\chi_1)\hat{M}(\alpha_2,\chi_2)\hat{P}^2 \tag{B3}$$

$$=\hat{M}(\alpha_1,\chi_1)\hat{M}(\alpha_2,\chi_2)\hat{T}(\pi). \tag{B4}$$

The translation operator affects the kick operators $\hat{K}_1$ and $\hat{K}_2$ as follows:

$$\hat{T}(\pi)\hat{K}_{1,2}(k,\theta)=\hat{K}_{1,2}(k,\theta+\pi)=\hat{K}_{1,2}(-k,\theta)\equiv\hat{K}_{1,2}^{-1}, \tag{B5}$$

$$\hat{T}(2\pi)\hat{K}_{1,2}(k,\theta)=\hat{K}_{1,2}(k,\theta+2\pi)=\hat{K}_{1,2}(k,\theta). \tag{B6}$$

APPENDIX C: INTRODUCTION OF FREE EVOLUTION

The free-evolution operator $\hat{P}_\pi$ for $\mathcal{T}=\pi$ after neglecting quasimomentum is not unity. When each MW rotation is considered to have a finite duration, this affects the evolution of the system described by $\hat{U}^t$ in the following way:

$$\begin{aligned}\hat{\mathcal{U}}^t &= \hat{P}_\pi\hat{M}\Big(-\frac{\pi}{2},\frac{\pi}{2}\Big)\hat{K}_2^{\frac{1}{2}}\hat{P}_\pi\hat{M}\Big(\frac{\pi}{2},\frac{\pi}{2}\Big)\Big[\hat{P}_\pi\hat{M}\Big(-\frac{\pi}{2},0\Big)\hat{K}_1\hat{P}_\pi\hat{M}\Big(\frac{\pi}{2},0\Big)\hat{P}_\pi\hat{M}\Big(-\frac{\pi}{2},\frac{\pi}{2}\Big)\hat{K}_2\hat{P}_\pi\hat{M}\Big(\frac{\pi}{2},\frac{\pi}{2}\Big)\Big]^{t-1}\\ &\cdot\hat{P}_\pi\hat{M}\Big(-\frac{\pi}{2},0\Big)\hat{K}_1\hat{P}_\pi\hat{M}\Big(\frac{\pi}{2},0\Big)\hat{P}_\pi\hat{M}\Big(-\frac{\pi}{2},\frac{\pi}{2}\Big)\hat{K}_2^{\frac{1}{2}}\hat{P}_\pi\hat{M}\Big(\frac{\pi}{2},\frac{\pi}{2}\Big) \qquad \text{(C1)}\\ &= \hat{P}_\pi\hat{M}\Big(-\frac{\pi}{2},\frac{\pi}{2}\Big)\hat{K}_2^{\frac{1}{2}}\hat{M}\Big(\frac{\pi}{2},\frac{\pi}{2}\Big)\Big[\hat{M}\Big(-\frac{\pi}{2},0\Big)\hat{T}(\pi)\hat{K}_1\hat{M}\Big(\frac{\pi}{2},0\Big)\hat{M}\Big(-\frac{\pi}{2},\frac{\pi}{2}\Big)\hat{T}(\pi)\hat{K}_2\hat{M}\Big(\frac{\pi}{2},\frac{\pi}{2}\Big)\Big]^{t-1}\\ &\cdot\hat{M}\Big(-\frac{\pi}{2},0\Big)\hat{T}(\pi)\hat{K}_1\hat{M}\Big(\frac{\pi}{2},0\Big)\hat{M}\Big(-\frac{\pi}{2},\frac{\pi}{2}\Big)\hat{T}(\pi)\hat{K}_2^{\frac{1}{2}}\hat{P}_\pi\hat{M}\Big(\frac{\pi}{2},\frac{\pi}{2}\Big) \qquad \text{(C2)}\\ &= \hat{P}_\pi\hat{M}\Big(-\frac{\pi}{2},\frac{\pi}{2}\Big)\hat{K}_2^{\frac{1}{2}}\hat{M}\Big(\frac{\pi}{2},\frac{\pi}{2}\Big)\Big[\hat{M}\Big(-\frac{\pi}{2},0\Big)\hat{K}_1^{-1}\hat{M}\Big(\frac{\pi}{2},0\Big)\hat{M}\Big(-\frac{\pi}{2},\frac{\pi}{2}\Big)\hat{T}(2\pi)\hat{K}_2\hat{M}\Big(\frac{\pi}{2},\frac{\pi}{2}\Big)\Big]^{t-1}\\ &\cdot\hat{M}\Big(-\frac{\pi}{2},0\Big)\hat{K}_1^{-1}\hat{M}\Big(\frac{\pi}{2},0\Big)\hat{M}\Big(-\frac{\pi}{2},\frac{\pi}{2}\Big)\hat{T}(2\pi)\hat{K}_2^{\frac{1}{2}}\hat{P}_\pi\hat{M}\Big(\frac{\pi}{2},\frac{\pi}{2}\Big) \qquad \text{(C3)}\\ &= \hat{P}_\pi\hat{M}\Big(-\frac{\pi}{2},\frac{\pi}{2}\Big)\hat{K}_2^{\frac{1}{2}}\hat{M}\Big(\frac{\pi}{2},\frac{\pi}{2}\Big)\Big[\hat{M}\Big(-\frac{\pi}{2},0\Big)\hat{K}_1^{-1}\hat{M}\Big(\frac{\pi}{2},0\Big)\hat{M}\Big(-\frac{\pi}{2},\frac{\pi}{2}\Big)\hat{K}_2\hat{M}\Big(\frac{\pi}{2},\frac{\pi}{2}\Big)\Big]^{t-1}\\ &\cdot\hat{M}\Big(-\frac{\pi}{2},0\Big)\hat{K}_1^{-1}\hat{M}\Big(\frac{\pi}{2},0\Big)\hat{M}\Big(-\frac{\pi}{2},\frac{\pi}{2}\Big)\hat{K}_2^{\frac{1}{2}}\hat{P}_\pi\hat{M}\Big(\frac{\pi}{2},\frac{\pi}{2}\Big). \qquad \text{(C4)}\end{aligned}$$

Therefore every second kick operator (here, $\hat{K}_1$) effectively experiences an inversion.

[1] D. Y. H. Ho and J. Gong, Topological effects in chiral symmetric driven systems, Phys. Rev. B **90**, 195419 (2014).

[2] X.-L. Qi and S.-C. Zhang, Topological insulators and superconductors, Rev. Mod. Phys. **83**, 1057 (2011).

[3] M. Z. Hasan and C. L. Kane, Colloquium: topological insulators, Rev. Mod. Phys. **82**, 3045 (2010).

[4] J. M. Kosterlitz and D. J. Thouless, Ordering, metastability and phase transitions in two-dimensional systems, J. Phys. C: Solid State Phys. **6**, 1181 (1973).

[5] N. D. Mermin, The topological theory of defects in ordered media, Rev. Mod. Phys. **51**, 591 (1979).

[6] A. Kitaev and C. Laumann, Topological phases and quantum computation, arXiv:0904.2771.

[7] T. Kitagawa, Topological phenomena in quantum walks: elementary introduction to the physics of topological phases, Quantum Inf. Process. **11**, 1107 (2012).

[8] P. Leboeuf, J. Kurchan, M. Feingold, and D. P. Arovas, Phase-Space Localization: Topological Aspects of Quantum Chaos, Phys. Rev. Lett. **65**, 3076 (1990).

[9] A. Eckardt, Colloquium: Atomic quantum gases in periodically driven optical lattices, Rev. Mod. Phys. **89**, 011004 (2017).

[10] L. Zhou and J. Gong, Floquet topological phases in a spin-1/2 double kicked rotor, Phys. Rev. A **97**, 063603 (2018).

[11] C. Groiseau, A. Wagner, G. S. Summy, and S. Wimberger, Impact of lattice vibrations on the dynamics of a spinor atom-optics kicked rotor, Condens. Matter **4**, 10 (2019).

[12] J. Cayssol and J.-N. Fuchs, Topological and geometrical aspects of band theory, J. Phys. Mater. **4**, 034007 (2021).

[13] M. Aidelsburger, M. Lohse, C. Schweizer, M. Atala, J. T. Barreiro, S. Nascimbène, N. R. Cooper, I. Bloch, and N. Goldman, Measuring the Chern number of Hofstadter bands with ultracold bosonic atoms, Nat. Phys. **11**, 162 (2015).

[14] G. Jotzu, M. Messer, R. Desbuquois, M. Lebrat, T. Uehlinger, D. Greif, and T. Esslinger, Experimental realization of the topological Haldane model with ultracold fermions, Nature (London) **515**, 237 (2014).

[15] W. Hu, J. C. Pillay, K. Wu, M. Pasek, P. P. Shum, and Y. D. Chong, Measurement of a Topological Edge Invariant in a Microwave Network, Phys. Rev. X **5**, 011012 (2015).

[16] S. Mukherjee, A. Spracklen, M. Valiente, E. Andersson, P. Öhberg, N. Goldman, and R. R. Thomson, Experimental observation of anomalous topological edge modes in a slowly driven photonic lattice, Nat. Commun. **8**, 13918 (2017).

[17] T. Kitagawa, M. A. Broome, A. Fedrizzi, M. S. Rudner, E. Berg, I. Kassal, A. Aspuru-Guzik, E. Demler, and A. G. White, Observation of topologically protected bound states in photonic quantum walks, Nat. Commun. **3**, 882 (2012).

[18] R. Süsstrunk and S. D. Huber, Observation of phononic helical edge states in a mechanical topological insulator, Science **349**, 47 (2015).

[19] R. Fleury, A. B. Khanikaev, and A. Alù, Floquet topological insulators for sound, Nat. Commun. **7**, 11744 (2016).

[20] M. Xiao, G. Ma, Z. Yang, P. Sheng, Z. Q. Zhang, and C. T. Chan, Geometric phase and band inversion in periodic acoustic systems, Nat. Phys. **11**, 240 (2015).

[21] J. K. Asbóth and H. Obuse, Bulk-boundary correspondence for chiral symmetric quantum walks, Phys. Rev. B **88**, 121406(R) (2013).

[22] J. K. Asbóth, Symmetries, topological phases, and bound states in the one-dimensional quantum walk, Phys. Rev. B **86**, 195414 (2012).

[23] S. Dadras, A. Gresch, C. Groiseau, S. Wimberger, and G. S. Summy, Experimental realization of a momentum-space quantum walk, Phys. Rev. A **99**, 043617 (2019).

[24] M. G. Raizen, Quantum chaos with cold atoms, Adv. At. Mol. Opt. Phys. **41**, 199 (1999).
[25] M. Sadgrove and S. Wimberger, A pseudo-classical method for the atom-optics kicked rotor: From theory to experiment and back, Adv. At. Mol. Opt. Phys. **60**, 315 (2011).
[26] C. Ryu, M. F. Andersen, A. Vaziri, M. B. d'Arcy, J. M. Grossman, K. Helmerson, and W. D. Phillips, High-Order Quantum Resonances Observed in a Periodically Kicked Bose-Einstein Condensate, Phys. Rev. Lett. **96**, 160403 (2006).
[27] I. Talukdar, R. Shrestha, and G. S. Summy, Sub-Fourier Characteristics of a δ-Kicked-Rotor Resonance, Phys. Rev. Lett. **105**, 054103 (2010).
[28] F. L. Moore, J. C. Robinson, C. F. Bharucha, B. Sundaram, and M. G. Raizen, Atom Optics Realization of the Quantum δ-Kicked Rotor, Phys. Rev. Lett. **75**, 4598 (1995).
[29] J. F. Kanem, S. Maneshi, M. Partlow, M. Spanner, and A. M. Steinberg, Observation of High-Order Quantum Resonances in the Kicked Rotor, Phys. Rev. Lett. **98**, 083004 (2007).
[30] A. Ullah and M. D. Hoogerland, Experimental observation of Loschmidt time reversal of a quantum chaotic system, Phys. Rev. E **83**, 046218 (2011).
[31] I. Dana, V. Ramareddy, I. Talukdar, and G. S. Summy, Experimental Realization of Quantum-Resonance Ratchets at Arbitrary Quasimomenta, Phys. Rev. Lett. **100**, 024103 (2008).
[32] M. Sadgrove, M. Horikoshi, T. Sekimura, and K. Nakagawa, Rectified Momentum Transport for a Kicked Bose-Einstein Condensate, Phys. Rev. Lett. **99**, 043002 (2007).
[33] D. R. Hofstadter, Energy levels and wave functions of Bloch electrons in rational and irrational magnetic fields, Phys. Rev. B **14**, 2239 (1976).
[34] M. Aidelsburger, M. Atala, M. Lohse, J. T. Barreiro, B. Paredes, and I. Bloch, Realization of the Hofstadter Hamiltonian with Ultracold Atoms in Optical Lattices, Phys. Rev. Lett. **111**, 185301 (2013).
[35] H. Miyake, G. A. Siviloglou, C. J. Kennedy, W. C. Burton, and W. Ketterle, Realizing the Harper Hamiltonian with Laser-Assisted Tunneling in Optical Lattices, Phys. Rev. Lett. **111**, 185302 (2013).
[36] S. Dadras, A. Gresch, C. Groiseau, S. Wimberger, and G. S. Summy, Quantum Walk in Momentum Space with a Bose-Einstein Condensate, Phys. Rev. Lett. **121**, 070402 (2018).
[37] J. H. Clark, C. Groiseau, Z. N. Shaw, S. Dadras, C. Binegar, S. Wimberger, G. S. Summy, and Y. Liu, Quantum to classical walk transitions tuned by spontaneous emissions, Phys. Rev. Res. **3**, 043062 (2021).
[38] S. Wimberger, I. Guarneri, and S. Fishman, Quantum resonances and decoherence for delta-kicked atoms, Nonlinearity **16**, 1381 (2003).
[39] A. Alberti and S. Wimberger, Quantum walk of a Bose-Einstein condensate in the Brillouin zone, Phys. Rev. A **96**, 023620 (2017).
[40] C. Groiseau, Discrete-time quantum walks in momentum space, Master's thesis, Heidelberg University, 2017.
[41] C. Groiseau, A. Gresch, and S. Wimberger, Quantum walks of kicked Bose-Einstein condensates, J. Phys. A: Math. Theor. **51**, 275301 (2018).
[42] N. Bolik, C. Groiseau, J. H. Clark, A. Gresch, S. Dadras, G. S. Summy, Y. Liu, and S. Wimberger, Light-shift-induced behaviors observed in momentum-space quantum walks, Phys. Rev. A **106**, 033307 (2022).
[43] A. Wagner, Topology in 1D quantum walks, Bachelor's thesis, Heidelberg University, 2018.

VITA

Jerry Clark

Candidate for the Degree of

Doctor of Philosophy

Thesis: QUANTUM WALKS OF A RUBIDIUM BOSE-EINSTEIN CONDENSATE AND THEIR APPLICATIONS

Major Field: Physics

Biographical:

Education:

Completed the requirements for the Doctor of Philosophy in Physics at Oklahoma State University, Stillwater, Oklahoma in December, 2022.

Completed the requirements for the Bachelor of Science in Physics, Chemistry, and Mathematics at Arkansas State University, Jonesboro, Arkansas in December, 2012.

Professional Membership:

American Physical Society